Spring 5-15-2019

# First-principles Study of Structural and Optical Properties of Novel Materials

Wenshen Song
*Washington University in St. Louis*

WASHINGTON UNIVERSITY IN ST. LOUIS

Department of Physics

Dissertation Examination Committee:
Li Yang, Chair
Erik Henriksen
Rohan Mishra
Zohar Nussinov
Lan Yang

# First-principles Study of Structural and Optical Properties of Novel Materials

by

Wenshen Song

A dissertation presented to
The Graduate School
of Washington University in
partial fulfillment of the
requirements for the degree
of Doctor of Philosophy

May 2019
St. Louis, Missouri

# Table of Contents

# Acknowledgments

I would first like to acknowledge my advisor Dr. Li Yang, who was giving me tremendous encouragement and support in my journey through graduate school. I deeply appreciate for his creative ideas, expert guidance and generous contribution in my research field, as well as for the trust and freedom that he gave me to explore my own career.

I would like to acknowledge the members of my committee, Dr. Erik Henriksen and Dr. Zohar Nussinov from Department of Physics, Dr. Rohan Mishra from Department of Mechanical Engineering and Materials Science and Dr. Lan Yang from Department of Electrical and Systems Engineering, for their time and support. I would also like to acknowledge to my collaborators Dr. Jie Guan at Southeast University, Dr. David Tománek at Michigan State University, Dr. Su Huang and Dr. Lan Yang at Washington University in St. Louis, and Dr. Guang-Yu Guo at National Taiwan University, who provide indispensable help and instructions in my research.

I would like to acknowledge Dr. Ruixiang Fei, who is a helpful former group member, an impressive research partner and coauthor, and a genuine friend. The growth that I have experienced through our work and friendship has a major impact on my life.

Lastly, I would like to acknowledge my other group members of past and present, Dr. Ryan Soklaski, Dr. Vy Tran, Dr. Shiyuan Gao, Xiaobo Lu and Linghan Zhu. Thank you for your support and friendship.

Wenshen Song

*Washington University in St. Louis*

*May 2019*

Dedicated to my loving family.

ABSTRACT OF THE DISSERTATION

First-principles Study of Structural and Optical Properties of Novel Materials

by

Wenshen Song

Doctor of Philosophy in Physics

Washington University in St. Louis, 2019

Professor Li Yang, Chair

Novel materials, including two-dimensional (2D) materials, ferroelectric materials, as well as hybrid perovskites materials, have attracted tremendous attention in recent years because of their unique structural symmetries and electronic structures. Among them, 2D materials, such as graphene, black phosphorene, and transition metal dichalcogenides (TMDs), etc., have great potentials for nanoelectronics and optical applications. Particularly, these 2D materials can sustain much larger strain than their bulk counterparts, making strain a unique and efficient tool to tune a wide range of properties of 2D structures. In the first part of this thesis, we explore how strain tunes quasiparticle energy and excitonic effects of typical 2D materials, including black phosphorus and monolayer 2H-phase TMDs, i.e., $MoS_2$, $MoSe_2$, $WS_2$, and $WSe_2$. Beyond the widely studied uniaxial and biaxial strain, we expand the research to arbitrarily axial strains and find complicated variations of quasiparticle band gaps, band-edge energies, direct-indirect gap transitions, and exciton energies. These results provide a complete picture for straining engineering of electronic structures and optical spectra of 2D TMDs.

The second part of this thesis focuses on the electronic polarization of non-centrosymmetric layered van der Waals (vdW) metal chalcogen-diphosphates MCDs, especially on $CuInP_2Se_6$. We employ first-principles modern-polarization theory to study the electrical polarization

ordering and build an electrostatic-energy model to explore the effects of boundary conditions. We find the existence of intrinsic off-plane polarization of $CuInP_2Se_6$, with an antiferroelectric (AFE) ground state for monolayer and ferroelectric state (FE) ground state for bulk under the open-circuit boundary condition. However, for close-circuit boundary condition, we find that the ground state is always FE through bulk to monolayer. We also apply Monte Carlo simulations to obtain the FE Curie temperature and electric hysteresis. This study gives hope to overcoming the depolarization effect and realizing ultra-thin FE transistors and memories based on vdW materials.

In the last part, we focus on nonlinear optical properties of a novel family of materials, organic-inorganic hybrid perovskites materials. We have developed a high-efficient, large-scale parallel simulation tool (NLOPACK), making it possible to explore the nonlinear optical properties of a family of organic-inorganic hybrid halide perovskites, $CH_3NH_3MX_3$ (M= Ge, Sn, Pb; X=Cl, Br, I), which contains a large number of atoms and cannot be handled by traditional simulation packages. We employ this code and find significant second harmonic generation (SHG) and linear electro-optic (LEO) effect in the cubic phase of $CH_3NH_3SnI_3$, in which those effects are comparable with those widely used organic/inorganic nonlinear optical materials. The reason for these enhanced nonlinear optical properties in hybrid perovskites is explained as well. This work will motivate experimental efforts to fabricate hybrid perovskites for low-cost, nonlinear-optical device implementations.

# Chapter 1: Introduction

Nowadays, the exploration of novel materials have experienced explosive growth in numerous fields, such as physics, electronic engineering, chemistry, medicine, energy systems, etc. [1]–[5]. Among the novel materials, two-dimensional (2D) materials has become a rising star in the past tens of years. Starting with the discovery of single layer graphene by Novoselov and Geim in 2004 [6], followed by other materials like hexagonal boron nitride (h-BN), transition metal dichalcogenide (TMDCs) and black phosphorus (BP) [7]–[9], 2D materials are springing like mushrooms and exhibit fascinating and promising properties in applications including electronics, optoelectronics and photonics, etc. [10]–[15]. Particularly, the synthesis of monolayer $MoS_2$, one of the most representative TMDCs, in 2010 [16] becomes a milestone for nanoelectronics applications. With band gap around 1.7 eV, direct-band-gap 2D semiconductor monolayer $MoS_2$ exhibits strong photoluminescence spectroscopy [16], [17], which is quite distinct from its bulk counterpart which is indirect-band-gap. Therefore, monolayer $MoS_2$ has great potentials in visible-light optoelectronic applications. Moreover, monolayer $MoSe_2$, $WS_2$, $WSe_2$ from the same TMDCs family, have shown similar electronic and optical properties as monolayer $MoS_2$ [18], [19].

The aforementioned electronic and optical properties are largely determined by quasiparticles excitation of many-body electron systems. The most important quasiparticles is exciton [20], which is formed by the electron-hole pair interaction after the electron is excited by incident photons and attracted by the left-over hole under Coulomb interaction. This electron-hole pair is vital in determining the electronic and optical properties, especially when electrons are confined in low-dimensional materials which enhances the many-body effect to a large extent [21]. As a

result, excited properties, such as photoluminescence (PL) and band energies, are of great importance in 2D TMDCs, and have been studied widely in recent years [22]–[26].

It is a common practice to manipulate material structures for new properties and improving performance. Therefore, we have huge interest in tuning excited-state properties by external means. Among these means, strain is known for effectively impacting a wide range of properties and tailoring materials for various applications [27]–[36]. This is particularly intriguing for two-dimensional (2D) structures that can sustain much larger magnitude of strain than their bulk counterparts. Still, experimentally controllable strain engineering is still challenging since: 1. Stretching or bending 2D structures usually introduces spatially inhomogeneous strain; 2. Complicated strain distribution is widely expected in fabricated samples [28], [29], [37], [38]. As a result, simple cases such as uniaxial/biaxial strains along specific high-symmetry directions [39]–[41] are not enough to cover the experimentally trained conditions that the strain may be applied with differently amplitudes along different directions because of substrates or various boundary conditions. It is necessary to cover arbitrarily axial strain and essential to explore the 2D strain-mapping properties. Moreover, typical first-principles calculations are based on density-functional theory (DFT), but the excited-state properties require including many electron effects, *i.e.*, electronic self-energy and electron-hole (*e*-*h*) interactions, which are beyond DFT. Therefore, a first-principles calculation considering complicated strain conditions and including many-electron effects is essential for explaining a wide range of measurements and guiding future strain engineering of 2D materials.

Apart from excited-state properties of 2D materials, polarization ordering, such as ferroelectricity is another interesting and intriguing field which has attracted extensive attention in 2D materials. Polarization orderings, mainly including ferroelectrics (FE) and antiferroelectric

(AFE), arise from macroscopic polarization induced by spontaneous ordering of electric dipoles and switchable under external electric field. The ultrathin FE films are extremely useful structure for exploring new physics and realizing device applications, such as FE transistors and memories [42]. Ferroelectrics has been thoroughly studied in bulk materials like perovskites oxides [43]–[50]. However, surface dangling bonds and accumulated free electrons will appear at the intersections for these materials when exfoliating. Meanwhile, their ferroelectricity is extremely sensitive to vertical boundary conditions [51], [52]. As a result, drastic depolarization effects emerge in these three-dimensional structures when they are thinned down, resulting in a suppression of polarization and thus a critical thickness for sustaining the FE state [53], [54]. Thus, realizing ultrathin ferroelectricity is hard to achieve.

Layered van der Waals (vdW) materials may give hope to overcoming this challenge, since there are no chemical bonds between layers. 2D in-plane ferroelectricity has been predicted and observed in monolayer group IV monochalcogenides [55]–[58]. For the most useful off-plane (vertical) ferroelectricity, it is still challenging. Recently, experiments reported that metal chalcogen-diphosphates (MCDs) can be a promising family of ultrathin FE materials [59]. However, other measurements claim that ferroelectricity can only exist in samples with much larger thickness of MCDs [60], [61]. Furthermore, the electric boundary conditions between top and bottom surfaces of slab structure of MCDs are crucial in determining polarization orders, as mentioned before. Thus, it is worthwhile to explore the polarization order through first-principles calculations, under different boundary conditions and layer thickness.

Another novel material that have attracted considerable interest in recent years is nonlinear optical (NLO) materials, which play an important role in modern electronics and photonics. In NLO materials, a variety of nonlinear processes can be realized, such as electro-optic (EO) effect

and second/third harmonic generation (SHG/THG) [62]. Traditional NLO materials such as ternary inorganic oxides have achieved widespread success and play key roles in related industries due to their reliable performance, low optical loss, and good stability. However, the synthesis of these insoluble oxides requires high temperature treatment, which hinders their application for most flexible substrates and their integration into chip-scale nanophotonic devices. On the other hand, although conventional organic NLO materials based on chromophores have been considered a promising alternative due to their solution processability, faster response and stronger NLO activities, their low intrinsic stability and high optical loss severely hindered their applications where high light intensity and elevated temperature are expected [63].

Nowadays, organic-inorganic hybrid halide perovskites (OHPs), such as $CH_3NH_3MX_3$ (M=Ge, Sn, Pb; X= I, Br, Cl), becomes increasingly important and prestigious in the fast-growing photovoltaic technologies [64]–[67]. Due to the asymmetry of $CH_3NH_3$ units, ferroelectricity could be realized in this family of materials naturally or by artificially tuning [68]–[70]. This broken inversion symmetry also ensures even order nonlinear optical properties [71], especially second harmonic generation (SHG) and linear electro-optic (LEO) effects are also expected in such materials [72]–[74]. Moreover, given the fact that such compounds can be easily fabricated from liquid phase [13], [14] and nearly unlimited choices of compositions [15], [16], OHPs may exhibit unique advantages in fabricating cost and optimizations of NLO properties, compared to traditional NLO materials. Moreover, given the fact that such compounds can be easily fabricated from liquid phase [64], [65] and nearly unlimited choices of compositions [66], [67], OHPs may exhibit unique advantages in fabricating cost and optimizations of NLO properties, compared to traditional NLO materials.

Although calculations of second-order nonlinear optical properties have been conducted to a large number of systems without inversion symmetry from 1D to 3D [75]–[80]. Calculating and predicting NLO properties of OHPs are challenging for the available simulation tools, since it involves higher-order transitions, which are intrinsically much more expensive in simulation cost compared to those of linear optical responses. As a result, it requires fairly dense k-point sampling and a large number of empty bands to get convergence, especially for large and complex systems with low symmetry, just like OHPs. Such requirements make the calculation for nonlinear optical properties extremely hard and time-consuming. To achieve computational proficiency for studying NLO properties of OHPs, fundamental coding development is needed to for better parallelization performance and simulation efficiency.

This thesis is organized as follows. In Chapter 2, we go through the theoretical background and discuss the computational methods. We first start with density-functional theory (DFT), many-body perturbation theory, followed by modern theory of polarization and second-order nonlinear optics. Chapter 3 mainly focuses on quasiparticle energies and bright excitons of strained materials [81], [82], especially on four strained typical TMDC monolayers, *i.e.*, $MoS_2$, $MoSe_2$, $WS_2$, and $WSe_2$, using first-principles DFT and many body perturbation theory. By mapping their band gaps, absolute band-edge energies, and exciton frequencies into 2D contours of in-plane strain distributions, we are able to provide a complete picture of arbitrary strain effects on these important quantities.

In chapter 4, we take a typical member of layered vdW MCDs, $CuInP_2Se_6$, as an example and show that monolayer MCD may sustain a polarization ordering even down to the monolayer [83]. We reveal that the vertical boundary conditions are crucial for determining the polarization orders of ultrathin structures. Given the substantial transition energy barrier between AFE and

FE states, the FE state can be held as a robustly metastable state of the free-standing monolayer, giving rise to 2D vertical ferroelectricity. Finally, the FE phase transition temperature and electric hysteresis curves of the free-standing monolayer $CuInP_2Se_6$ are obtained by Monte Carlo (MC) simulations.

In chapter 5, we apply first-principles calculations to systematically investigate the family organic-inorganic hybrid halide perovskites $CH_3NH_3MX_3$ (M=Ge, Sn, Pb; X= I, Br, Cl) on structural and electronic properties. Based on that, second-order nonlinear optical properties, including SHG and LEO effects, are explored by our self-developed NLOPACK package, which is written in Fortran with Message Passing Interface (MPI) and performs parallel computation on k-points. It has good scalability for calculating large and complex system with dense k-point sampling and low symmetry, and the excellent parallelization performance can be hold for up to a few thousand processors. We explore linear and second-order nonlinear optical properties of cubic phase hybrid halide perovskites. Within this family of materials, we find relatively large SHG susceptibilities within the infrared frequency range as well significant LEO coefficients for $CH_3NH_3SnI_3$. Furthermore, we work into details to reveal the mechanism behind the formation of such large electro-optic coefficients.

# Chapter 2: Computational Methods

In an interacting many-electron system, the Hamiltonian can be expressed as [84], [85]:

$$\widehat{H}_{el} = -\frac{\hbar}{2m_e}\sum_i \nabla_i^2 + \sum_i V_{ext}(\boldsymbol{r}_i) + \frac{1}{2}\sum_i \frac{e^2}{|\boldsymbol{r}_i - \boldsymbol{r}_j|} \tag{2.1}$$

where $i$ is summed over all the electrons in the system. The first term is kinetic energy, and the second term is external potential of independent electrons, and the third term is the Coulomb interaction between all pairs of electrons. It is impossible to solve the formula straightforwardly since the number of electrons is extremely large in a real solid system. For approximate solutions [86], density functional theory (DFT) [87], [88] and the many-body Green's function method [89] are introduced and proved to be very effective in the study of the ground and excited state properties.

## 2.1 Density Functional Theory (DFT)

### 2.1.1 Hohenberg-Kohn Theorems and Kohn-Sham Equation

The foundation of DFT originates from two Hohenberg-Kohn Theorems published in 1964 [87]. The first Hohenberg-Kohn theorem states that, in a many-electron system, the ground-sate electron density $n(\boldsymbol{r})$ uniquely determines the external potential $v_{ext}(\boldsymbol{r})$ as well as the Hamiltonian of the system. As a consequence, all ground-state properties can be written as functional of the ground-state electron density $n(\boldsymbol{r})$ instead of the many-body wavefunction. The energy functional can be written as follows [87]:

$$E[n] = \int v_{ext}(\boldsymbol{r})n(\boldsymbol{r})d\boldsymbol{r} + F[n] \tag{2.2}$$

, where is $F[n]$ is the kinetic and interaction energy functional. The second Hohenberg-Kohn theorem states that for a given potential $v_{ext}(\boldsymbol{r})$ and total electron number $N$, the actual ground-state density will minimize the functional $E[n]$.

The most well-known approximation of the function $F[n]$ is Kohn-Sham formalism originally published in 1965 [88]. It separates the electronic kinetic energy and Hartree potential energy from Eq. (2.2):

$$E[n] = \int v_{ext}(\boldsymbol{r})n(\boldsymbol{r})d\boldsymbol{r} + T[n] + \frac{1}{2}\int \frac{n(\boldsymbol{r})n(\boldsymbol{r}')}{|\boldsymbol{r}-\boldsymbol{r}'|}d\boldsymbol{r}d\boldsymbol{r}' + E_{xc}[n] \tag{2.3}$$

, where $T[n]$ is the kinetic energy of non-interacting electrons and $E_{xc}[n]$is the exchange-correlation energy. Under the constraints of $\int \delta n(\boldsymbol{r})\, d\boldsymbol{r} = 0$, the variational stationary point can be expressed as:

$$v_{ext}(\boldsymbol{r}) + \frac{\delta T[n]}{\delta n(\boldsymbol{r})} + \int \frac{n(\boldsymbol{r}')}{|\boldsymbol{r}-\boldsymbol{r}'|}d\boldsymbol{r}' + \frac{\delta E_{xc}[n]}{\delta n(\boldsymbol{r})} = 0 \tag{2.4}$$

, which is equivalent to solving the single particle Schrodinger equation:

$$\left[-\frac{\hbar^2\nabla^2}{2m_e} + v_{ext}(\boldsymbol{r}) + \int \frac{n(\boldsymbol{r}')}{|\boldsymbol{r}-\boldsymbol{r}'|}d\boldsymbol{r}' + v_{xc}(\boldsymbol{r})\right]\psi_i(\boldsymbol{r}) = \varepsilon_i\psi_i(\boldsymbol{r}) \tag{2.5}$$

, where $n(\boldsymbol{r}) = \sum_i|\psi_i(\boldsymbol{r})|^2$ is charge density and $v_{xc}(\boldsymbol{r}) = \frac{\delta E_{xc}[n]}{\delta n(\boldsymbol{r})}$. Eq. (2.5) reduces N-electron problem to a single electron moving in effective potential induced by the other electrons and can be solved by self-consistent method. It simplifies the many-body problem to a large extent, thus become the foundation of most of the modern DFT calculations [84].

Since Hohenberg-Kohn theorems don't provide details of how to get the exchange-correlation potential $v_{xc}(\boldsymbol{r})$, different approximations have been developed for practical calculations. A simple approximation, local density approximation (LDA) [90], replaces $E_{xc}$ with exchange-correlation potential of homogeneous electron liquid. Another widely used approximation is the generalized gradient approximation (GGA) [91], proposes a more accurate way to include the first-order gradient expansion around the homogeneous density. LDA and GGA are widely used in the calculation of DFT, as they are able to give accurate description of the ground state as well as of good simplicity for efficient calculation. There are still plenty of other functionals which can achieve better accuracy by including more terms, at the expense of more computational cost, such as Perdew, Burke and Enzerhof (PBE) [92], Perdew and Wang (PW91) [93], etc.

### 2.1.2 Plane-Wave Pseudopotential Method

Good choice of basis function set is crucial for solving Kohn-Sham equations. In the early stage, the most natural and common choice is orthogonal plane wave method. However, core electrons are often localized by atomic nucleus, leading to drastic oscillation in near-core wavefunctions which requires too large a number of plane waves for efficient calculation. Considering that valence electrons make the dominated contributions in chemical bonding between solids rather than core electrons, it is a good idea to use pseudopotentials to only keep the characteristics of valence electrons and simplify core electrons. This plane wave pseudopotential method is very popular in first-principles calculation, and in this thesis, we will use it as our primary DFT methods.

## 2.2 Many-Body Perturbation Theory

Although DFT is widely accepted and applied in first-principles calculations, it still has non-neglectable limitation, that DFT is only exact for ground state but not for excited state. For

example, DFT always underestimate the quasiparticle band gap of materials [94]. Beyond DFT, the many-body perturbation theory provides a more accurate way to study the excited state properties.

### 2.2.1 Quasiparticle and GW Approximation

The electron-hole (*e*-*h*) quasiparticles are excitations behaving like free electron-hole bounded by screened Coulomb interaction, which is described by the electron's self-energy Σ. The energy of quasiparticle is solved by Dyson Equation [85], [89], [95],

$$\left[-\frac{1}{2}\nabla^2 + V(\boldsymbol{r})\right]\Phi_{n\boldsymbol{k}}(\boldsymbol{r}) + \int d\boldsymbol{r}'\Sigma(\boldsymbol{r},\boldsymbol{r}';E_{n\boldsymbol{k}})\Phi_{n\boldsymbol{k}}(\boldsymbol{r}') = E_{n\boldsymbol{k}}\Phi_{n\boldsymbol{k}}(\boldsymbol{r}) \tag{2.6}$$

In 1965, Hedin expands the self-energy and Green's function $G$ in terms of the screened Coulomb interaction $W$ [96]. Taking the first order, it can be expressed as:

$$\Sigma = iGW \tag{2.7}$$

, which is the origin of the name "GW approximation". For each k-point $\boldsymbol{k}$ and band $n$. The Dyson equation is solved in the first-order approximation [89]:

$$E_{n\boldsymbol{k}} = \varepsilon_{n\boldsymbol{k}}^{DFT} + \langle\psi_{n\boldsymbol{k}}^{DFT}|\Sigma_{n\boldsymbol{k}}(E_{n\boldsymbol{k}}) - v_{xc}|\psi_{n\boldsymbol{k}}^{DFT}\rangle \tag{2.8}$$

, where the $v_{xc}$ is the exchange-correlation contribution from DFT. The quasiparticle energy $E_{n\boldsymbol{k}}$ is determined based on the single-particle energy $E_{n\boldsymbol{k}}^{DFT}$ from DFT, and the DFT-level exchange-correlation energy is replaced by the many-body self-energy. The GW approximation is much more accurate in estimating the true band gap compared to DFT.

### 2.2.2 Exciton and Bethe-Salpeter Equation (BSE)

When an electron is excited into conduction bands, a positive empty hole is left over, and the electron and hole are bounded together with Coulomb interaction, forming a charge-neutral exciton. Excitons can be created by optical excitations, or annihilate under the recombination of electrons and holes, emitting a photon for each pair, as shown in Figure 2.1. Therefore, exciton is crucial in understanding the optical properties of a solid.

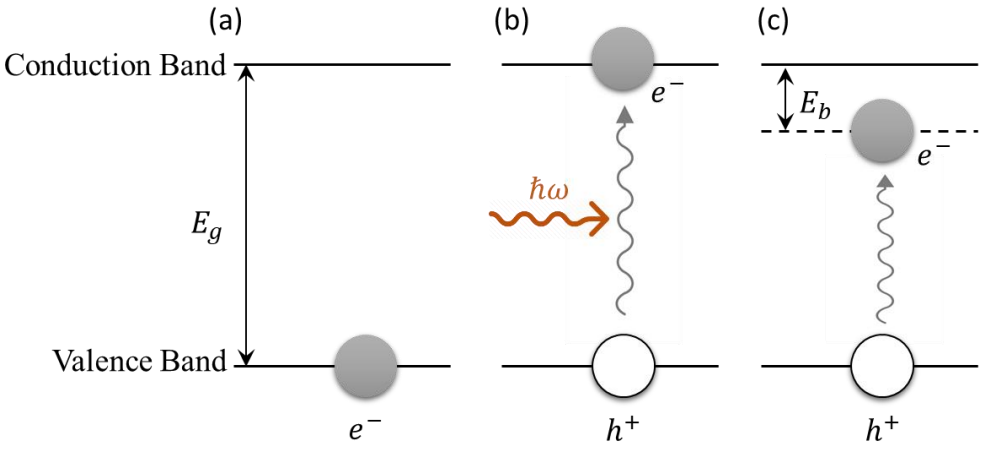


Figure 2.1 (a) The ground state of electrons in semiconductors with quasiparticle band gap $E_g$, (b) one electron excited by the incident photon, left over an empty hole (c) a bound state of the *e-h* pair by the attractive coulomb interaction, $E_b$ is the binding energy of the exciton state.

In many-body perturbation theory, Bethe-Salpeter Equation (BSE) [97], [98] is very powerful to study excitons. After Tamm-Dancoff approximation [97], it can be expressed as:

$$(E_{c\boldsymbol{k}} - E_{v\boldsymbol{k}})A^S_{vc\boldsymbol{k}} + \Sigma_{v'c'\boldsymbol{k}'}K_{vc\boldsymbol{k},v'c'\boldsymbol{k}'}(\Omega^S)A^S_{v'c'\boldsymbol{k}'} = \Omega^S A^S_{vc\boldsymbol{k}} \tag{2.9}$$

, in which $E_{c\boldsymbol{k}}$ is the quasi-electron energy, and $E_{v\boldsymbol{k}}$ is the quasi-hole energy, and $K_{vc\boldsymbol{k},v'c'\boldsymbol{k}'}$is the *e-h* kernel. $\Omega^S$ and $A^S_{vc\boldsymbol{k}}$ are the exciton energy and amplitude of a state S. The state S can be expressed as linear superposition of *e-h* pair states

$$|S\rangle = \sum_{v}^{occ} \sum_{c}^{empty} \sum_{\boldsymbol{k}} A_{vc\boldsymbol{k}}^{S} |vc\boldsymbol{k}\rangle \tag{2.10}$$

Since $E_{c\boldsymbol{k}}, E_{v\boldsymbol{k}}$ are band energies calculated by GW, BSE calculations are often performed after GW calculations. In general, exciton wavefunction in BSE needs finer k-points grid, on which the kernel is interpolated from original coarse grid [99]. The absorption spectrum can be obtained from BSE eigenstates.

Furthermore, if we want to calculate the optical absorption of a solid, which is the imaginary part of dielectric function, $\varepsilon_2(\omega)$. From Fermi's golden rule [100], we can get:

$$\varepsilon_2(\omega) = \frac{16\pi^2 e^2}{\omega^2} \sum_{vc\boldsymbol{k}} |\hat{e} \cdot \langle v\boldsymbol{k}|v|c\boldsymbol{k}\rangle|^2 \delta(\omega - E_{c\boldsymbol{k}} - E_{v\boldsymbol{k}}) \qquad \text{(without } e\text{-}h\text{)} \tag{2.11}$$

$$\varepsilon_2(\omega) = \frac{16\pi^2 e^2}{\omega^2} \sum_{S} |\hat{e} \cdot \langle 0|v|S\rangle|^2 \delta(\omega - \Omega^S) \qquad \text{(with } e\text{-}h\text{)} \tag{2.12}$$

, where $\hat{e} \cdot \langle v\boldsymbol{k}|v|c\boldsymbol{k}\rangle$ is velocity matrix along polarization light direction $\hat{e}$. Particularly in 2D materials, we can convert dielectric function into optical absorbance by:

$$A(\omega) = \omega \varepsilon_2(\omega) d/c \tag{2.13}$$

, where $d$ is the periodicity along off-plane direction and $c$ is the light speed. Optical absorbance $A(\omega)$ reflects the proportion of incident photons absorbed by a single layer of material.

## 2.3 Modern Theory of Polarization

For a periodic solid, the polarization cannot be well defined by traditional form. The so-called Modern theory of polarization [101] provides a route for such calculation in electronic structure codes through the Berry phase [102]. In the following, we will introduce modern theory of polarization following a simple qualitative discussion according to [103].

### 2.3.1 Periodicity and Polarization Quantum

The traditional way to describe polarization in finite systems is calculating the electric dipole moment, which can be defined as:

$$\boldsymbol{d} = \sum_i q_i \boldsymbol{r}_i \qquad \text{(point charges)} \tag{2.14}$$

$$\boldsymbol{d} = \int e\, n(\boldsymbol{r})\, \boldsymbol{r} d\boldsymbol{r} \qquad \text{(continuous charges)} \tag{2.15}$$

In one-dimensional chain system, as shown in Figure 2.2, the alternating anions and cations by the same interval in the upper chain should be non-polar due to inversion symmetry.

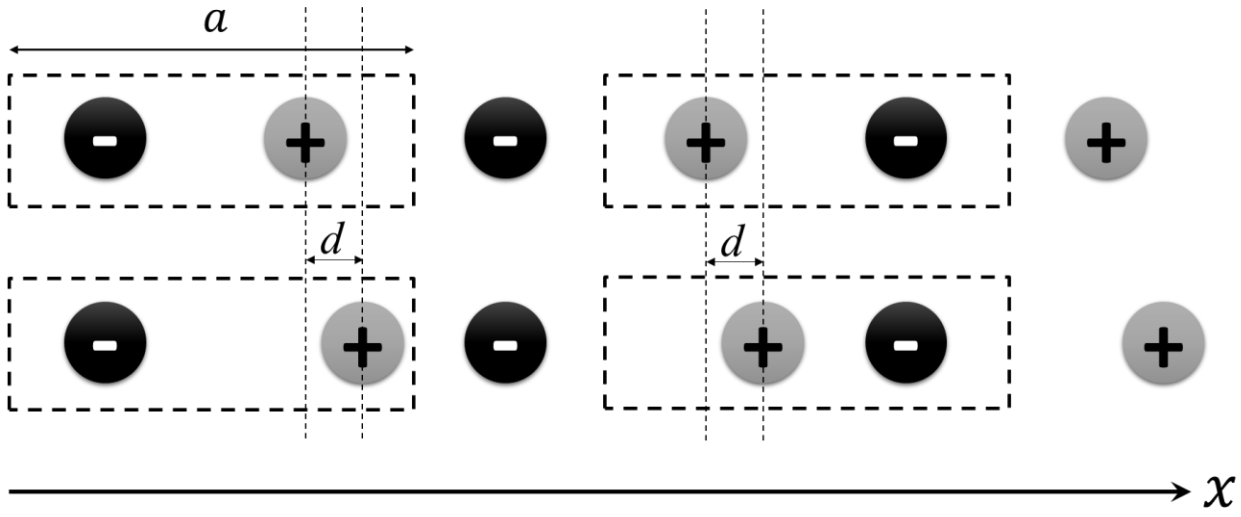


Figure 2.2 One-dimensional chain of alternating anions and cations with unit charge. In the lower chain, the cations are moved to x direction by a displacement of d compared to the upper chain

However, if we choose the unit cell, as the dash rectangle indicates, in the upper chain, the dipole moment per unit length is calculated to be:

$$p = \frac{1}{a}\sum_i q_i x_i = \frac{1}{a}\left(-1 \times \frac{a}{4} + 1 \times \frac{3a}{4}\right) = \frac{1}{2} \qquad \text{(left case)} \tag{2.16}$$

$$p = \frac{1}{a}\sum_i q_i x_i = \frac{1}{a}\left(1 \times \frac{a}{4} - 1 \times \frac{3a}{4}\right) = -\frac{1}{2} \qquad \text{(right case)} \tag{2.17}$$

It is very straightforward to find that, even for the same system, different choice of unit cell will lead to different values of dipole moments. For the upper chain in Figure 2.2, we can get a collection of $\ldots, -\frac{5}{2}, -\frac{3}{2}, -\frac{1}{2}, \frac{1}{2}, \frac{3}{2}, \frac{5}{2}, \ldots$, which are called polarization lattice, and the quantized value between adjacent values is called polarization quantum, $P_q$ [103]. For all one-dimensional non-polar systems, the polarization lattices are either $0 \pm nP_q$ (one ion at center and 2 opposite half-ion at unit cell boundaries, and zero point on one ion) or $\frac{P_q}{2} \pm nP_q$ (zero point not on any ions) [103], [104].

In experiments, spontaneous polarization is defined and measured by the change of polarization. In the lower chain in Figure 2.2, the dipole moment per unit length is

$$p = \frac{1}{a}\sum_i q_i x_i = \frac{1}{a}\left(-1 \times \frac{a}{4} + 1 \times (\frac{3a}{4} + d)\right) = \frac{1}{2} + \frac{d}{a} \qquad \text{(left case)} \qquad (2.18)$$

$$p = \frac{1}{a}\sum_i q_i x_i = \frac{1}{a}\left(1 \times \frac{a}{4} - 1 \times (\frac{3a}{4} + d)\right) = -\frac{1}{2} + \frac{d}{a} \qquad \text{(right case)} \qquad (2.19)$$

Again, we get different values differing by one polarization quantum, as Eq. (2.16), (2.17). Nevertheless, compared the polarization change $\delta p$ between upper chain and lower chain, the change is $\frac{d}{a}$ which are the same for left and right cases. Considering the upper chain is non-polar and the actual polarization value should be 0, we can use this well-defined single value of polarization change to serve as the spontaneous polarization as long as unit cell and basis are fixed.

Such a definition can be extended to three dimensions, in which the values of polarization lattice are spaced by $\frac{1}{\Omega} e\boldsymbol{R}$ [101], [104], where $e$ is the electronic charge, $\Omega$ is the unit cell volume and

$\boldsymbol{R} = \sum_i n_i R_i$ is any lattice vector, and $i$ donates the $x, y, z$ principle Cartesian directions. As a result, there are 3 polarization quanta for each direction of the basis vectors:

$$P_{q,i} = \frac{1}{\Omega} e R_i \tag{2.20}$$

### 2.3.2 Wannier Functions and Berry Phase

Up to now, we only discuss the polarization for point charge systems. However, in a real solid, electrons are dispersed in real space in the form of charge density, as shown in Figure 2.3. To extend our previous discussion effectively to the real case, we move on to Wannier functions [105], [106] and Berry phase method [102].

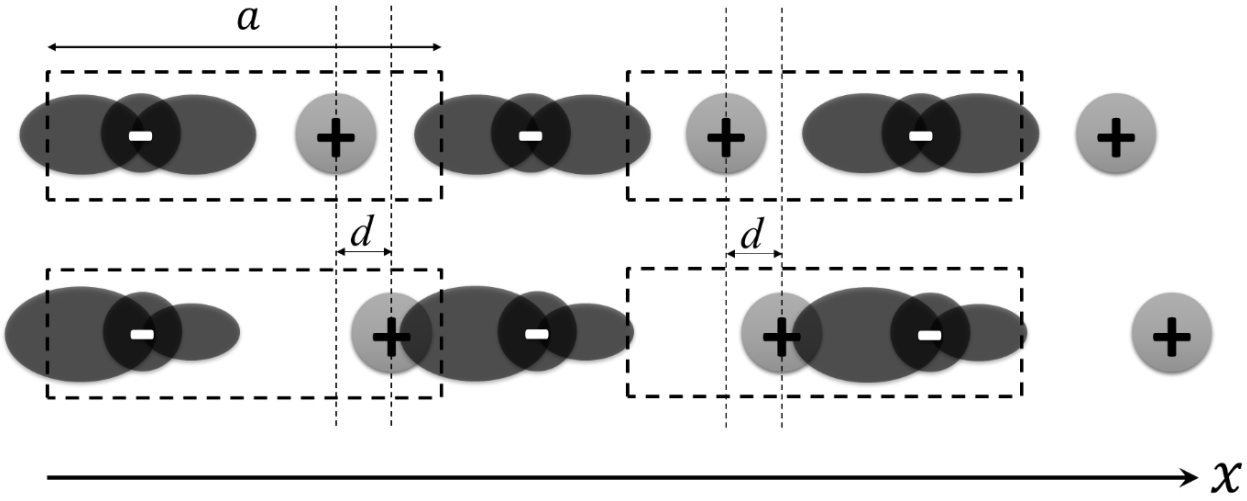


Figure 2.3 One-dimensional chain of alternating electron clouds and cations with unit charge. In the lower chain, the cations are moved to x direction by a displacement of d compared to the upper chain.

In unit cell $\boldsymbol{R}$, the Wannier function $w_n(\boldsymbol{r})$ with band $n$ is defined as [103]:

$$w_n(\boldsymbol{r} - \boldsymbol{R}) = \frac{\Omega}{(2\pi)^3} \int_{BZ} d^3\boldsymbol{k} e^{-i\boldsymbol{k}\boldsymbol{R}} \psi_{n\boldsymbol{k}}(\boldsymbol{r}) = \frac{\Omega}{(2\pi)^3} \int_{BZ} d^3\boldsymbol{k} e^{-i\boldsymbol{k}(\boldsymbol{r}-\boldsymbol{R})} u_{n\boldsymbol{k}}(\boldsymbol{r}) \tag{2.21}$$

, where $\psi_{n\boldsymbol{k}}(\boldsymbol{r}) = e^{i\boldsymbol{k}\boldsymbol{r}}u_{n\boldsymbol{k}}(\boldsymbol{r})$ are the Bloch functions. Wannier functions are localized in real space and often used to describe the chemical bonds in solid system. To calculate dipole moments, we can still treat ions as point charges. Meanwhile, we need to find the averaged position of the dispersed electrons and treat them as point charge in calculating dipole moment. This average position, as known as Wannier center, can be expressed as [105]:

$$\bar{\boldsymbol{r}}_n = \int w_n^*(\boldsymbol{r})\boldsymbol{r}w_n(\boldsymbol{r})d^3\boldsymbol{r} \tag{2.22}$$

In periodic cell, the position operator can be expressed in momentum representation $\boldsymbol{r} = -i(\frac{\partial u_{n\boldsymbol{k}}}{\partial \boldsymbol{k}})$, then we can rewrite Eq. (2.23) as:

$$\bar{\boldsymbol{r}}_n = -i\frac{\Omega}{(2\pi)^3}\int_{BZ} d^3\boldsymbol{k}e^{-i\boldsymbol{k}\boldsymbol{R}}\langle u_{n\boldsymbol{k}}|\frac{\partial u_{n\boldsymbol{k}}}{\partial \boldsymbol{k}}\rangle \tag{2.23}$$

Then the polarization can be expressed in a simple formula with the help of Wannier center with the summation through all the occupied Wannier functions [103]:

$$p = \frac{1}{a}(\sum_i (q_i x_i)^{ions} + \sum_n^{occ}(q_n\bar{\boldsymbol{r}}_n)^{Wannier\ functions}) \tag{2.24}$$

As mentioned previously, the spontaneous polarization between the polar final state and nonpolar initial state can be expressed as [103]:

$$\begin{aligned}\delta p = p^f - p^0 = &\frac{1}{\Omega}\sum_i \left[q_i^f \boldsymbol{r}_i^f - q_i^0\boldsymbol{r}_i^0\right] \\ &-\frac{2ie}{(2\pi)^3}\sum_n^{occ}[\int_{BZ} d^3\boldsymbol{k}e^{-i\boldsymbol{k}\boldsymbol{R}}(\langle u_{n\boldsymbol{k}}^f|\frac{\partial u_{n\boldsymbol{k}}^f}{\partial \boldsymbol{k}}\rangle - \langle u_{n\boldsymbol{k}}^0|\frac{\partial u_{n\boldsymbol{k}}^0}{\partial \boldsymbol{k}}\rangle)]\end{aligned} \tag{2.25}$$

In Eq. (2.25), the integrals are actually Berry phase developed by the wavefunction $u_{nk}$, that is [102]:

$$\sum_{n}^{occ} \int_{BZ} d^3\boldsymbol{k} e^{-i\boldsymbol{kR}} \langle u_{n\boldsymbol{k}} | \frac{\partial u_{n\boldsymbol{k}}}{\partial \boldsymbol{k}} \rangle \tag{2.26}$$

In this way, we start from Wannier functions to find the Wannier center as the center of electronic charge dispersed in space, and end with a Berry phase expression for spontaneous polarization.

## 2.4 Second-Order Nonlinear Optics Properties

Nonlinear optics is the study of phenomena that occur as a consequence of the modification of the optical properties of a material system by the presence of light [62], and they are called "nonlinear" because induced polarization responses nonlinearly to an applied optical field. The discovery of second-harmonic generation by Franken *et al.* (1961) [71] is often taken as the beginning of field of nonlinear optics. We will give basic introduction of nonlinear optics according to [62].

Conventionally, the induced polarization depends linearly on the electric field in a material:

$$\tilde{P}(t) = \epsilon_0 \chi^{(1)} \tilde{E}(t) \tag{2.27}$$

, where $\tilde{P}(t)$ is the polarization, $\tilde{E}(t)$ is the applied field, and $\chi^{(1)}$ is linear susceptibility and $\epsilon_0$ is the dielectric constant. In nonlinear optics, Eq. (2.27) is generalized into high-order expansion:

$$\tilde{P}(t) = \epsilon_0 \left[ \chi^{(1)} \tilde{E}(t) + \chi^{(2)} \tilde{E}^2(t) + \chi^{(3)} \tilde{E}^3(t) + \cdots \right] \tag{2.28}$$

$\chi^{(2)}$ is known as the second-order nonlinear optical susceptibilities and $\chi^{(3)}$ is the third-order nonlinear optical susceptibilities. It is easy to find that, the even order nonlinear optical

susceptibilities will vanish when there exists inversion symmetry, for the simple reason that if we reverse the applied field $\tilde{E}(t)$, the polarization $\tilde{P}(t)$ will also reverse due to the inversion symmetry of the materials, thus:

$$\begin{aligned} -\tilde{P}(t) &= \epsilon_0\left[\chi^{(1)}[-\tilde{E}(t)] + \chi^{(2)}[-\tilde{E}(t)]^2 + \chi^{(3)}[-\tilde{E}(t)]^3 + \cdots\right] \\ &\equiv -\epsilon_0\left[\chi^{(1)}\tilde{E}(t)] + \chi^{(2)}[\tilde{E}(t)]^2 - \chi^{(3)}[\tilde{E}(t)]^3 + \cdots\right] \end{aligned} \tag{2.29}$$

To keep consistence with Eq. (2.28), $\chi^{(2)}$ or other even order terms must be zero. Thus, lack of inversion symmetry of the material is a necessary condition for second-order nonlinear optical properties.

### 2.4.1 Second Harmonic Generation (SHG) and Linear Electro-Optic (LEO)

According to [62], for an incident light with 2 different frequency components, it can be expressed as:

$$\tilde{E}(t) = E_1 e^{-i\omega_1 t} + E_2 e^{-i\omega_2 t} + c.c. \tag{2.30}$$

, where the $\omega_1, \omega_2$ are different frequency and $c.c.$ represents complex conjugated terms.

According to Eq. (2.28), the second-order term can be written as:

$$\begin{aligned} \sum_n P(\omega_n)e^{-i\omega_n t} = \tilde{P}^{(2)}(t) = \epsilon_0\chi^{(2)}\tilde{E}^2(t) = \epsilon_0\chi^{(2)}\{2[E_1E_1^* + E_2E_2^*] + \\ [E_1^2e^{-2i\omega_1 t} + E_2^2e^{-2i\omega_2 t} + 2E_1E_2e^{-i(\omega_1+\omega_2)t} + 2E_1E_2^*e^{-i(\omega_1-\omega_2)t} + c.c.]\} \end{aligned} \tag{2.31}$$

Different components of Eq. (2.31) can be expressed as [62]:

$$
\begin{aligned}
P(2\omega_1) &= \epsilon_0 \chi^{(2)} E_1^2 \ (SHG), \\
P(2\omega_2) &= \epsilon_0 \chi^{(2)} E_2^2 \ (SHG), \\
P(\omega_1 + \omega_2) &= 2\epsilon_0 \chi^{(2)} E_1 E_2 \ (SFG), \\
P(\omega_1 - \omega_2) &= 2\epsilon_0 \chi^{(2)} E_1 E_2^* \ (DFG), \\
P(0) &= 2\epsilon_0 \chi^{(2)} (E_1 E_1^* + E_2 E_2^*) \ (OR)
\end{aligned}
\tag{2.32}
$$

Here the first 2 expression is labeled as second harmonic generation (SHG), the third is sum frequency generation (SFG), followed by difference frequency generation (DFG), and optical rectification (OR). For SHG, we see that the incident beam at frequency $\omega$ is converted to radiation at the second-harmonic frequency $2\omega$. One common use of SHG is to double the frequency of a fixed-frequency laser, such as convert 1064 nm infrared laser into 532 nm green laser. For SFG, if we fix $\omega_1 = \omega$ as the incident beam frequency and $\omega_2 = 0$, it can reflect the change in refractive index depends linearly on applied electric field, as known as the linear electro-optic (LEO) effect or Pockels effect.

Further considering the directions, second nonlinear optical susceptibilities are tensors of order 3, which is:

$$
P^a(\omega_1 + \omega_2) = \chi^{abc}(-\omega_1 - \omega_2; \omega_1, \omega_2) E^b(\omega_1) E^c(\omega_2) \tag{2.33}
$$

As mentioned in last paragraph, SHG and LEO are 2 special cases:

$$
P^a(2\omega) = \chi^{abc}(-2\omega; \omega, \omega) E^b(\omega) E^c(\omega) \quad \text{(SHG)} \tag{2.34}
$$

$$P^a(\omega) = 2\chi^{abc}(-\omega;\omega,0)E^b(\omega)E^c_{dc} \qquad \text{(LEO)} \tag{2.35}$$

Here the $E_{dc}$ is the actual direct current field. At zero frequency, we have

$$\lim_{\omega\to 0}\chi^{abc}(-2\omega;\omega,\omega) = \lim_{\omega\to 0}\chi^{abc}(-\omega;\omega,0) \tag{2.36}$$

a statement of the equivalence of the SHG and LEO susceptibilities at $\omega = 0$ [107].

For the detailed expression [107]–[110], we need to define the dipole transition matrix element between two states *i* and *j* at the $\boldsymbol{k}$ point which can be calculated by DFT

$$p^a_{ij} = \langle \boldsymbol{k}j|\hat{p}_a|\boldsymbol{k}i\rangle \tag{2.37}$$

And the position operator matrix element

$$r^a_{nm}(\boldsymbol{k}) = \begin{cases} \frac{p^a_{nm}(\boldsymbol{k})}{im\omega_{nm}}, & n \neq m \\ 0, & n = m \end{cases} \tag{2.38}$$

The linear susceptibility can be then written as [107]:

$$\chi^{abc}_I(-\omega;\omega) = \frac{e^2}{\hbar}\sum_{nmk} f_{nm}\frac{r^a_{nm}(\boldsymbol{k})r^b_{mn}(\boldsymbol{k})}{\omega_{mn}(\boldsymbol{k}) - \omega} \tag{2.39}$$

The SHG $\chi^{abc}(-2\omega;\omega,\omega)$ can generally be written in the form [107], [109]:

$$\chi^{abc}(-2\omega;\omega,\omega) = \chi^{abc}_{II}(-2\omega;\omega,\omega) + \eta^{abc}_{II}(-2\omega;\omega,\omega) + \sigma^{abc}_{II}(-2\omega;\omega,\omega) \tag{2.40}$$

, in which

$$\chi_{II}^{abc}(-2\omega;\omega,\omega)=\frac{e^3}{\hbar^2}\sum_{nml}\int\frac{d\boldsymbol{k}}{8\pi^3}\frac{r_{nm}^{a}\{r_{ml}^{b}r_{ln}^{c}\}}{\omega_{ln}-\omega_{ml}}\left\{\frac{2f_{nm}}{\omega_{mn}-2\omega}+\frac{f_{ml}}{\omega_{ml}-\omega}+\frac{f_{ln}}{\omega_{ln}-\omega}\right\} \tag{2.41}$$

$$\eta_{II}^{abc}(-2\omega;\omega,\omega)=\frac{e^3}{\hbar^2}\int\frac{d\boldsymbol{k}}{8\pi^3}\left\{\sum_{nml}\omega_{mn}r_{nm}^{a}\{r_{ml}^{b}r_{ln}^{c}\}\left\{\frac{f_{nl}}{\omega_{ln}^2(\omega_{ln}-\omega)}+\frac{f_{lm}}{\omega_{ml}^2(\omega_{ml}-\omega)}\right\}\right.$$
$$\left.-8i\sum_{nm}\frac{f_{nm}r_{nm}^{a}}{\omega_{mn}^2(\omega_{mn}-2\omega)}\{\Delta_{mn}^{b}r_{mn}^{c}\}+\frac{2\sum_{nml}f_{nm}r_{nm}^{a}\{r_{ml}^{b}r_{ln}^{c}\}(\omega_{ml}-\omega_{ln})}{\omega_{mn}^2(\omega_{mn}-2\omega)}\right\} \tag{2.42}$$

$$\sigma_{II}^{abc}(-2\omega;\omega,\omega)=\frac{e^3}{2\hbar^2}\int\frac{d\boldsymbol{k}}{8\pi^3}\left\{\sum_{nml}\frac{f_{nm}}{\omega_{mn}^2(\omega_{mn}-\omega)}[\omega_{nl}r_{lm}^{a}\{r_{mn}^{b}r_{nl}^{c}\}-\omega_{lm}r_{nl}^{a}\{r_{lm}^{b}r_{mn}^{c}\}]\right.$$
$$\left.+i\sum_{nm}\frac{f_{nm}r_{nm}^{a}\{\Delta_{mn}^{b}r_{mn}^{c}\}}{\omega_{mn}^2(\omega_{mn}-\omega)}\right\} \tag{2.43}$$

, where $\Delta_{mn}^{a}=\frac{P_{mm}^{a}(k)-P_{nn}^{a}(k)}{m}$, and the first term $\chi_{II}^{abc}(-2\omega;\omega,\omega)$ is the interband contribution, describing a pure interband transition between different band on the same momentum $\boldsymbol{k}$; the second term $\eta_{II}^{abc}(-2\omega;\omega,\omega)$ is the intraband contribution, describing the contribution from the modulation of the linear susceptibility by the intraband motion of the electrons; the third term $\sigma_{II}^{abc}(-2\omega;\omega,\omega)$ called modification contribution, represents that portion of the susceptibility resulting from the modification of the intraband motion by the polarization energy associated with the interband [89], [90]. The linear electro-optic coefficient $r_{abc}(\omega)$ is connected to the LEO susceptibility $\chi_{abc}^{(2)}(-\omega,\omega,0)$ at zero frequency limit as:

$$r_{abc}(\omega) = -\frac{2}{n_a^2(0)n_b^2(0)} \lim_{\omega \to 0} \chi_{abc}^{(2)}(-\omega; \omega, 0) = -\frac{2}{n_a^2(0)n_b^2(0)} \lim_{\omega \to 0} \chi_{abc}^{(2)}(-2\omega; \omega, \omega) \quad (2.44)$$

Where $n_a(0)$ is the refraction index in a direction at zero frequency and $n_a^2(0)$ equals dielectric constant $\varepsilon_a(0)$. Besides, for low frequency region below the bandgap, $\chi_{abc}^{(2)}(-2\omega, \omega, \omega)$ and $n(\omega)$ are nearly constant so that the linear electro-optic coefficient $r_{abc}(\omega) \approx r_{abc}(0)$ [78].

### 2.4.2 Scissor Approximation

As mentioned in 2.2, DFT always underestimate band gap, therefore scissors approximation [111] has been suggested to modify the DFT band gap with more accurate values, such as quasiparticle band gap, experimental gap or band gap calculated by other methods. The only modification is the energy difference [107]:

$$\omega_{mn} \to \omega_{mn} + \frac{\Delta}{\hbar}(\delta_{mc} - \delta_{nc}) \quad (2.45)$$

Meanwhile the matrix elements of the position operator will not change. Since in practical calculation, we will use dipole transition matrix $\boldsymbol{p}_{mn}$ rather than the position operator $\boldsymbol{r}_{mn}$, we need to normalize $\boldsymbol{p}_{mn}$ as:

$$\widetilde{\boldsymbol{p}}_{mn} = \boldsymbol{p}_{mn} \frac{\omega_{mn} + \frac{\Delta}{\hbar}(\delta_{mc} - \delta_{nc})}{\omega_{mn}} \quad (2.46)$$

Substitute the original expression in Eq. (2.39)~(2.43) , we can include scissor approximation in our second-order nonlinear optical calculations.

# Chapter 3: Quasiparticle and Optical Spectra of Strained Materials

## 3.1 Introduction

Strain is known for impacting a wide range of properties of semiconductors and thus it is useful to tailor materials for various applications [27]–[30], [32], [33], [112]. However, experimentally controllable strain engineering is still challenging. In particular, stretching or bending 2D structures usually introduces spatially inhomogeneous strain, as shown in schematics of Figure 3.1(a). These complicated strain distributions, which are beyond the scope of simple uniaxial or biaxial cases, will surely affect local electronic structures and optical properties, bringing uncertainty for strain engineering [28], [29], [37], [38]. Moreover, complicated strain distribution is widely expected in fabricated samples. Interestingly, those epitaxial samples exhibit various local properties: inhomogeneous free-carrier distributions and photoluminescence (PL) have been observed [113], [114]. Given the important roles of substrates, edge reconstructions, and domain walls, strain may be inevitable in those fabricated samples. In this sense, connecting optical or electrical inhomogeneity to spatial strain distributions is an effective way to understand these epitaxial processes and local structures, giving hope to further optimizing fabrications.

Different from arbitrary or even inhomogeneous strain realized in experiments, most calculations have focused on relatively simple cases, such as uniaxial/biaxial strains along specific high-symmetry directions [39]–[41]. While uniaxial or biaxial strain decides many important properties, they are not enough for covering those experimentally strained conditions: the strain may be applied with differently amplitudes along different directions because of substrates or various boundary conditions, which are common in fabricated samples. Thus, a study covering

arbitrarily axial strain is necessary and essential to explore the 2D strain-mapping properties, which is also important to fill a hole of previous studies.

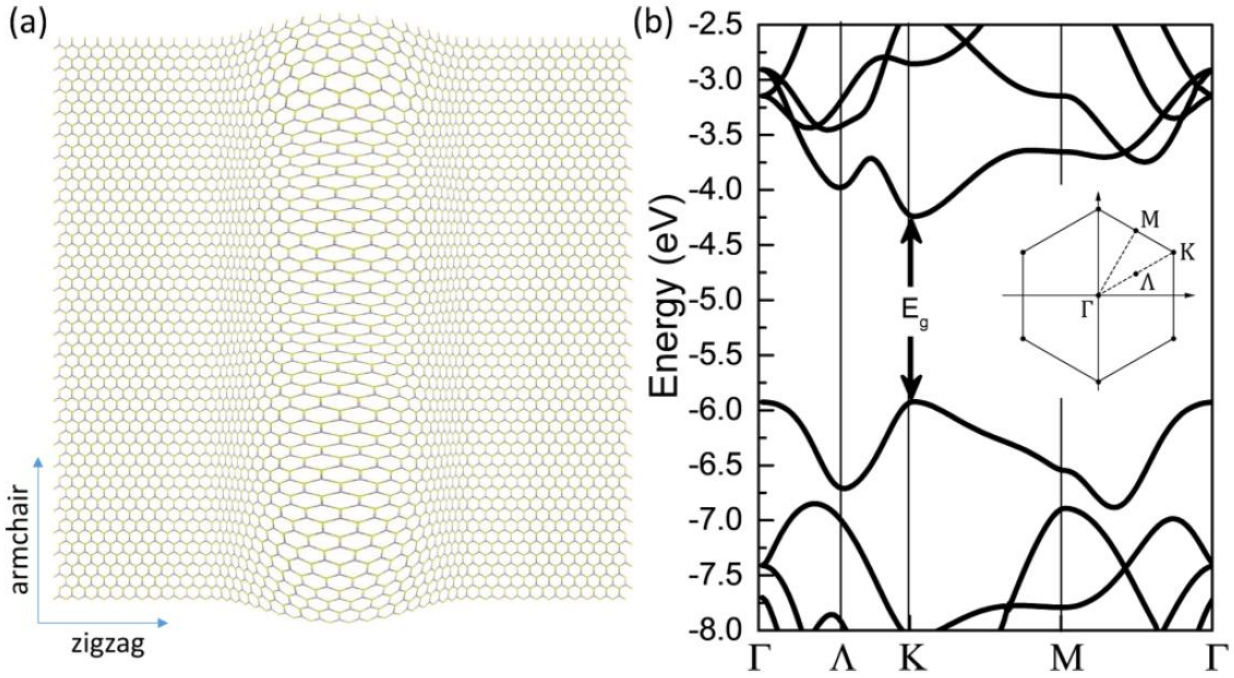


Figure 3.1 (a) Schematic plot of the top view of inhomogeneously strained monolayer 2-H phase TMDC. The orthogonal armchair and zigzag directions are specified, respectively. To show atomic structures, the spatial size of plotted local strain domains is much smaller than that of realistic samples, which is around micrometers. (b) DFT-calculated band structure of monolayer $MoS_2$. The band energy is aligned to the vacuum level. The inset is the first BZ with high-symmetry points marked.

Moreover, typical first-principles calculations are based on (DFT), but the aforementioned PL and band energies are essentially excited-state properties, requiring including many electron effects beyond DFT. Therefore, a first-principles calculation considering complicated strain conditions and including many-electron effects is essential for explaining a wide range of measurements and guiding future strain engineering of materials.

In this chapter, we will first study theoretically the structural and electronic response of layered bulk black phosphorus to in-layer 2D strain. This part is co-authored with Dr. Jie Guan and Dr. David Tománek [81] , in which our main contribution is quasi-particle calculation of strained

layered bulk black phosphorus. To correctly describe the dependence of the fundamental band gap on strain, we used the computationally more involved GW quasiparticle approach that is free of parameters and is superior to DFT studies, which are known to underestimate gap energies. After that, we apply the first-principles DFT and many body perturbation theory to obtain quasiparticle energies and bright excitons of four strained typical TMDC monolayers, *i.e.*, $MoS_2$, $MoSe_2$, $WS_2$, and $WSe_2$ [82]. By mapping their band gaps, absolute band-edge energies, and exciton frequencies into 2D contours of in-plane strain distributions, we are able to provide a complete picture of arbitrary strain effects on these important quantities. Combining the high spatial resolution of PL spectra with our calculated exciton energies, experimentalists may understand the observed inhomogeneous PL measurements and further quantify the local strain condition.

## 3.2 Computational Methods

DFT with the Perdew-Burke-Ernzerhof (PBE) functional is employed to calculate the ground-state properties. Normconserving pseudopotentials are used to approximate the core-electron effects on the electronic structure and excited-state properties.

### 3.2.1 Black Phosphorus

For black phosphorus, a $8 \times 8 \times 4$ *k*-grid sampling and 180 Ry energy cutoff are used for DFT calculation [81], implemented in SIESTA code [115] to optimize the structure and to determine the structural response to in-plane strain. GW approximation is implemented with BerkeleyGW packages [99] on top of DFT calculation in Quantum Espresso [116]. We have expanded the dielectric matrix in plane waves up to a cutoff energy of 10 Ry. The quasiparticle energies are determined by considering the lowest 158 unoccupied conduction bands and accounting for all

higher-lying bands using the modified static-remainder approximation [117]. We use single-shot $G_0W_0$ calculations with a 14 × 10 × 4 *k*-point grid, which provide converged results.

### 3.2.2 2D TMDCs

For 2D TMDCs, Only the 2H phase is considered in this work. The atomic structure is fully relaxed according to the DFT/PBE-calculated force and stress. A 70 Ry plane-wave truncation and an 18 × 18 × 1 *k*-grid sampling in the first Brillouin zone (BZ) of the intrinsic hexagonal unit cell are adopted for calculating fully converged ground-state properties. For strained calculations, we take a rectangle cell with 12 × 21 × 1 *k* point. The quasiparticle energies are obtained by the first-principles single-shot $G_0W_0$ approximation [89] and subsequently excitonic effects and optical absorption spectra are obtained from solving the Bethe-Salpeter equation (BSE) within the Tam-Dancoff approximation [97]. The involved unoccupied band number is more than 10 times that of valence bands to achieve the converged dielectric function. The excitonic effects are included by solving the BSE with a fine *k*-point grid of 36 × 63 × 1.

## 3.3 Quasiparticle Band Gap of Strained Black Phosphorus

The DFT-level strain-induced structural changes can be found in reference [81] Part. III. A, which is the work of co-author Dr. Jie Guan and Dr. David Tománek.

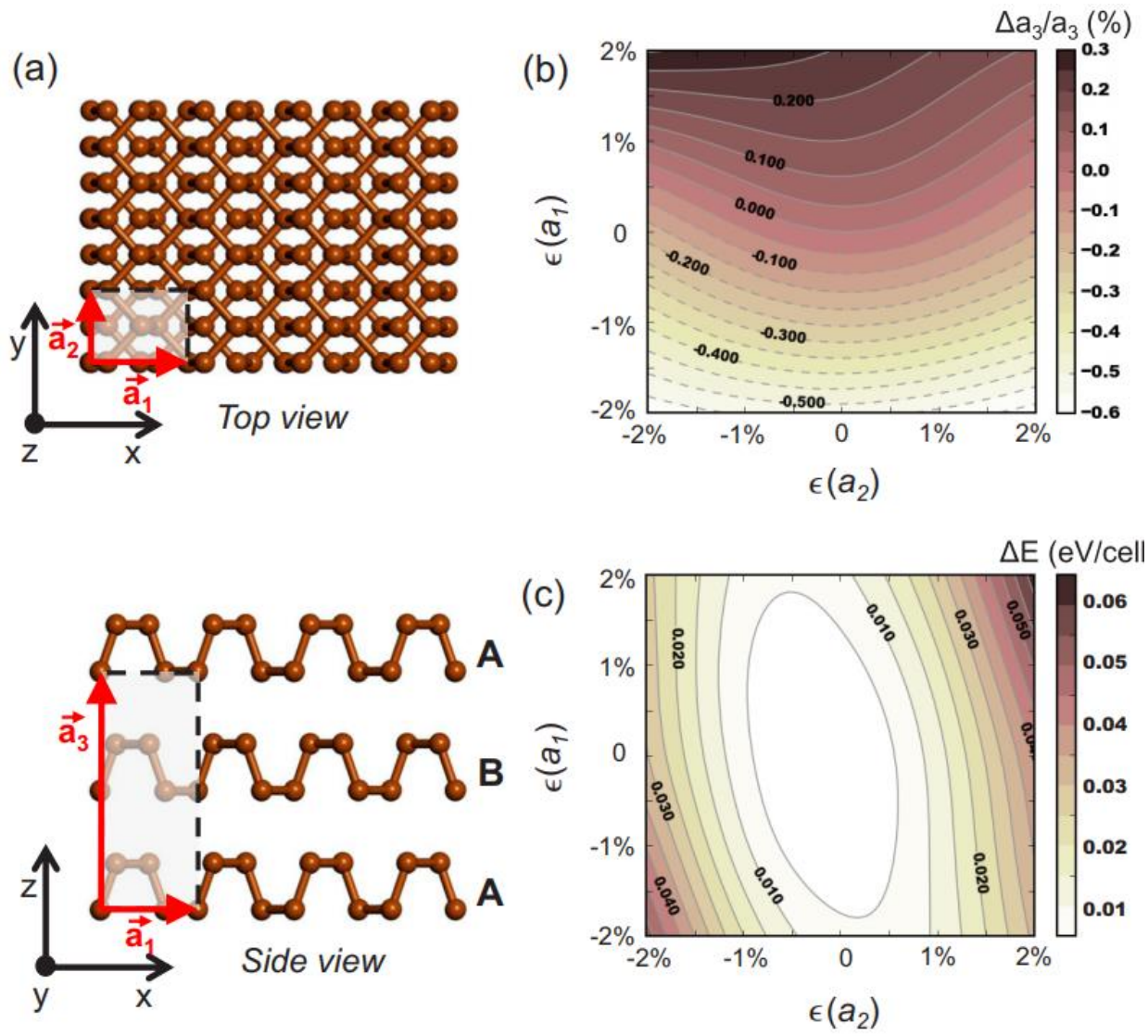


Figure 3.2 (a) Ball-and-stick model of the structure of bulk black phosphorus in top and side views. (b) Fractional change of the interlayer distance $\overrightarrow{a_3}$ as a function of the in-layer strain along the $\overrightarrow{a_1}$ and $\overrightarrow{a_2}$ directions. (c) Dependence of the strain energy $\Delta E$ per unit cell on the in-layer strain along the $\overrightarrow{a_1}$ and $\overrightarrow{a_2}$ directions

Here we focus on strain-induced changes of electronic structures involved with GW calculation. In DFT calculation with SIESTA [81], the intrinsic unstrained bulk black phosphorus has an extremely small direct fundamental band gap value $E_g$(PBE) $\approx$ 0.05 eV. However, Quantum Espresso will lead to an overlapping between the top of conduction band and the bottom of valence band under that condition, making GW correction inapplicable since BerkeleyGW cannot break the band topology in order to open a closed bandgap. To solve this problem, we

apply moderate strains (~3%) to force a finite band gap of black phosphorus at DFT level, then do GW calculation based on those opened band gap [118]. Eventually we extrapolate the obtained GW band gaps under different strains back to zero-strain intercept, as shown in the schematic diagram Figure 3.3. As a result, we obtain a quasiparticle band gap 0.35 eV in unstrained bulk black phosphorus, very close to the observed value around 0.33 eV [119].

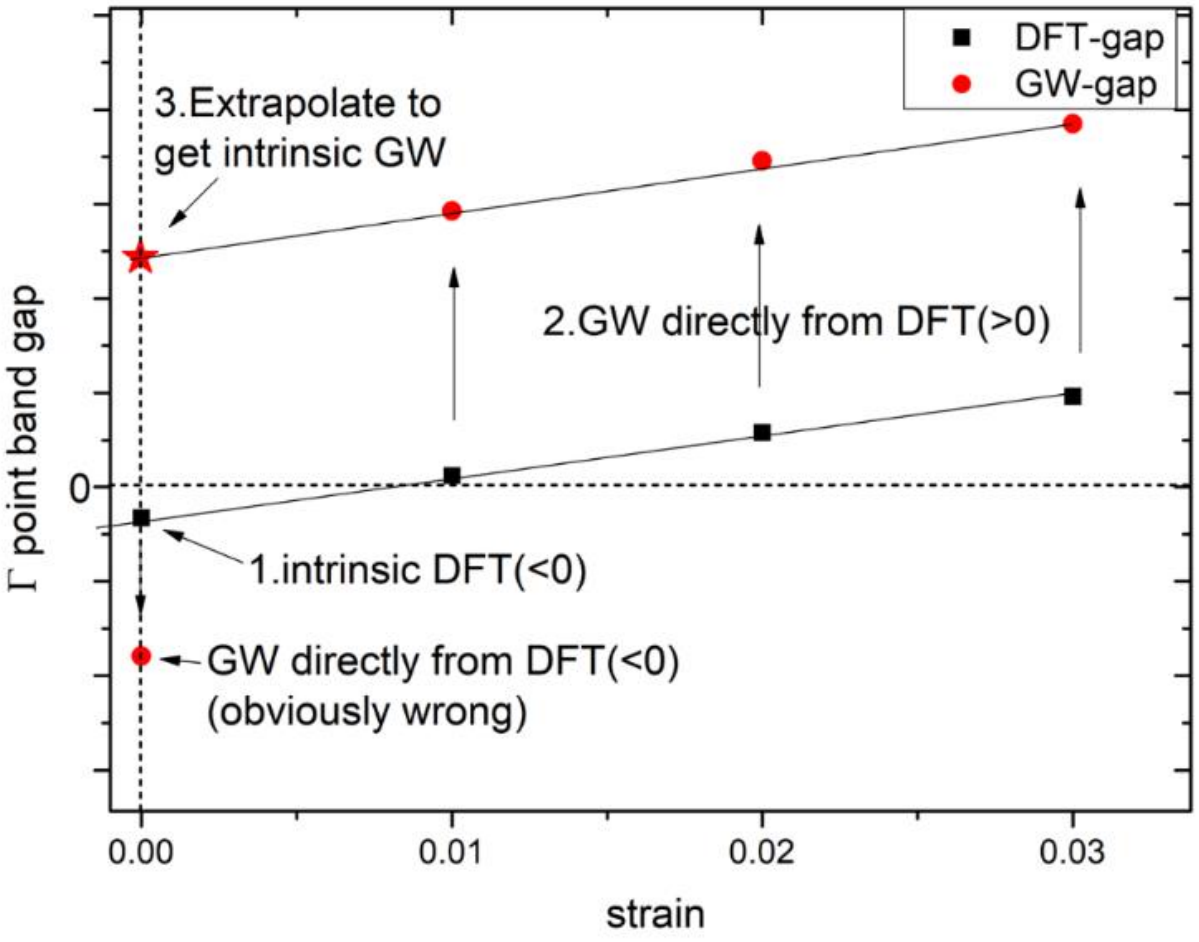


Figure 3.3 Schematic diagram represents how we 1. apply moderate strains to force a finite band at DFT level, then 2. do GW calculation on these finite DFT bands, 3. then extrapolate back to get intrinsic GW band gap at zero strain.

The calculation for electronic band structure and density of states (DOS) of unstrained and strained bulk black phosphorus are shown in Figure 3.4.

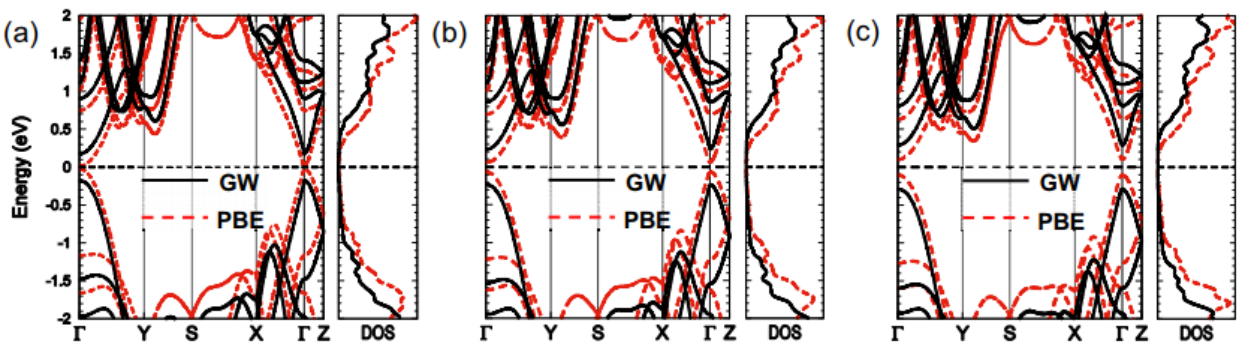


Figure 3.4 Electronic band structure (left panels) and density of states (right panels) of bulk black phosphorus (a) without strain, (b) when stretched by 1% along the $\vec{a}_1$ direction, and (c) when stretched by 2% along the $\vec{a}_1$ direction. GW results are shown by the solid black lines. DFT-PBE results, which underestimate the band gap, are shown by the dashed red lines.

A more precise comparison between the quasiparticle spectra and DFT eigenvalues reveals that the difference $E_{qp} - E_{PBE}$ does depend on the energy but is independent of the crystal momentum $\boldsymbol{k}$. For 1% strain along $\vec{a}_1$, we find that the quasiparticle energies display a linear relationship with DFT eigenvalues, as shown in Figure 3.5(a), given by

$$\begin{aligned} E_{qp}(CB) &= 1.10 \times E_{PBE}(CB) + 0.11\ eV \\ E_{qp}(VB) &= 1.07 \times E_{PBE}(VB) - 0.18\ eV \end{aligned} \tag{3.1}$$

Compare DFT and GW values at different strains, we find that the modulation of band gap $\Delta E_g(PBE) \approx \Delta E_g(qp)$ is the same up to $\leq 0.01\ eV$ in the strain range here. Thus, we can deduce the GW band gap at different strain based on DFT band gap with Eq. (3.1). The results, based on a cubic spline interpolation of a $5 \times 5$ grid of strain map, are shown in Figure 3.5(b).

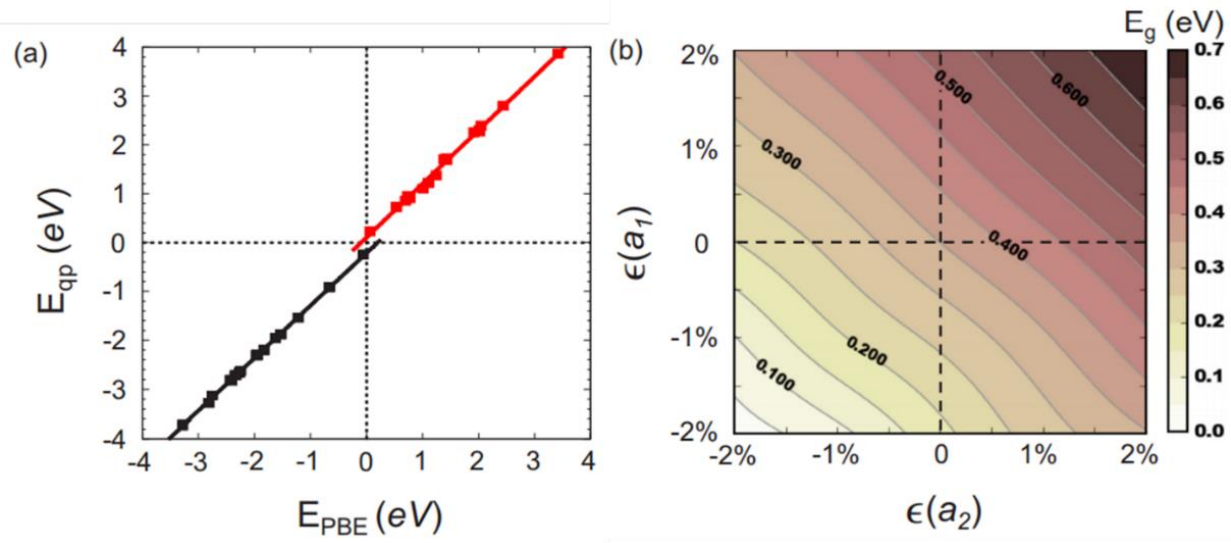


Figure 3.5 (a) Correlation between quasiparticle (GW) energies $E_{qp}$ and Kohn-Sham energy values $E_{PBE}$, obtained using the DFT-PBE functional, for states along high symmetry lines in the Brillouin zone. The straight lines in the valence and conduction band regions are drawn to guide the eye. The results represent bulk black phosphorus subject to strain values $\epsilon(\vec{a}_1) = 1\%$ and $\epsilon(\vec{a}_2) = 0\%$. The Fermi level is at zero energy. (b) Dependence of the quasiparticle (GW) electronic band gap $E_g$ on the in-layer strain applied along the $\vec{a}_1$ and $\vec{a}_2$ directions.

The results indicate that, the band gap $E_g$ of bulk black phosphorus varies smoothly between 0.05 and 0.70 eV. Independent of the in-plane strain direction, $E_g$ increases upon stretching and decreases upon compression. With the nearly equidistant spacing between the contour lines in Figure 3.5(b), we can extrapolate to larger strains and expect the band gap to close at compressive strains along both directions exceeding 2% and band gap even vanishes at compressive strain values exceeding 2%. This result agrees with 2D black phosphorene under strain [120], [121], which results from accumulating charge around 3*p* orbitals of P atoms. The sensitivity of band gap dependence on -in-layer strain suggests a possible application of black phosphorus in strain-controlled infrared devices.

## 3.4 Excited-State Properties of Strained 2D TMDCs

For 2D TMDCs, we take monolayer $MoS_2$ as an example. Its intrinsic band structure calculated by DFT is presented in Figure 3.1(b). Here we choose hexagonal unit cell, and the first BZ and

those important high-symmetry points (including the Λ point) in the reciprocal space are plotted as well. We observe a direct band gap located at the $K(K')$ point in suspended monolayer $MoS_2$. The in-plane strain is included through a 2D grid, which is expanded by the orthogonal armchair and zigzag directions, which are marked in Figure 3.1(a), on a rectangle unit cell. The strain magnitude covers the range from $-5$ to 5% along each direction with a step of 0.5%, forming a $21 \times 21$ grid to describe strain conditions. The electronic structures and optical spectra will be calculated under each strain condition. As a result, this study covers not only uniaxial and biaxial strain cases but also all possible arbitrarily axial strain cases that are observed in fabricated samples. Finally, the linear interpolation scheme will be employed to smooth the 2D contour plots.

### 3.4.1 Sensitivity of SOC and Many-body Correction under Strain

There are several factors that will influence our results. First, spin-orbit coupling (SOC) is significant in these monolayers. For example, the SOC splitting of the valence-band maximum (VBM) of monolayer $WS_2$ is around 425 meV [122], definitely affecting the band-edge energies and excitons. Fortunately, we have checked that, although SOC is not negligible, it is not very sensitive to applied strain. For instance, the SOC splitting of the valence-band edge at the *K* point is around 140 meV for monolayer $MoS_2$ and the variation of SOC is less than 10 meV when applied strain is within our studied range (±5%). Thus, in the following we will directly include fixed SOC corrections into the band gaps and exciton energies for strained 2D structures.

Another challenge is to obtain the quasiparticle energies and excitons for strained structures. Due to the hardness of calculating GW-BSE, it is nearly formidable to perform the brute-force GW-BSE calculation for excited-state properties of the $21 \times 21$ strained structures. Nevertheless,

many-electron effects can be regarded as higher-order corrections, therefore in our strain region, many-electron corrections may not change substantially.

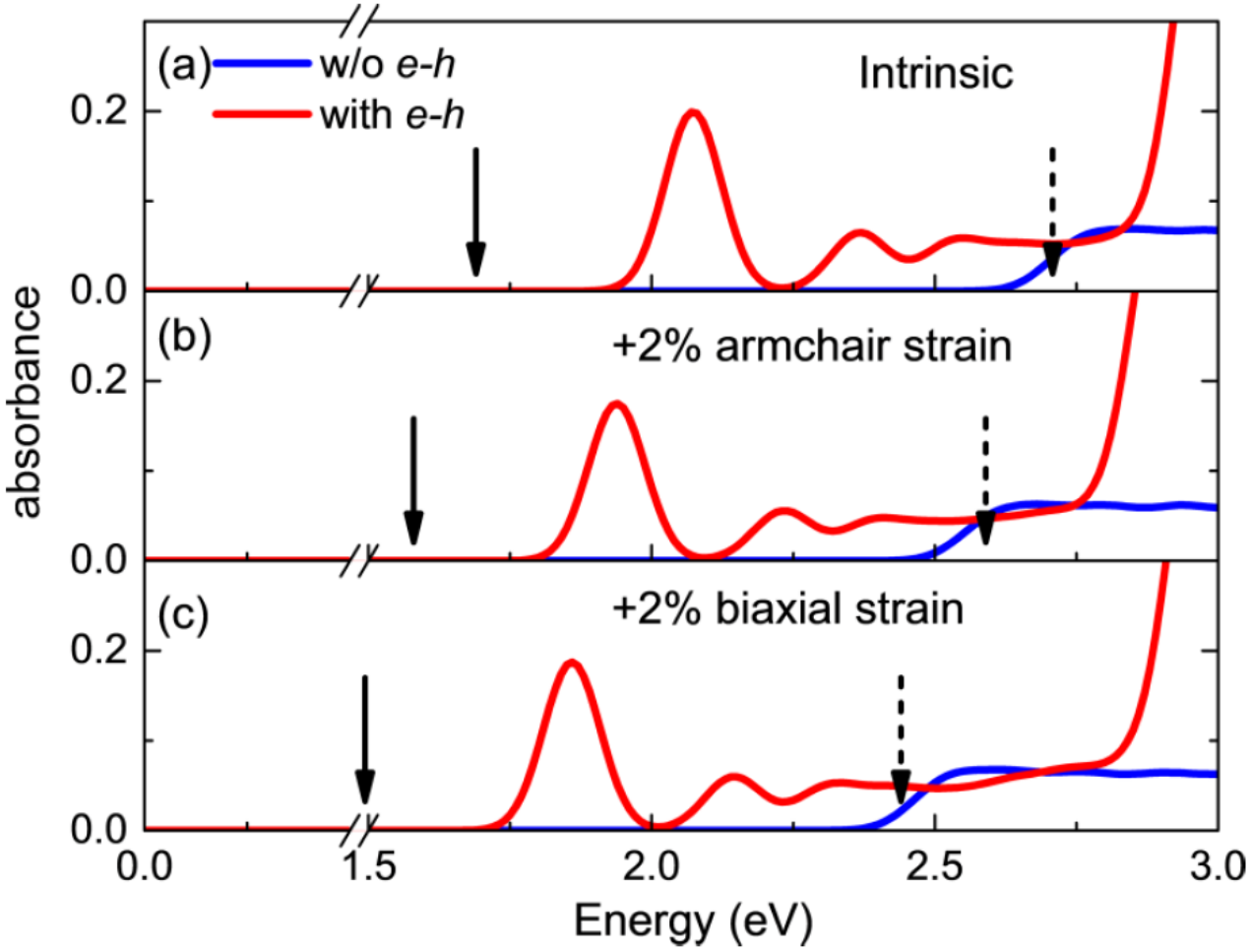


Figure 3.6 (a)–(c) Optical absorption spectra of intrinsic, +2% uniaxially strained, and +2% biaxially strained monolayer $MoS_2$. The blue curves are optical absorption spectra without e-h interactions included and the red curves are those with e-h interactions included. The DFT band gap ($E_g^{DFT}$) and GW-calculated quasiparticle band gap ($E_g^{GW}$) are marked with solid and dashed arrows, respectively.

To confirm this, we calculate the quasiparticle band gaps and optical spectra of intrinsic monolayer $MoS_2$ and two typical strained cases (+2% uniaxial and +2% biaxial cases), as included in Table 3.1 and Figure 3.6. The SOC is not included here because we mainly want to compare the difference induced by strain and, moreover, SOC is not significantly changed by many-electron effects in these monolayers [123]. Substantial self-energy corrections and

excitonic effects have been observed in all these monolayers. Our calculated quasiparticle band gap and optical absorption spectrum of intrinsic monolayer $MoS_2$ are consistent with previous studies [124], [125].

Table 3.1 The DFT calculated band gaps (at the K point), quasiparticle band gaps (at the K point), and the lowest, bright exciton energies intrinsic and strained monolayer $MoS_2$ (SOC is not included).

| Strain | DFT (eV) | GW (eV) | Exciton (eV) |
|---|---|---|---|
| Intrinsic | 1.69 | 2.71 | 2.07 |
| +2% armchair | 1.58 | 2.59 | 1.94 |
| +2% biaxial | 1.47 | 2.44 | 1.86 |

We can find that many-electron corrections are essentially insensitive to the applied strain, as shown in Table 3.1, all GW correction are around 1 eV and exciton energy shift are around 0.36 eV, with error tolerance less than 5%. Therefore, we only need to calculate the electronic self-energy corrections and excitonic effects of intrinsic materials. They are used to rigidly shift the quasiparticle band gaps and excitonic energies of monolayer TMDCs within moderate strain. More strain conditions are calculated to confirm this rigid shift, and the error bar of the rigid shift is shown to be less than 0.1 eV, making it reasonable for applying rigid shifts to all quasiparticle band gaps and exciton energies.

### 3.4.2 Quasiparticle Band Structures for 2D $MoS_2$ under Strain

We first focus on excited-state properties of strained monolayer $MoS_2$. Its contour of the quasiparticle band gap with SOC included is presented in Figure 3.7(a). Significant variations of the band gap are observed: within this ±5% strain range, the band gap can be changed from 1.7 to 2.8 eV (the intrinsic band gap is 2.6 eV). The band gap is particularly sensitive to both the

magnitude of the applied strain and how the strain is applied. Interestingly, the most efficient way to tune the band gap is the widely studied one, the biaxial stretching. This can be seen from that the steepest sloping direction in Figure 3.7(a) is along the diagonal direction from the origin to the right-up corner. On the other hand, along the orthogonal direction to the biaxial strain, the band-gap variation is, however, the minimum. Based on those isolines in Figure 3.7(a), we can conclude that when the 2D structure is stretched along one direction and compressed along the other orthogonal direction, its variation of the band gap is small. In other words, the conservation of the in-plane area can minimize the band-gap variation in strained TMDCs.

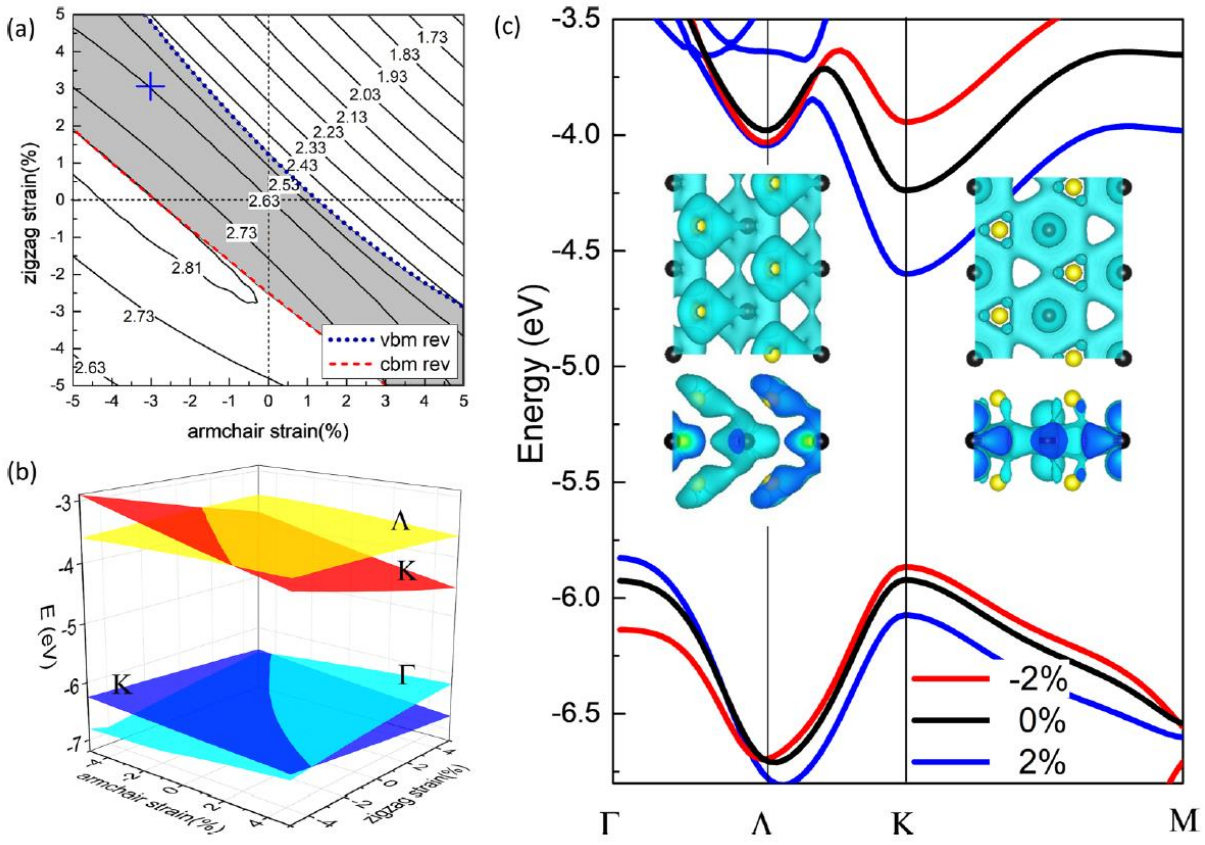


Figure 3.7 (a) 2D contour plot of the quasiparticle band gap in arbitrarily strained monolayer $MoS_2$. The indirect band-gap area is marked by the gray color. (b) 3D contour plot of the absolute band energies of those crucial high-symmetry points. (c) Variation of the band structure according to the ±2% biaxial strain. The top view and side view of the 3D contours of the wave functions of the conduction states at the *Λ* and *K* points are plotted, respectively.

From 5% to -5%, the biaxial strain effect is highly asymmetric: the band gap is not changed substantially for the compressing case. This is actually a result of switching band edges, thus leading to transformation from direct to indirect bandgap. In Figure 3.7(a), we present a complete picture of strain effect for such a direct-indirect band gap transition in monolayer $MoS_2$. The gray area stands for the strain condition for holding a direct band gap and the white area stands for that of an indirect band gap. Particularly, Figure 3.7(a) shows that even under significant stretch along one direction, monolayer TMDCs may still hold the direct band gap if it is allowed for shrinking along the orthogonal direction, e.g., the blue cross.

The above direct-indirect band-gap transitions are essentially from the competitions between band edges at those high-symmetry points, marked in Figure 3.1(b). In Figure 3.7(b), we have plotted the three-dimensional (3D) contour plot of the absolute quasiparticle energies of the valence and conduction band edges of those relevant high-symmetry points, according to the vacuum level. We can see that there are energy crossings between those band edges. At some critical strain, valence-band maximum (VBM) and conduction-band minimum (CBM) will be shifted from $K$ point to $\Gamma/\Lambda$ point, resulting in a switch of direct/indirect band gap.

To understand the different strain responses of these band edges at high-symmetry points, we use a schematic way to qualitatively analyze the different strain responses. Let us take an example of local conduction band minimum at the $\Lambda$ and $K$ points. We have plotted the three-dimensional isosurface plots of their wave functions in Figure 3.7(c). The electronic state at the $\Lambda$ point is more localized and the overlap between neighboring unit cells is small. On the other hand, the wave function at the $K$ point is more delocalized and has a significant overlap between neighboring unit cells. As a result, the wave function at the $\Lambda$ point will not be that sensitive to the change of in-plane distance between atoms, compared to strong overlapped state at $K$ point.

This is also consistent with the results in Figure 3.7 (b), in which the energy of the state at the Λ point is nearly fixed while that of the state at the $K$ point is varied substantially according to strain.

This arbitrary strain effect on the absolute band-edge energies is useful for understanding the recently observed inhomogeneous carrier density in monolayer TMDCs [113], [114]. Due to the substrate effect or ripple structures, those samples may have inevitable locally complicated strain distributions, which may be neither uniaxial nor biaxial. In particular, for those triangular-shape samples epitaxially growing on $SiO_2$/Si substrate, the strain may be accumulated at the corners or edges, inducing a significant shift of the absolute band-edge energy and subsequent inhomogeneous free-carrier distributions [126]. For example, according to Figure 3.7 (b), the accumulations of electrons or holes may indicate a locally biaxial stretching strain condition because that strain condition can efficiently decrease the CBM or increase the VBM.

### 3.4.3 Excitons of 2D TMDCs under Strain

The GW-BSE calculated energies of the brightest exciton in all four types of monolayer 2H-phase TMDCs, *i.e.*, $MoS_2$, $MoSe_2$, $WS_2$, and $WSe_2$, according to arbitrarily axial strain are presented in Figure 3.8. From these 2D contour plots, we can see that strain can significantly modify the PL frequency. Importantly, within our strain range (±5%), the optical response edge can be tuned from the visible light range to the near-infrared one (~1.3 eV). This will be useful for broad physics and biological applications [127]. Meanwhile, the PL peak is strongly impacted by the direct/indirect band gap and it is expected that the PL intensity will be substantially quenched for those indirect band-gap regions. Therefore, we mark the direct-indirect band-gap transition regimes in Figure 3.8 to guide strain engineering for optical applications. Monolayer $MoSe_2$ seems to be the most robust direct-gap TMDC under strain. It

can hold the direct band-gap exciton for compress strain up to 1.5% or the stretching strain up to 3.5%. On the contrary, intrinsic monolayer $WSe_2$ is almost an indirect band-gap 2D semiconductor. Interestingly, it is always an indirect-gap semiconductor under compress and a direct-gap one under stretch.

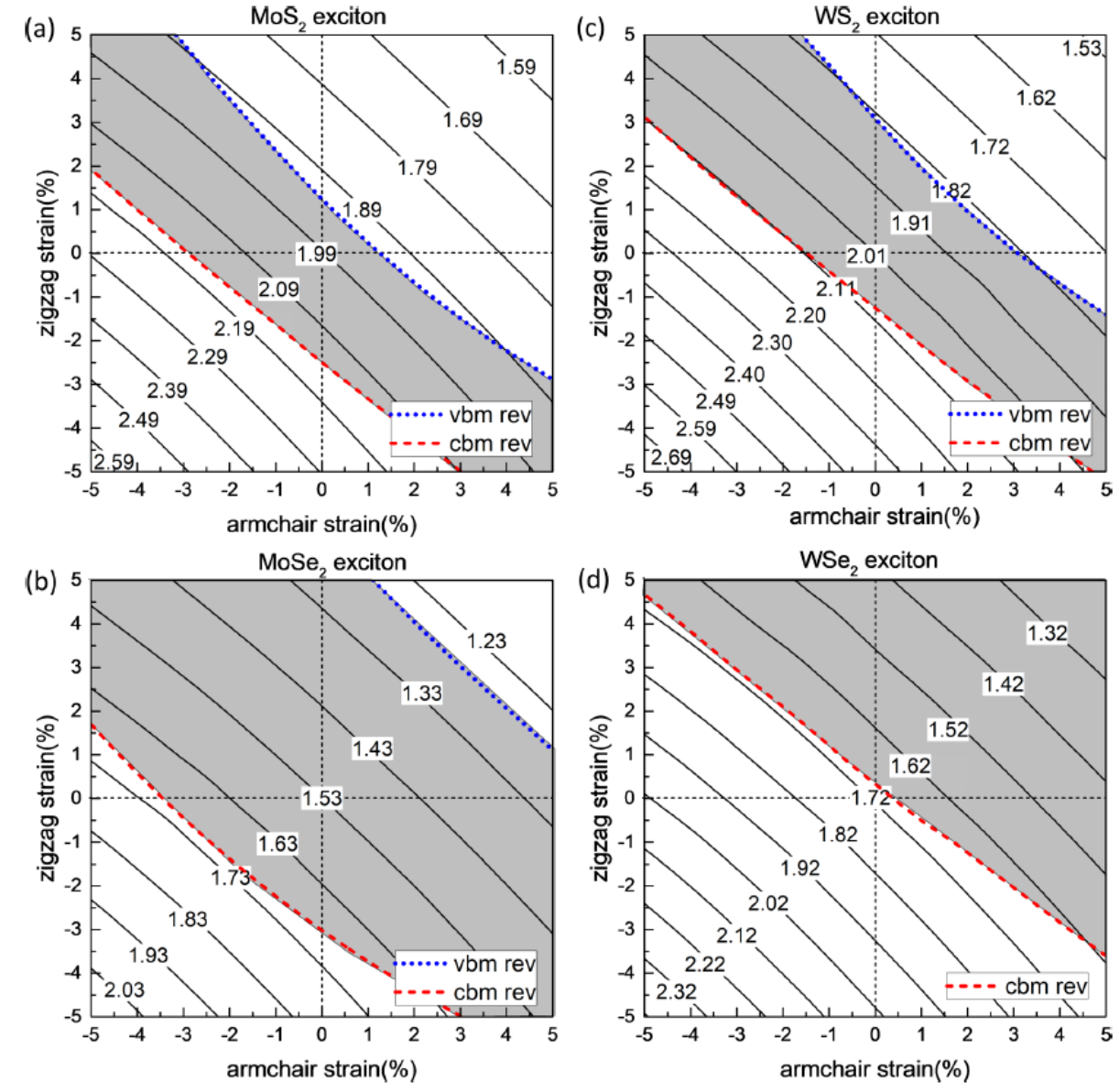


Figure 3.8 Contour plots of the excitation energy of the lowest-energy bright exciton of strained monolayer $MoS_2$ (a), $WS_2$ (b), $MoSe_2$ (c), and $WSe_2$ (d). The direct band-gap regions are marked by the gray area. SOC is approximately included as a constant correction. The temperature effect is not included.

The exciton energy according to complicated strain in Figure 3.8 is useful to understand recent optical measurements. To date, the techniques for obtaining PL spectra with a high spatial resolution have been highly developed and applied for studying epitaxially grown samples [126]. In addition to the inhomogeneous carrier distributions, the local strain condition may also be responsible for the shift of the frequency of the PL peak with a spatial resolution. Therefore, our results in Figure 3.8 will be of help to understand the local strain distribution. Moreover, combined with the strain-induced variation of the band-edge energy and exciton energy, it is possible to design strain distribution to accumulate optically excited excitons and realize high-efficient light-emission or photovoltaic devices [128].

## 3.5 Summary

First, we have studied theoretically the structural and electronic response of layered bulk black phosphorus to in-layer strain. DFT calculations reveal that the strain energy and interlayer spacing display a strong anisotropy with respect to the uniaxial strain direction. GW quasiparticle approach is implemented to correctly describe fundamental band gap on strain. The band gap depends sensitively on the in-layer strain and even vanishes at compressive strain values exceeding $\approx 2\%$, thus suggesting a possible application of black P in strain-controlled infrared devices.

Second, we have presented excited-state properties, including absolute quasiparticle band energies, band gaps, and the bright exciton peak, for arbitrarily in-plane strain of typical monolayer 2H-phase TMDCs. With many-electron effects included, the complete pictures of these important quantities are described by 2D contours of strain conditions. The mechanism for the competition of band-edge energies and its impact on band gaps are discussed based on first-principles results. The variations of these quantities are crucial for experiments to understand

local strain distribution and free carrier inhomogeneity by optical measurements. The predicted arbitrary strain effects are also helpful for strain engineering of transport and optical properties.

# Chapter 4: Off-plane Polarization Ordering in Metal Chalcogen Diphosphates (MCDs) from Bulk to Monolayer

## 4.1 Introduction

Ferroelectrics, arising from macroscopic polarization induced by spontaneous ordering of electric dipoles and switchable under external electric field, has attracted extensive attention. The ultrathin ferroelectric (FE) films are obviously the most useful structure for exploring new physics and realizing device applications, such as FE transistors and memories [42]. To date most works on ferroelectrics have focused on perovskite oxides, such as $PbTiO_3$ and $BaTiO_3$ [43]–[50]. Unfortunately, their ferroelectricity is extremely sensitive to vertical boundary conditions [51], [52]. As a result, drastic depolarization effects emerge in these three-dimensional structures when they are thinned down, resulting in a suppression of polarization and thus a critical thickness for sustaining the FE state [53], [54]. Realizing ultrathin ferroelectricity is thus known hard to achieve.

Layered van der Waals (vdW) materials may give hope to overcoming this challenge. Two-dimensional (2D) in-plane ferroelectricity has been predicted and observed in monolayer group IV monochalcogenides [55]–[58]. This ignites novel applications, such as giant piezoelectricity [129], [130], bulk photovoltaics, and photostriction [131], [132]. However, the more useful off-plane (vertical) ferroelectricity is still challenging. More recently, a few layered materials have been theoretically predicted to be vertically ferroelectric, such as $In_2Se_3$ [133], 1T-phase $MoS_2$ [134], and $Sc_2CO_2$ with 2D electron/hole [135], although many of these structures are metastable or the ferroelectricity is not intrinsic. On the other hand, experiments reported that metal

chalcogen-diphosphates (MCDs) can be a promising family of ultrathin FE materials: Ferroelectricity is observed in a fabricated bilayer [59]. This may shed light on intrinsically stable 2D structures with off-plane ferroelectricity. However, other measurements claim that ferroelectricity can only exist in samples with much larger thickness of MCDs [60], [61].

In this chapter, we take $CuInP_2Se_6$ [Figure 4.1 (a)], a typical member of the family of layered vdW MCDs, as an example and show that monolayer MCD may sustain a polarization ordering even down to the monolayer [83]. Unlike bulk $CuInP_2Se_6$ which is always FE, we reveal that the vertical boundary conditions are crucial for determining the polarization orders of ultrathin structures: The freestanding (open-circuit) monolayer $CuInP_2Se_6$ is antiferroelectric (AFE) but the closed-circuit (shortcut) monolayer can hold the FE phase as the ground state. Particularly, given the substantial transition energy barrier between AFE and FE states, the FE state can be held as a robustly metastable state of the free-standing monolayer, giving rise to 2D vertical ferroelectricity. Finally, the FE phase transition temperature and electric hysteresis curves of the free-standing monolayer $CuInP_2Se_6$ are obtained by Monte Carlo (MC) simulations [136].

## 4.2 Computational Methods

The relaxed atomistic structures and electronic structures are calculated by density functional theory (DFT) with the generalized gradient approximation using the Perdew-Burke-Ernzerhof (GGA-PBE) functional [92], implemented in the Vienna *ab initio* simulation package (VASP) [137], [138]. The VdW interaction is included through the DFT-D2 method of Grimme [139]. The energy cutoff is 600 eV for structure relaxation and solving the Kohn-Sham equation. We use a 6 × 6 × 1 k-grid sampling in the reciprocal space. A vacuum distance is set to be larger than 20 Å between adjacent mono/few layer(s) for avoiding spurious interactions. The climbing image nudged elastic band (cNEB) [140], [141] method is employed to calculate the transition

states and minimum energy path (MEP). The polarization is obtained by the modern theory of polarization based on the Berry-phase approach [104], [142]. As a validation, we have used the Berry-phase method to calculate spontaneous polarization of a typical MCD FE material, bulk $CuInP_2S_6$ (CIPS), which is 3.20 $\mu C/cm^2$. This is in good agreement with experimental measurements [143], which is 3.5 $\mu C/cm^2$ at 153 K, 3.0 $\mu C/cm^2$ at room temperature, and 2.55 $\mu C/cm^2$ from hysteresis at room temperature.

For the Monte Carlo (MC) simulation [136], the length of steps is set to be 0.2 Å and the number of steps is 20 000. We randomly pick up the direction (positive/negative) of each step with even probability and determine the acceptance using the Metropolis-Hastings algorithm [136]. This process is repeated for about 50 times with a fixed starting point and use the average of final positions as a result. Finally, the whole process is repeated for about 100 times to obtain the converged mean values and standard deviations for estimating error bars. We have verified these simulation parameters by comparing the MC-calculated Curie temperature with the measured values of bulk $CuInP_2Se_6$.

## 4.3 Polarizations and Boundary Conditions

As shown in Figure 4.1 (b), $CuInP_2Se_6$ has two typical low energy structures: One is the FE ordering with all copper atoms at the same side, which is its known bulk structure that exhibits a ferroelectric ground state [143], [144]; the other is the AFE ordering with copper atoms arranged in a line-by-line, up-and-down pattern. This is also a popular structure of many other MCDs, such as bulk $CuCrP_2Se_6$ [144]. Our first-principles calculation confirms that the FE state of bulk $CuInP_2Se_6$ is more stable than the AFE state by an energy difference of ~13 meV/formula unit (f.u.). For the freestanding monolayer $CuInP_2Se_6$, we find that, however, the energy of the AFE state is about 12 meV/f.u. less than FE, making AFE be the rigorously ground state of the

monolayer due to the depolarization effect. In other words, at very low temperature and under perfect equilibrium, the freestanding monolayer $CuInP_2Se_6$ will theoretically stay on an AFE order or form dipole glass [145]–[147].

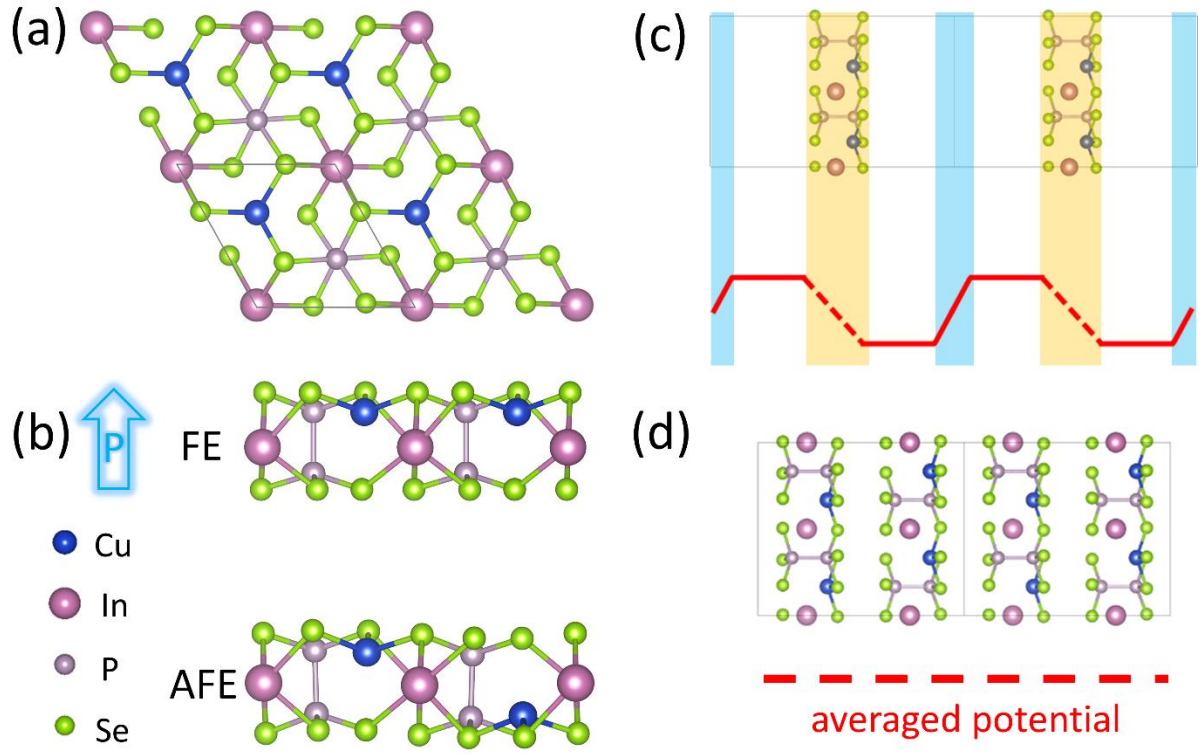


Figure 4.1 (a) Top view of monolayer $CuInP_2Se_6$. (b) Side views of the FE (upper) and AFE (lower) states. (c) Schematic potential of FE monolayer under the D = 0 (open-circuit) boundary condition. (d) Averaged electric potential of bulk under the E = 0 (closed-circuit) boundary condition.

Since the ground state of bulk $CuInP_2Se_6$ is FE while that of the monolayer is AFE, an obvious question is to find the critical thickness for this FE/AFE transition. Answering this question leads us to a subtle while crucial problem: The above first-principles calculations of bulk and slab structures are actually performed under different boundary conditions, which are, unfortunately, an essential factor to decide the polarization ordering and depolarization effect. In slab structures, as shown in Figure 4.1(c), the existence of a vacuum between layers makes it possible to keep the periodic boundary condition by applying a dipole correction only in the vacuum

region [148]. This mimics the freestanding case (the open-circuit boundary condition). However, to keep the periodic boundary condition of bulk structures [Figure 4.1(d)], the overall electric field of bulk must be zero ($E$ = 0) and *ab initio* packages always automatically apply a compensating field to cancel the spontaneous polarization field. In other words, this mimics the closed-circuit boundary condition [52]. In this sense, our above calculated total energies of bulk and monolayer are under different boundary conditions and the claim for their ground states is problematic. Especially, a brute-force first-principles calculation cannot mimic the open-circuit ($D$ = 0) boundary condition for bulk FE structures because of they are periodic without vacuum.

## 4.4 Electrostatic-Energy Model

To solve this problem and compare the total energy within the same boundary condition, we introduce an electrostatic energy model to investigate ground states and ferroelectricity under electric field [51]. This model will also pave the way for following MC simulations and studies of hysteresis. Based on the geometry and energy track from the *ab initio* climbing image nudged elastic band (cNEB) method [140], [141], we define the displacement of copper atoms from the central position as a polar internal degree of freedom $u$, which is the displacement of copper atoms. The free energy per f.u. can be expressed as

$$\begin{aligned} F(u,E) &= au^2 + bu^4 + cu^6 + E_{es} \\ &= au^2 + bu^4 + cu^6 - \left(P_s(u)E + \frac{1}{2}(\epsilon(u) - 1)\epsilon_0 E^2\right)\Omega \end{aligned} \tag{4.1}$$

The first three terms in Eq. (4.1) form a double-well potential that represents the lattice self-energy described by the Landau theory up to the sixth order. It is called the landau energy part. The rest part ($E_{es}$) of the free energy represents the electrostatic energy under $E$ field, which is defined as $E_{es}$. $\Omega$ is the volume of an f.u. and $\epsilon$ is the electric permittivity.

In solids, the total polarization can be written as

$$P = -\frac{\partial F(u,E)}{\Omega \partial E} = P_s(u) + (\epsilon(u) - 1)\epsilon_0 E \tag{4.2}$$

, where $P_s(u)$ is spontaneous polarization under $E = 0$, merely depending on the displacement $u$ of copper atoms in our studied $CuInP_2Se_6$ structure. The second term is the electronic correspondence to the electric field $E$, in which $\epsilon(u)$ is the ion clamped relative permittivity, which can be calculated by first-principles simulations. Therefore, combining with the general relationship, $D = \epsilon_0 E + P$, we can realize different electric boundary conditions by this electrostatic-energy model.

The parameters in Eq. (4.1) can be obtained for bulk and slab structures, respectively. For the bulk structure, the relative permittivity can be directly calculated by DFT based on the random-phase approximation (RPA) [149], [150]. Moreover, because of the periodic boundary condition, the overall electric field $E$ must be zero. As a result, the electrostatic energy part of Eq. (4.1) disappears and we only need to handle the Landau energy. These parameters can be obtained by fitting the first-principles calculated free energy according to the displacement of copper atoms. The fitted parameters of bulk $CuInP_2Se_6$ are concluded in Table 4.1.

Table 4.1 Fitted parameters of the Landau energy in Eq. (4.1)

| Layer | $a$ (meV/$A^2$) | $b$ (meV/$A^4$) | $c$ (meV/$A^6$) |
|---|---|---|---|
| 1 | −131.10 | 16.97 | 26.16 |
| Bulk | −168.13 | 33.31 | -13.2 |

For slab structures including monolayer and few layers, the fitting process is slightly more complicated. First, we must find the relative permittivity. Using the relation between electric displacement and polarization,

$$P = \frac{[\epsilon(u) - 1]D + P_s}{\epsilon(u)} \tag{4.3}$$

we can tune the applied electric displacement field in first-principles simulations to get the polarization and corresponding electric permittivity. Given that dielectric function is a linear-response property, we confine our calculation within a weak-field limit, such as around 0.1 V/nm. Within this range of applied field, the first-principles calculation shows that the position of copper atoms is nearly fixed. This substantially simplifies the calculation.

Therefore, we can fix the copper atom displacement *u* and tune the applied field *D*. With the calculated polarization *P* from first-principles Berry-phase calculations, the relative permittivity can be fitted by using Eq. (4.3). For example, that of monolayer $CuInP_2Se_6$ is about 2.58 for the FE phase. Interestingly, we observe a substantial change of the relative permittivity according to the thickness of FE structures, which can be seen from the concluded Table 4.2. Finally, with these parameters of the Landau-energy part. Those fitted parameters of the Landau-energy of the monolayer are summarized in Table 4.1 as well.

Table 4.2 $E_{EF} - E_{AFE}$ (meV/f.u.) for monolayer and bulk $CuInP_2Se_6$ under $D = 0$ and $E = 0$.

| Layer | $D = 0$ | $E = 0$ |
|---|---|---|
| 1 | 12.1 | -0.03 |
| Bulk | -0.8 | -13.2 |

## 4.5 Layer-dependent Properties under Different Boundary Conditions

### 4.5.1 Defining Thickness from Monolayer to Bulk

For suspended layered structure, the thickness is defined by the range of x-y plane average potential variation along z direction in a lattice slab. For periodic bulk system, this thickness simply equals lattice constant per unit along z direction. However, for thin slab structure, finding thickness is not as simple as it appears, since first-principle calculation only gives total dipole moment and charge density disperses beyond the atomic boundaries. To solve this problem, we directly obtain polarization from potential plot slope then calculate the thickness.

In Figure 4.2, we plot Hartree potential along z-direction of 1-4 layer at $D = 0$. For a better comparison, lines are adjusted to share a same starting point. Clearly, potential at slab boundaries disperses into vacuum while inner part still holds a periodic pattern between each layer. Potential difference per layer distance can therefore be read straightforwardly, and for 2 ~ 4 layers they are about the same value= 0.365 V/nm. However, in monolayer slab, which is lack of repetitive units, this method is not applicable. We might be able to assert it shares the same value with 2 ~ 4 layers according to the similarity in potential shape. Still, we need further evidence for this deduction.

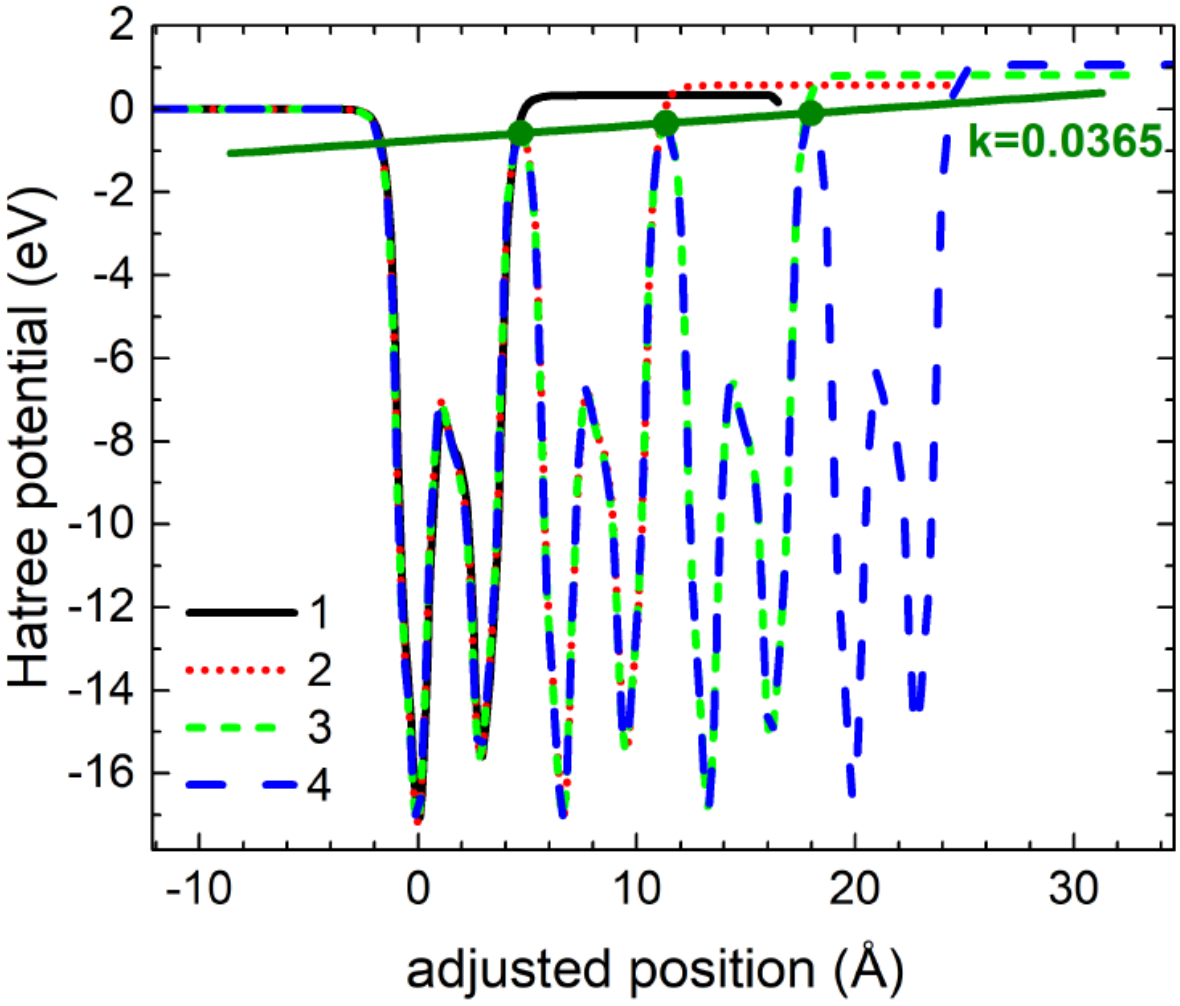


Figure 4.2 1-4 layer Hatree potential along z-direction at $D = 0$.

We plot Hatree potential for monolayer slab under different external field and then subtract potential variation caused by external field, seen in Figure 4.3(a)(b). From Figure 4.3(b) we can clearly see the region of potential variation. We manually cut the rest by hand and obtain a thickness of 9.00 Å. With the dipole moment from first-principle calculation, potential variation per thickness is 0.364 V/nm, just about the same value. This not only gives us a method to determine the polarization for slab structure but provide straightforward verification for electronic dispersion at boundaries as well. Based on that, we can further explain the evolution of layer-dependent polarization under $D = 0$ and $E = 0$ separately.

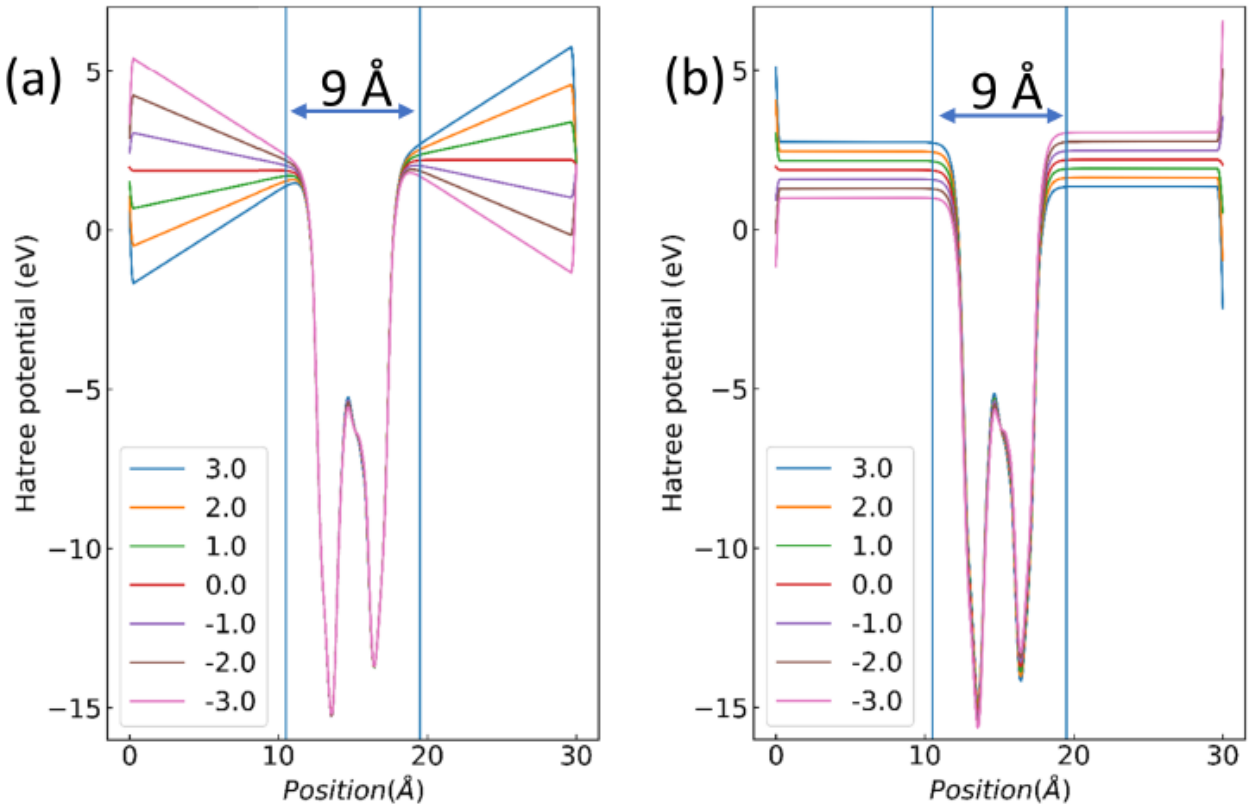


Figure 4.3 (a) hatree potential under external field (V/nm). (b) Same potential subtracted external electric field.

### 4.5.2 Critical Thickness of the AFE/FE Transition

With fitted parameters in Eq. (4.1), we ultimately obtain the FE energy of bulk $CuInP_2Se_6$ under the open-circuit boundary condition ($D = 0$). Interestingly, the FE state is still the ground state, but its energy is only about 0.8 meV below the AFE state, as shown in Table 4.2. More interestingly, under the other boundary condition, i.e., the closed-circuit case ($E = 0$), the above electrostatic model predicts that the energy of the FE state is always lower than that of the AFE state, indicating that monolayer $CuInP_2Se_6$ can be FE when it is short-circuit. This is because, under the closed-circuit boundary condition, a compensating electric field always tends to further lower the energy of the FE state, while the AFE configuration holds $D = E = 0$ intrinsically. In this sense, it is necessary to specify the boundary condition when deciding the ground state of vertically polarized 2D structures.

Combining the energy calculated by the electrostatic model of bulk with the first-principles results of mono-/few-layer $CuInP_2Se_6$, we finally obtain the layer-dependent evolution of stability of $CuInP_2Se_6$ under the open-circuit (freestanding) boundary condition in Figure 4.4. Here, we fit the energy relationship with the thickness and find that there is an AFE/FE transition of the ground state for the freestanding six-layer (~4 nm) $CuInP_2Se_6$. Therefore, for free-standing $CuInP_2Se_6$, under perfect equilibrium, ultrathin structures shall be AFE.

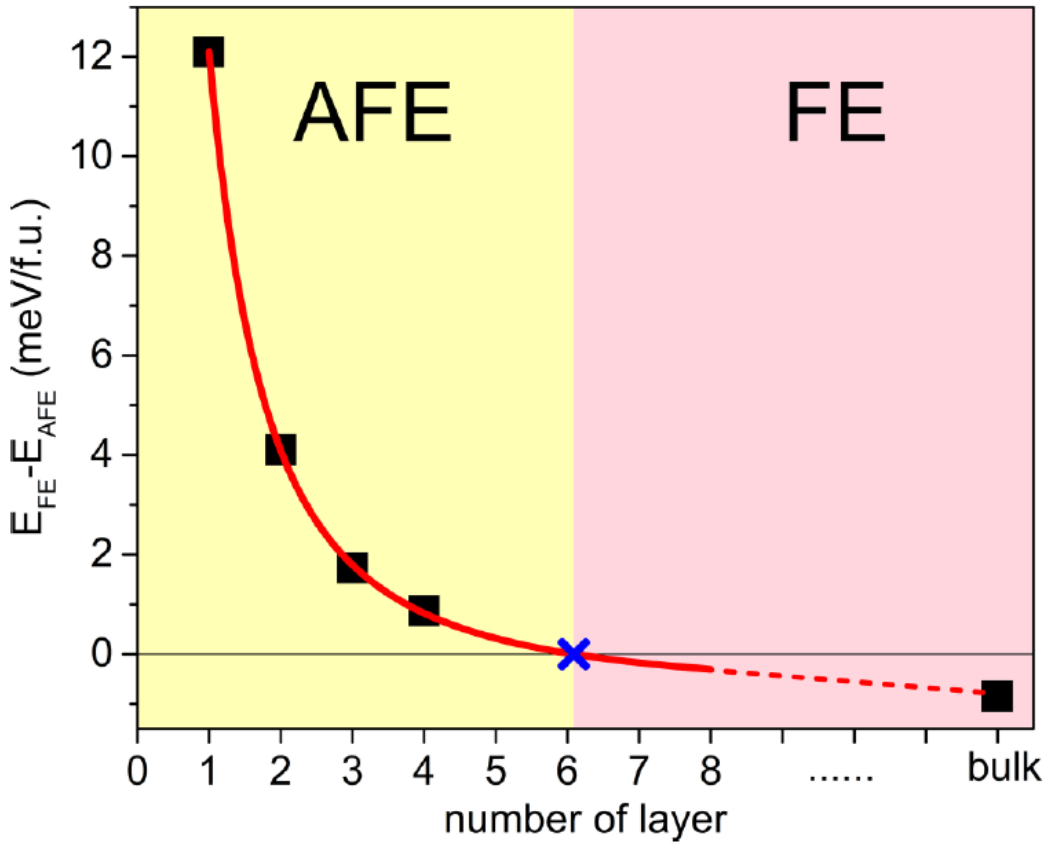


Figure 4.4 Layer-dependent evolution of the energy difference ($E_{FE} - E_{AFE}$) of $CuInP_2Se_6$ under the $D = 0$ boundary condition. The critical thickness is marked by the cross sign.

Finally, with this electrostatic model, we can also calculate the evolution of polarization intensity of $CuInP_2Se_6$ according to the thickness, under different electric boundary conditions, as listed in Table 4.3. Importantly, we can see that the boundary condition plays a significant role in

deciding the magnitude of spontaneous polarization. As previously mentioned, open circuit ($D$ = 0) represents a lack of external field for slab structures. Thus, deviation of centers of ions and electronic charge tend to move with same amplitude as $P/\epsilon_0$ but along opposite directions. This leads to a negative feedback corresponding to a smaller polarization, i.e., the depolarization effect. Interestingly, for our studied vdW layered $CuInP_2Se_6$, its depolarization effect is not sensitive to the thickness, which is evidenced by the nearly fixed polarization shown in Table 4.3. This is in rather contrast to the widely accepted wisdom learned from non-vdW FE materials, in which the depolarization effect is enhanced in thin films. On the other hand, under the closed-circuit ($E$ = 0) boundary condition, the depolarized field is compensated by the external field, endowing centers of ions and electronic charge with much more freedom to move away from each other. Therefore, larger polarization is generally observed.

Table 4.3 Layer-dependent thickness, polarization, and relative permittivity (first principle/model) under different boundary conditions.

| Layer | Thickness (Å/f.u.) | Polarization ($\mu C/cm^2$) | | $\epsilon$ | $\epsilon_{model}$ |
|---|---|---|---|---|---|
| | | $D$ = 0 | $E$ = 0 | | |
| 1 | 9.00 | 0.322 | 0.892 | 2.62 | 2.77 |
| 2 | 7.82 | 0.324 | 1.222 | 3.77 | 3.71 |
| 3 | 7.80 | 0.322 | 1.429 | 4.44 | 4.39 |
| 4 | 7.23 | 0.320 | 1.650 | 4.73 | 4.72 |
| Bulk | 6.64 | 0.365 | 2.531 | 6.93 | 6.93 |

### 4.5.3 Layer-dependent Relative Permittivity

Furthermore, we explore layer-dependent relative permittivity. As number of layers increasing to infinity (bulk), relative permittivity gradually increases to a converged bulk value. The reason is that, for few layers system, charge density disperses beyond the atomic boundaries, as shown in

Figure 4.5(a) with transparent yellow eclipse, contributes a lot to the effective thickness, which is defined as electric potential variation distance. Meanwhile for periodic bulk system, this contribution decreases to 0. A toy model is implemented to explain this phenomenon, as Figure 4.5(b) shows.

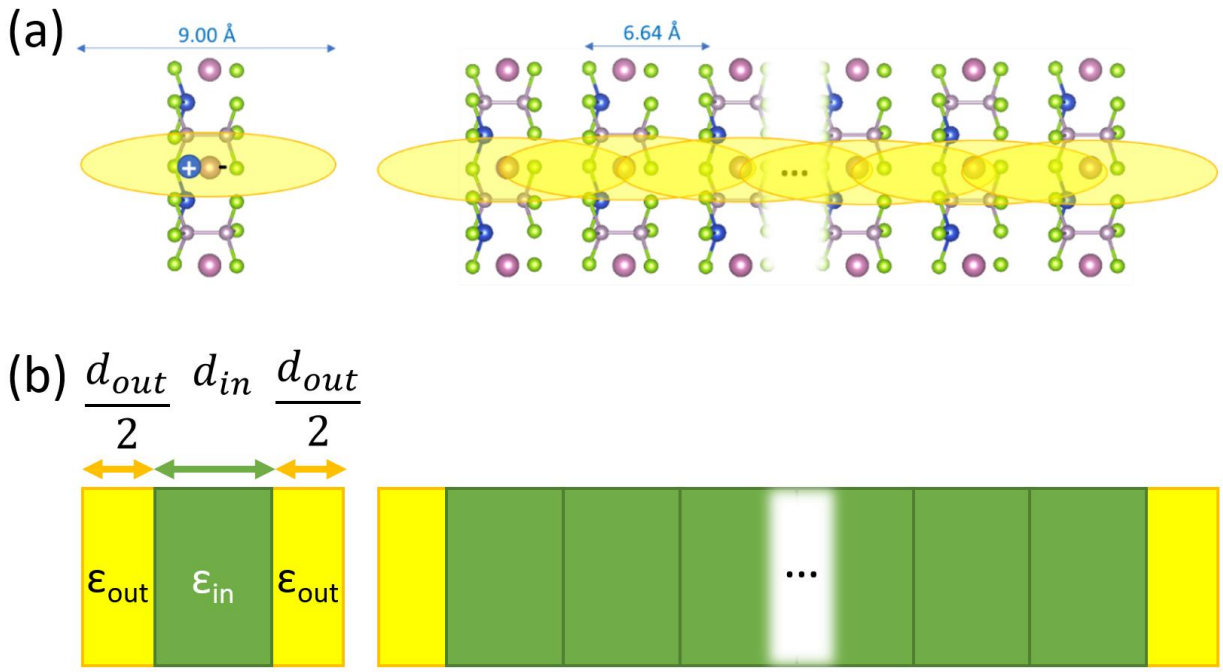


Figure 4.5 (a) Charge dispersion over atoms boundaries in monolayer to bulk $CuInP_2Se_6$. (b) Schematics of model for calculating effective relative permittivity.

The green rectangle represents a single repetitive unit with thickness $d_{in}$ and relative permittivity $\epsilon_{in}$, corresponding to bulk layer distance 6.64 Å and bulk relative permittivity 6.93, while the yellow rectangle represents the dispersed charge with thickness $d_{out}$ and relative permittivity $\epsilon_{out}$. The total effective relative permittivity $\epsilon_{model}$ is calculated by formula

$$\epsilon_{model} = \frac{nd_{in} + d_{out}}{nd_{in}/\epsilon_{in} + d_{out}/\epsilon_{out}} \tag{4.4}$$

, where $n$ is the number of layers. Using monolayer effective thickness 9.00 Å and first-principles calculated epsilon 2.77, we can easily obtain $d_{out}$ = 2.36 Å and $\epsilon_{out}$ = 1.03. With these parameters, the model gives relative permittivity $\epsilon_{model}$, as listed in Table 4.3, in good accordance with first-principle values. This model illustrates the mechanism of layer-dependent variation of relative permittivity and is very useful to predict the value of relative permittivity for samples of different layers.

## 4.6 Polarization in Freestanding $CuInP_2Se_6$

In the following, we particularly focus on polarization orderings in monolayer $CuInP_2Se_6$ under the open-circuit boundary condition, which is the intrinsic case of freestanding samples. Importantly, despite the AFE ground state, the FE state can be a robustly metastable state in realistic monolayer $CuInP_2Se_6$. As shown in Figure 4.6(a), our first-principles cNEB simulation shows that the energy barriers from the FE states to the AFE state are significant, e.g., ~80 meV for monolayer and ~120 meV for bulk. On the other hand, the energy difference between the AFE and FE state is much smaller (~10 meV). In other words, both FE and AFE states could coexist due to this large energy barrier. It agrees with the experimental fact that, despite the FE ordering is the ground state, bulk $CuInP_2Se_6$ exhibits dipole-glass properties at low temperature, because of a mixture of FE and AFE orderings [145]–[147]. In other words, if a strong initialing field is applied to forcing an FE ordering, the vertically ferroelectricity may be stable and observed in monolayer $CuInP_2Se_6$ because of the significant energy barrier between the FE and AFE states. This gives hope to practically monolayer FE structures.

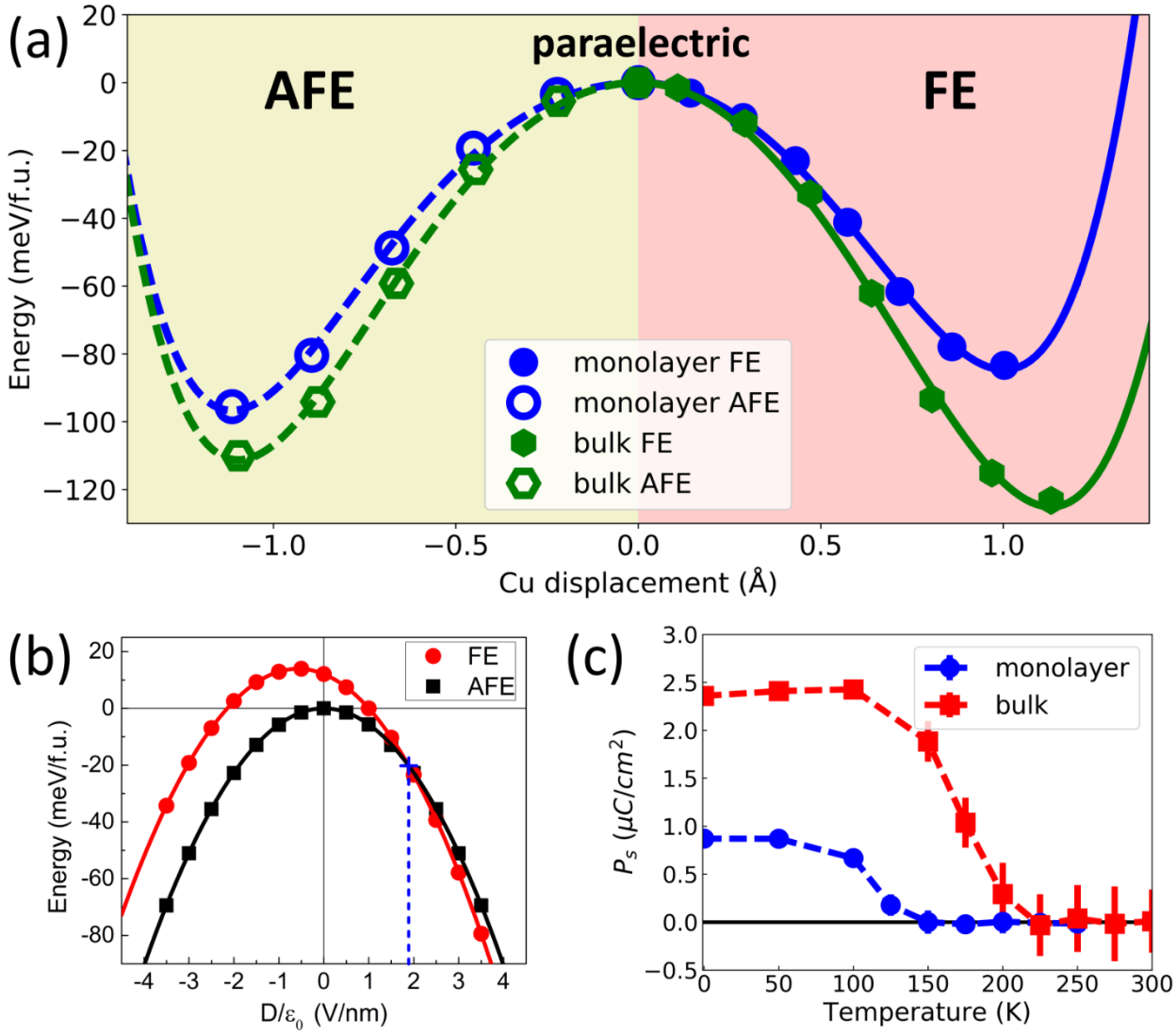


Figure 4.6 (a) Monolayer and bulk sample FE(AFE)-to-paraelectric energy tracks from first-principles NEB calculations. (b) Energy variation with aspect to the applied displacement field $D/\epsilon_0$. The energy of the FE state of the freestanding monolayer is set to be zero. (c) Temperature-dependent zero-$E$-field spontaneous polarization $P_s$in monolayer and bulk $CuInP_2Se_6$.

Our results may be useful for understanding recent measurements of few-layer MCDs. For example, recent experiments have reached controversial conclusions of the existence of the FE state in few-layer $CuInP_2S_6$ (CIPS) [59]–[61], a material very similar to our studied $CuInP_2Se_6$: Ferroelectricity was reported in bilayer CIPS [59] but other measurements [60], [61] showed an opposite conclusion. We have calculated spontaneous polarization of mono-/few-layer CIPS.

Nearly the same energetic pictures have been obtained. Therefore, on one hand, with a strong initial field, the FE state can be formed and observed due to the larger energy barrier between the AFE and FE states. On the other hand, if without a strong enough initial field, a likely coexistence of AFE and FE domains may lead to a dipole glass state and, thus, eliminate the macroscopic polarization.

Furthermore, first-principles simulations can provide the energetic stability of different orderings under the applied external field, as shown in Figure 4.6(b). The energy vs electric field is perfectly fitted by a quadratic function, confirming our electrostatic-energy model in Eq. (4.1). As expected, when an external field is applied to the slab along the direction of spontaneous polarization, FE energy will decrease with a higher rate than AFE. If comparing with the same external field, when $D/\epsilon_0$ exceeds 1.9 V/nm marked by a blue cross in Figure 4.6(b), FE energy will be lower than that of AFE. This corresponds to a critical situation that the ground state transforms from the AFE state to the FE state at 0 K under full equilibrium.

## 4.7 Polarization under Finite Temperature

In addition to spontaneous polarization, ferroelectricity requires the polarization can be switched by practical external field. In this sense, the coercive field is crucial for deciding the feasibility of our predicted ferroelectricity. At very low temperature, because of the large energy barrier shown in Figure 4.6(a), the coercive field to switch these spontaneous polarizations in $CuInP_2Se_6$ could be very large. For example, for bulk one, our calculation shows that its coercive field is about 14V/nm, which is too large compared with experimental value of 77 kV/cm [143]. On the other hand, previous first-principles calculations revealed the similar size of energy barriers in many other known ferroelectric materials [51], [151], whose practically coercive fields are, however, much smaller in reality.

There are several reasons, such as ferroelectric domains [152], [153], that can contribute to this lower coercive field for sizable energy barriers. Here we focus on the temperature effect. In a realistic condition, finite temperature can substantially reduce the coercive field. To include the temperature effect and further show the important hysteresis, the MC method is thus applied. Particularly, because of small interactions between two adjacent units in both FE and AFE states, which can be seen from the small energy difference between AFE/FE states [Figure 4.6(a)], our MC simulation within a single or double unit cell can reflect the properties of the FE and FE orderings, respectively. The MC simulated results are presented in Figure 4.6(c). Based on the effective Hamiltonian [Eq. (4.1)] with fitted parameters of bulk $CuInP_2Se_6$, MC gives a transition temperature around 225 K, which agrees well with experimental values 220 ~ 240 K of bulk $CuInP_2Se_6$ [154], [155]. Using the fitted parameter of monolayer $CuInP_2Se_6$, we estimate the Curie temperature to be around 150 K for the monolayer. This smaller $T_c$ is mainly from the smaller energy barrier of the monolayer, as shown in Figure 4.6(a).

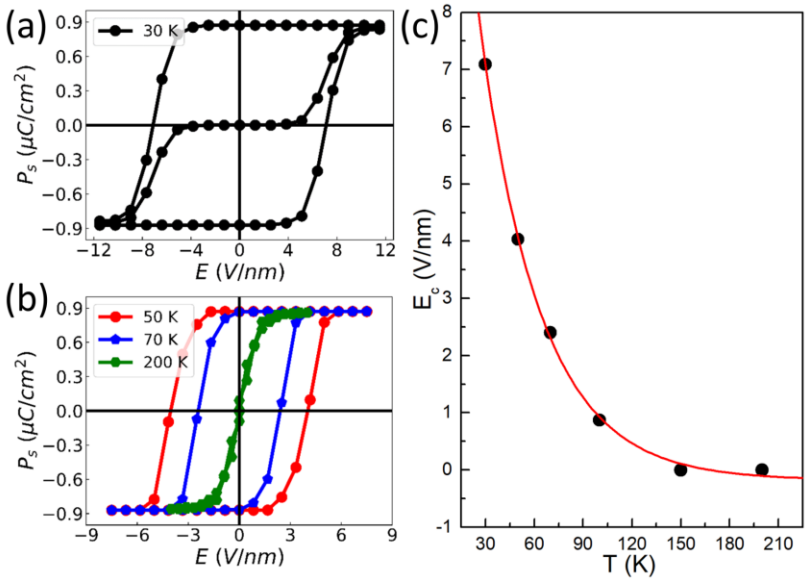


Figure 4.7 (a) Electric hysteresis of polarization of monolayer $CuInP_2Se_6$ under 30 K, starting from the AFE ground state, then evolving into and stabilizing at the FE state. (b) Electric hysteresis of FE $CuInP_2Se_6$ $P_s$ under different temperatures. (c) Temperature-dependent coercive field with an exponential decay fitting.

Finally, using this MC approach, we can simulate the electric hysteresis of monolayer $CuInP_2Se_6$. Because the initial AFE state has opposite polarizations between neighbored units, an average of two unit cells of the MC process with a different starting position can simulate the AFE to FE transition under finite temperature. Figure 4.7(a) shows that, with the added electric field [applying our electrostatic-energy model in Eq. (4.1)] at 30 K, the AFE ground state will gradually evolve into a commensurate state, since electric field will mandatorily tilt the double-well potential. In fact, this field that forces the AFE-to-FE phase transition has been observed in bulk $Pb(Zr,Sn,Ti)O_3$ experimentally [144] and provides a useful way to obtain the FE state from the AFE ground state. In Figure 4.7(b), we present how the hysteresis evolves with the temperature. At 30 K, the coercive field is 7.1 V/nm; at 100 K the value decreases to 0.9 V/nm; finally, at 200 K, hysteresis degrades into a single-value curve because the ferro-to-para phase has occurred at the Curie temperature of 150 K. In other words, as temperature increases, the coercive field will reduce rapidly until it reaches the transition temperatures [156], [157]. We have concluded the relation between the coercive field and the temperature in Figure 4.7(c), which is roughly fitted by an exponential curve. We can see that, if the temperature is above 100 K, this spontaneous FE ordering can be switchable under the practical field (less than 1 V/nm), making it promising to realize and use ferroelectricity in monolayer $CuInP_2Se_6$.

## 4.8 Summary

In conclusion, we have clarified two important boundary conditions that are essential for deciding energy and polarization orderings in bulk and slab structures. With first-principles simulations and the electrostatic-energy model, we predict robust off-plane polarization orderings in ultrathin films of a promising family of materials, MCDs. Taking $CuInP_2Se_6$ as an example, under the (freestanding) open-circuit boundary condition, the ground state of bulk is FE

while that of the monolayer is switched to be AFE, and the critical thickness for the AFE/FE transition is predicted to be six layers; however, under the closed-circuit boundary condition, the ground state of both bulk and monolayer is always FE. Moreover, even for freestanding mono-/few-layer $CuInP_2Se_6$, because of the small energy difference and large barrier between AFE and FE states, the FE state can be practically stabilized and useful for devices. Finally, using MC, we explore the Curie temperature and electric hysteresis, indicating that the corresponding coercive field is well within the practical range at finite temperature. Our studies are useful for understanding recent controversial measurements and further shedding light on ferro-/antiferro-electricity in ultrathin vdW materials.

# Chapter 5: Nonlinear Optical Properties of Organic-Inorganic Hybrid Halide Perovskites

## 5.1 Introduction

Nonlinear optical (NLO) materials play a critical role in modern electronics and photonics by providing means to alter the phase, frequency or amplitude of input electromagnetic waves. Such alternation can be realized through a variety of nonlinear processes such as the linear electro-optic (LEO) effect, second/third/fourth/high harmonic generation (SHG/THG/FHG/HHG), and the Kerr effect, etc. [62] The group of traditional NLO materials are ternary inorganic oxides and their derivatives such as lithium niobate and lithium tantalate. They have achieved widespread success due to their reliable performance, low optical loss, and good stability. However, the synthesis of these insoluble oxides requires high temperature treatment, which hinders broader applications for flexible substrates and integration into chip-scale nanophotonic devices. In contrast to their inorganic counterparts, organic NLO materials based on chromophores have been considered a promising alternative due to their solution processability, faster response and stronger NLO activities. Unfortunately, the low intrinsic stability and high optical loss severely limit their applications.

Nowadays, organic-inorganic hybrid halide perovskites (OHPs) have attracted tremendous interest in emerging photovoltaic (PV) technologies. Extensive theoretical exploration has been applied to studying their linear optical responses related to PV, including self-consistent density functional theory (DFT) approaches as well as quasiparticle methods [158]–[160]. On the other hand, due to the asymmetry of $CH_3NH_3$ units, ferroelectricity can be realized in this family of

materials naturally or by artificially tuning [68]–[70], [161]. This broken inversion symmetry also ensures NLO properties [71], especially second harmonic generation (SHG) and linear electro-optic (LEO) effects [72]–[74] while there has very limited attention on NLO properties in OHPs. Moreover, given the fact that such compounds can be easily fabricated from liquid phase [64], [65] and nearly unlimited choices of compositions [66], [67], OHPs may exhibit unique advantages in fabricating cost and optimizations of NLO properties, compared to traditional NLO materials.

Calculating and predicting NLO properties of OHPs are challenging for the available first-principles simulation tools [78], [162]–[164]. Compared to those of linear optical responses, NLO calculations involve higher-order transitions, which are intrinsically much more expensive in simulation cost. Hence, calculating NLO properties requires a dense k-point sampling and a large number of empty conduction bands to get converged results. As a result, most NLO studies focus on materials either with a small number of atoms per unit cell and high symmetries or low dimensions, which can reduce the number of k-point samples and empty bands. Unfortunately, OHPs contains a larger number of atoms and owns relatively low symmetries. Studying their NLO properties needs fundamental coding developments for better parallelization performance and simulation efficiency.

In this work, we have developed a high-efficient, parallel code (NLOPACK) to study the NLO properties of materials. Using Fortran with the Message Passing Interface (MPI) and performs parallel computation on k-points, the excellent parallelization performance can be hold for up to a few thousand processors. This development enables us to calculate large-scale systems with low symmetries. Our first-principles calculations systematically investigate an important family of cubic phase OHPs, i.e., $CH_3NH_3MX_3$ (M=Ge, Sn, Pb; X= I, Br, Cl). Spin-orbital coupling and

hybrid functional theory are used to improve the calculated band gaps. SHG and LEO effect are observed in all our studied structures, and they are strongly influenced by the cations/anions and corresponding band gaps. Particularly, the cubic phase of $CH_3NH_3SnI_3$ exhibit significant SHG and LEO effect, which are comparable with traditional NLO materials. Our work further reveals the mechanism behind the formation of such large LEO coefficients and their relationship with electronic structures in OHPs.

## 5.2 Computational Methods

In this work, we focus on the widely studied and observed cubic phase of $CH_3NH_3MX_3$ (M=Ge, Sn, Pb; X= I, Br, Cl) [165], [166], which are usually stable at room temperature, making them of application interests. The atomic structure is illustrated in Figure 5.1(a). In the cubic unit cell, the metal M atom sits on each vertex and the halide X atom sits on the middle position of each edge, forming $MX_6$ octahedra cages around the centered organic unit $CH_3NH_3$, conforming to the widely known perovskite structure.

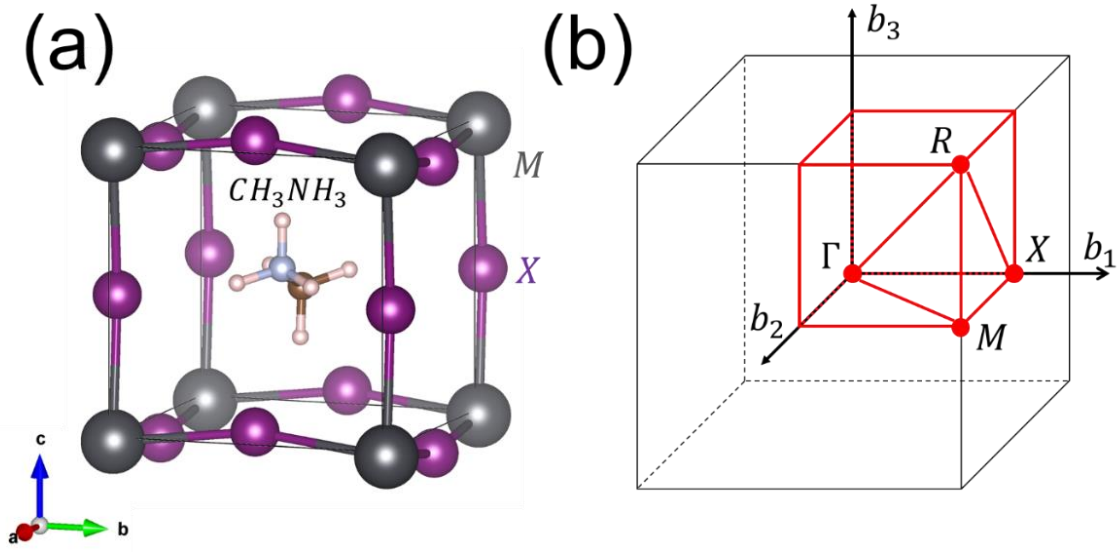


Figure 5.1. (a) Atomic structure of cubic phase $CH_3NH_3MX_3$ (M=Ge, Sn, Pb; X= I, Br, Cl). (b) the corresponding first Brillouin Zone and high-symmetry points.

After relaxation, our density functional theory (DFT)-calculated structures show good agreements with previous works [159], [165], [167], [168]. For example, our calculated lattice parameter of $CH_3NH_3PbI_3$ structure is $a = 6.31$ Å$, b = 6.23$ Å$, c = 6.38$ Å$, \alpha = 90.0°, \beta = 89.2°, \gamma = 90.0°$, which is close to previously published experimental result [168], $a = 6.33$ Å$, \alpha = \beta = \gamma = 90°$. Our calculated slight distortion of the cubic structure is due to that the $CH_3NH_3$ molecule cation ends up along the [101] direction, inducing a deformation and reducing the symmetry of the inorganic $PbI_6$ octahedra.

### 5.2.1 Band Structure Calculation.

The present first-principles calculations are based on density functional theory (DFT) with the generalized gradient approximation using the Perdew-Burke-Ernzerhof (GGA-PBE) functional [92], implemented in the Vienna ab initio simulation package (VASP) [137], [138]. The calculated band structures are along high symmetry lines as shown in Figure 5.1(b). Spin-orbital coupling (SOC) effects are included. The VdW interaction is included through the DFT-D3 method with Becke-Jonson damping [169], [170]. The energy cutoff is 450 eV for structure relaxation and solving the Kohn-Sham equation. We use a 4 × 4 × 4 k-grid sampling in the reciprocal space. Heyd-Scuseria-Ernzerhof (HSE) hybrid functionals HSE06 [171], [172] with $\alpha = 0.45$ (the fraction of exact exchange) are implemented to correct the underestimated band gap calculated by GGA-PBE.

### 5.2.2 Calculation of Optical Properties.

The linear optical dielectric function and the NLO susceptibility are calculated by our developed package NLOPACK based on the basis of the linear response formalism with the independent-particle approximation (IPA) [107]–[110]. The formulas are adapted from reference [107] with

slight modifications [80]. It is known that DFT always underestimates band gaps, we employ the HSE hybrid functional and the scissor approximations correct DFT band gaps [76], [78], [80], [107]. Excitonic effects are not included in this work because excitonic effects are usually significant in reduced-dimensional structures or large-gap insulators.

## 5.3 NLOPACK Performance

### 5.3.1 Parallelism and Scalability

The NLOPACK package can accept the outputs from VASP, which include the momentum matrix elements, Kohn-Sham eigenvalues and occupation numbers. Then it separates these data by k-points and implement parallel reading and computing by each node based on Fortran MPI. Linear and second-order nonlinear properties are calculated using Eq. (2.39)~(2.43), on each group of separated data parallelly. Finally, all results are reduced to root and final results, such as SHG and LEO, are output. In parallel computation, scalability is a vital criterion to evaluate the performance. It is, by definition, a measure of a parallel system's capacity to increase speedup in proportion to the number of processors [173]. According to Eq. (2.39)~(2.43), for each k-point the calculations are independent, indicating parallelism based on k-points should be able to achieve perfect scalability. An example of SHG calculation running time on GaAs illustrates the scalability of our package. As shown in Figure 5.2(a), for NLOPACK package, total time equals the split time, which is the time for splitting the input data into groups of k-points, adding the run time, which is the pure calculation time on each separated group of k-points. The run time vs number of nodes is linear in the $\log_2$ scale, indicating that the calculation process is sped up in proportion to the number of nodes with perfect scalability. Even the split time will increase with number of nodes, the total time will still decrease and gradually converge to a certain value

where all k-points are distributed one-by-one to the same number of node. In summary, our implementation of parallelism in NLOPACK is efficient and in good scalability.

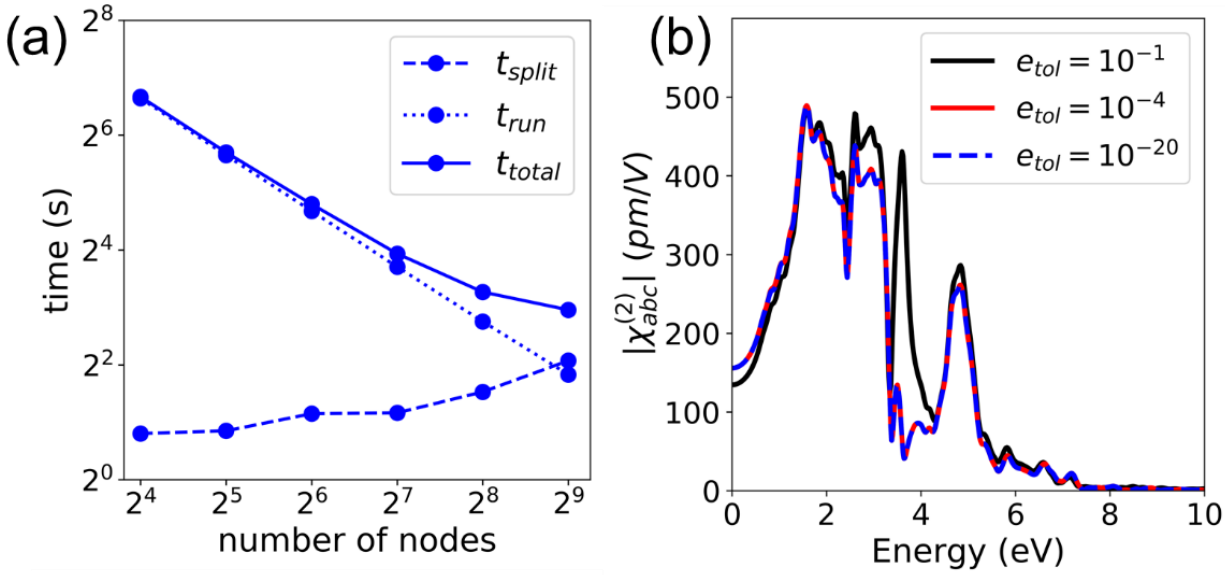


Figure 5.2. (a) Running time (in $\log_2$ scale) of SHG calculation using NLOPACK under different number of nodes, in which $t_{total} = t_{run} + t_{split}$. The benchmark calculations are cubic GaAs with 40 total bands under a $8 \times 8 \times 8 = 512$ non-reduced k-point sampling. (b) Calculated SHG susceptibility with different energy tolerance for GaAs.

### 5.3.2 Singularity Problem

We should note that there are terms in Eq. (2.39)~(2.43), where the cancellation of energy in the dominator will lead to singularities [107], [110], [174], [175]. The singularities will occur under two conditions: one is the resonance term that $\omega_{ij} \approx \omega$ or $2\omega$, and it can be avoided by adding a small positive real damping factor $\eta$ to $\omega \leftarrow \omega + i\eta$. Herein $\eta$ is directly related to the bandwidth of the Lorentzian resonance peaks. In our calculations for perovskite, we choose $\eta = 0.035\ eV$; the other is that $\omega_{ln} - \omega_{ml} \approx 0$ at some special k-points. According to [174]–[176], such k-points are few and the contributions are safe to discard. In our calculation, we set the energy tolerance $e_{tol}$, determining which term to discard if the denominator of that term is less than this

value. For a larger $e_{tol}$, more terms with singularities tend to be discarded and for a small $e_{tol}$, more singularities tend to be reserved. From the Figure 5.2(b) we can clearly see that, while $e_{tol} = 10^{-1}$ discard too much terms for an accurate result, plot for GaAs at $e_{tol} = 10^{-4}$ with less singularities and $e_{tol} = 10^{-20}$ with more singularities agrees well, indicating that $e_{tol} = 10^{-4}$ is a good choice for the convergence of susceptibility plot and the rest of singularity terms either vanish or cancel with each other ideally in GaAs, thus making no difference to the summation. Nevertheless, in practice, when the denominator goes really small, even tiny numerical difference will lead to huge difference in real values and the supposed cancellation will be broken, which is quite common in NLO calculation of OHPs. As a result, it is fairly important to choose a proper $e_{tol}$ to avoid unreasonable large peaks of singularities. For our NLO calculation of OHPs, we choose $e_{tol} = 10^{-8}$.

## 5.4 Results and discussion

### 5.4.1 Band Structures of $CH_3NH_3MX_3$

Because all the $CH_3NH_3MX_3$ have the same crystalline structure and are isoelectronic, their electronic band structures are rather similar. We plot those of two representatives, i.e., $CH_3NH_3PbI_3$ and $CH_3NH_3SnI_3$ in Figure 5.3. The band gaps have been corrected by the scissor approximation based on HSE hybrid functional theory calculations. All the $CH_3NH_3MX_3$ OHPs exhibit direct gap at the *R* point, which is the corner of the Cubic first Brillouin zone as shown in Figure 5.1(b). This agrees well with previous works [167].

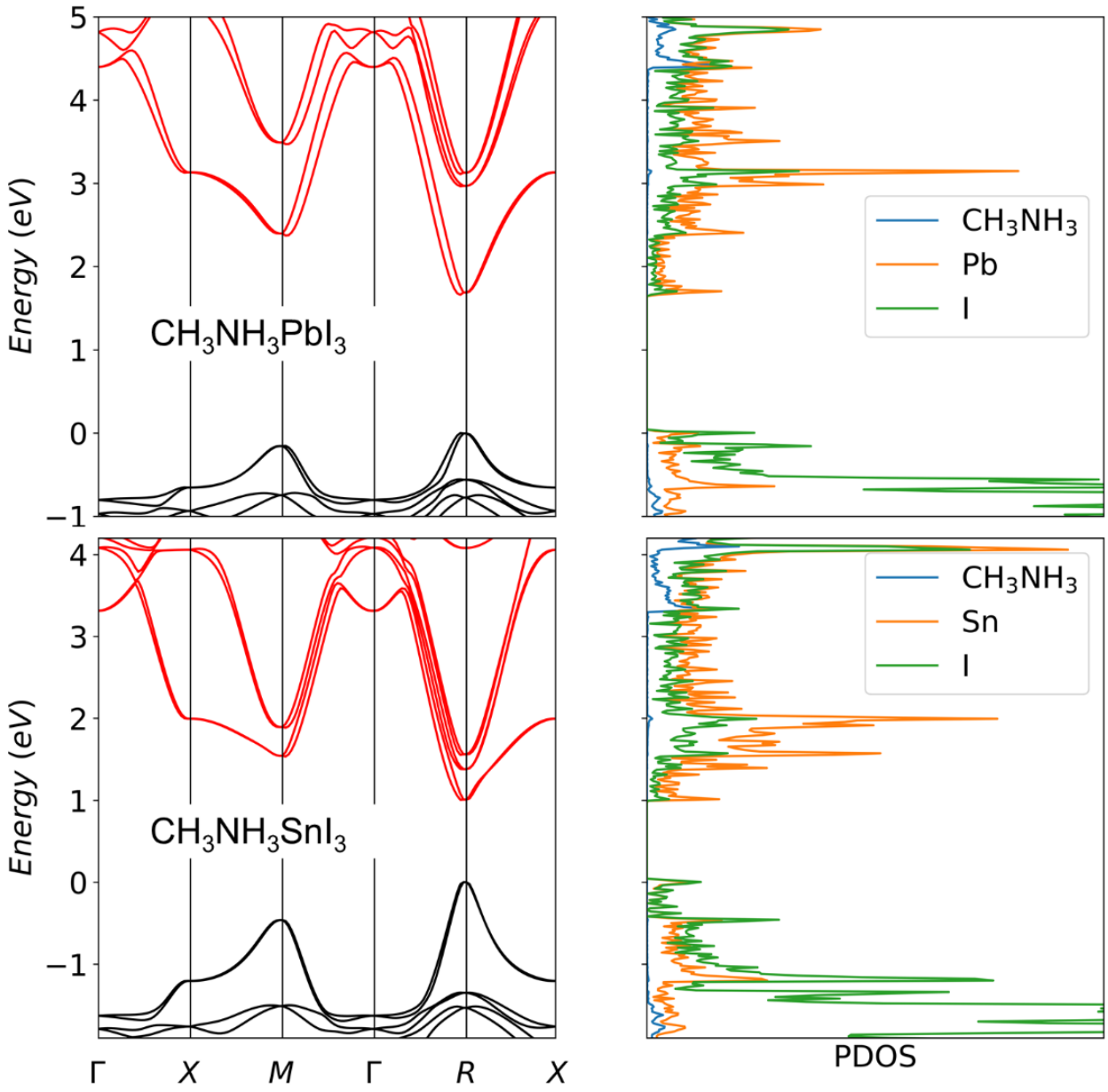


Figure 5.3. Band structures (left panels) and projected density of states (PDOS) (right panels) of $CH_3NH_3PbI_3$ and $CH_3NH_3SnI_3$. Both materials have direct band gap at the R symmetry point. The top valence band is set to be 0 eV.

The band structures around band edges are mostly determined by the inorganic components of the hybrid perovskite [167][177]. The PDOS in Figure 5.3 shows that the bottom of the conduction band mainly originates from group-V M atom, while the top of the valence band is derived from halide atom X as well as M atom. There is almost no hybridization of the band-edge states with organic components because PDOS of $CH_3NH_3$ are very far away from band

gap. Therefore, the organic molecules affect mainly the crystal structure and break the inversion symmetry by the orientation of C-N bond, rather than directly influence the band structure. Still, this structural effect only leads to tiny change of band structures and will not affect the overall optical properties [167].

Table 5.1. HSE band gap for cubic $CH_3NH_3MX_3$ perovskites

| Bandgap (eV) | I | Br | Cl |
|---|---|---|---|
| Pb | 1.64 | 2.24 | 2.85 |
| Sn | 1.01 | 1.48 | 2.1 |
| Ge | 1.66 | 2.63 | 3.46 |

Table 5.1 summarizes evolution of the band gaps of our studied OHP structures. The calculated band gaps agree well with measurements. For example, the calculated band gap of $CH_3NH_3PbI_3$ is 1.64 eV which is in a good agreement with experimental value 1.61 eV [178]. Table I also reveals that there is a monotonic correlation between the band gap and halide X atoms: the band gap increases from I to Br to Cl. Finally, Table 5.1 suggests that the magnitudes of the band gaps cover a large scale of light spectrum from infrared to the blue end of the visible frequency. Therefore, these OHPs can be promising for applications of electronic, optical, and electro-optical devices.

### 5.4.2 Second Harmonic Generation (SHG)

Most of symmetries of the cubic $CH_3NH_3MX_3$ perovskites are broken. As a result, all elements of the SHG tensor are expected to be nonzero. To address the essential results, we focus on several typical components. In Figure 5.4(a), the calculated absolute values, which is the modulus of real and imaginary parts of SHG susceptibility $\chi^{(2)}_{111}$, $\chi^{(2)}_{122}$ and $\chi^{(2)}_{311}$ of four OHPs, i.e., $CH_3NH_3PbI_3$, $CH_3NH_3PbBr_3$, $CH_3NH_3SnI_3$ and $CH_3NH_3SnBr_3$, are presented. The subscripts 1, 2, 3 of the susceptibility denote the Cartesian coordinates *x*, *y*, and *z*. Figure 5.4(a) indicates that all these OHPS exhibit SHG mainly within the infrared frequency range. In particular, the SHG susceptibility of $CH_3NH_3SnI_3$ is significant, and its intensity is comparable to those of widely used SHG materials such as GaAs [77], and emerging two-dimensional transition-metal dichalcogenides [78], indicating NLO application potential of OHPs.

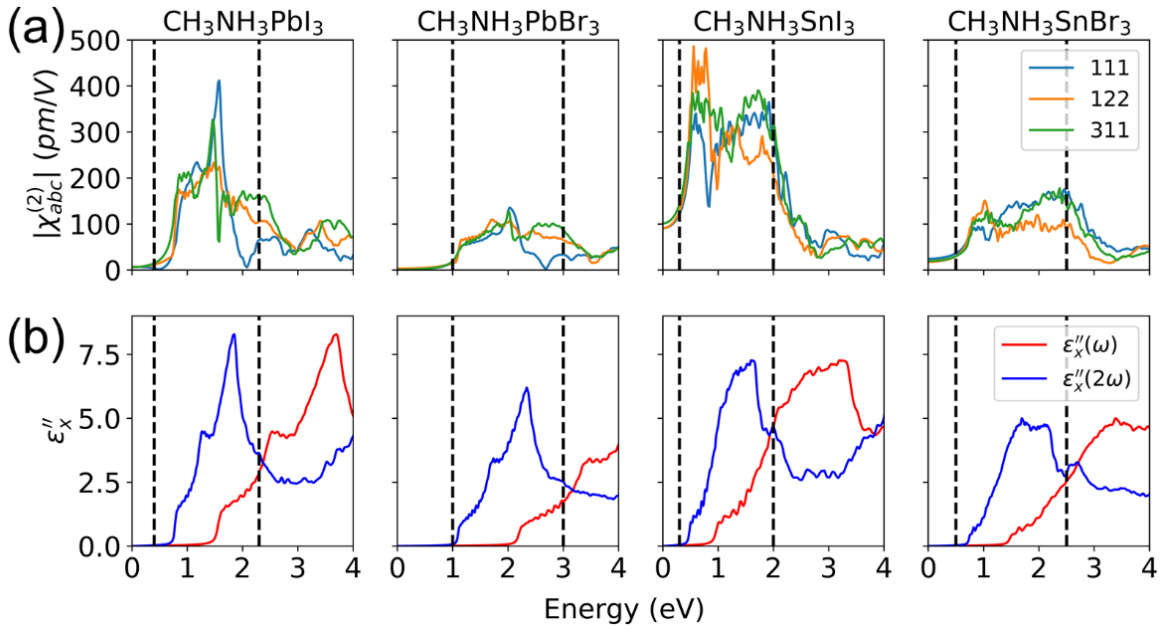


Figure 5.4. (a) 111, 122, 311 components of absolute SHG susceptibility of cubic $CH_3NH_3PbI_3$, $CH_3NH_3PbBr_3$, $CH_3NH_3SnI_3$, $CH_3NH_3SnBr_3$ perovskites, and (b) the correspondent imaginary part of dielectric function, $\varepsilon''_x(\omega)$, and the double-resonant one, $\varepsilon''_x(2\omega)$.

To analyze spectra of these SHG susceptibilities, it is helpful to compare them with the absorptive part of the corresponding dielectric function. In Figure 5.4(b), the x-direction component $\varepsilon_x''(\omega)$ is plotted in a red-color curve. Comparing the linear and SHG spectra, two different features can be observed. First, because of the second-order nature of SHG, the low-energy edge of SHG spectra is about half of that of the linear absorption spectra. Second, the positions of peaks are very different between SHG and linear optical absorption spectra. This is expected because of the different transition paths in these two processes. Third, the SHG spectra in higher energy regime are much weaker compared to those of linear-optical spectra. This is because the SHG amplitude is inversely proportional to the square of transition energy while that of linear optical absorption is inversely proportional to the transition energy, according to Eq. (2.39)~(2.43).

On the other hand, Figure 5.4 shows there are strong correlation between SHG and linear optical absorption. Following an approach of previous work [78], we replot the linear optical absorption, which relates to the single-photon resonance process in SHG, with double frequency, $\varepsilon_x''(2\omega)$, in Figure 5.4(b) (blue-color curves). This is approximately to only consider two-phonon process with identical energy, which reflects the double-photon resonance. Interestingly, these approximated double-resonance spectra fit those of SHG very well. As shown in Figure 5.4, within the two vertical dashed lines, the peak positions and edges approximately agree with each other. Therefore, the main features (peaks) of SHG spectra, especially below band gap ($E_g$), are from the double-resonance processes.

In Figure 5.4(a), with the same M atom, the absolute value of SHG susceptibility $|\chi_{abc}^{(2)}|$ will decrease from I to Br as the X atom. Such a trend can also be seen in the absorptive part of the

corresponding dielectric function $\varepsilon_x''(\omega)$ in Figure 5.4(b). The reason is that, when the radius of X atom decreases, the band gap of $CH_3NH_3MX_3$ increases, as shown in Table 5.1. Meanwhile, the SHG amplitude is inversely correlated to transition energy. As a result, $CH_3NH_3SnI_3$ with the smallest band gap has the largest SHG susceptibility. The susceptibility $|\chi^{(2)}_{122}|$ reaches about 500 pm/V at around 0.6 eV, and the susceptibilities along other directions, such as $|\chi^{(2)}_{311}|, |\chi^{(2)}_{111}|$, also have broad peaks above 300 pm/V.

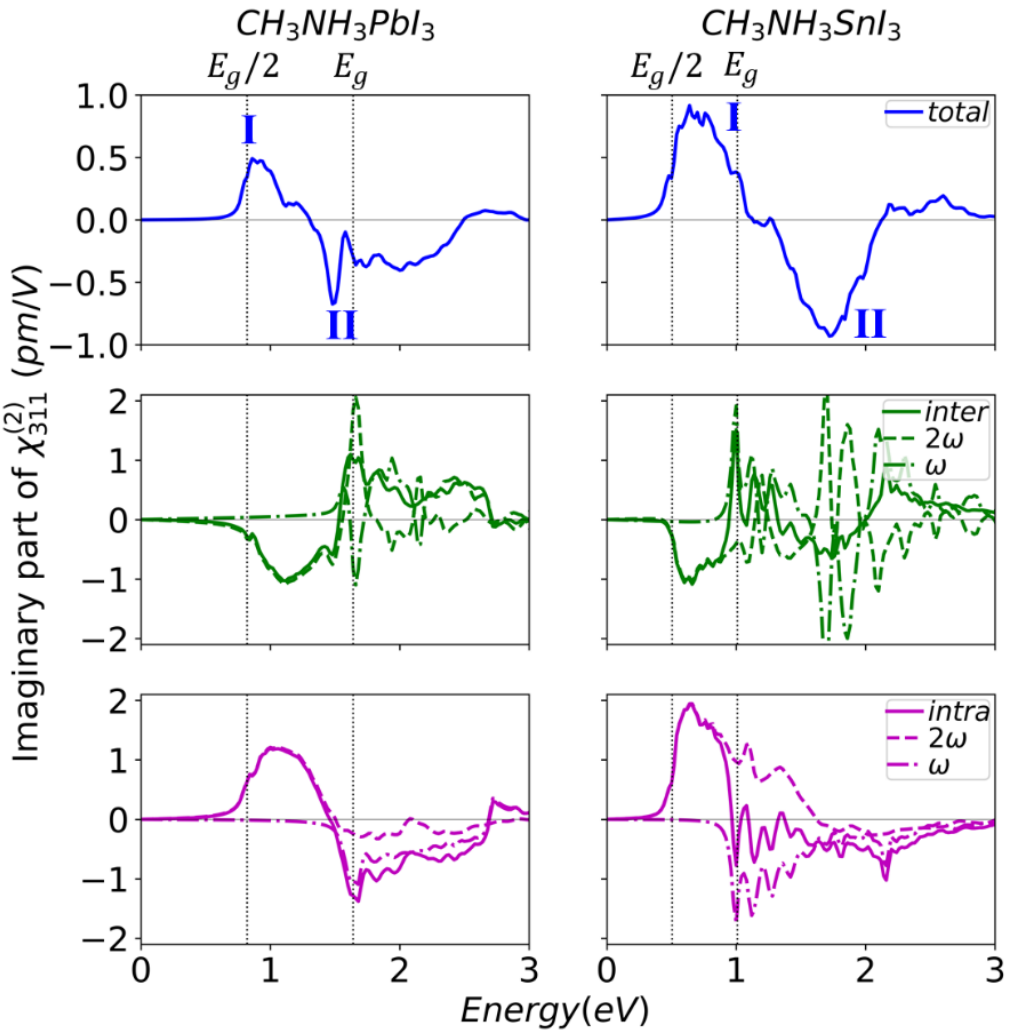


Figure 5.5. Imaginary part of SHG susceptibility and contributions of subdivided interband (inter)and intraband (intra) terms of $CH_3NH_3PbI_3$ and $CH_3NH_3SnI_3$, half band gap $E_g/2$ and band gap $E_g$ are marked with vertical black lines.

In addition to the above qualitative discussion of the band-gap effect on SHG, we further quantitatively analyze the large SHG susceptibility in $CH_3NH_3SnI_3$. In Figure 5.5, the imaginary parts of SHG susceptibility are plotted in upper panels with blue colors. Meanwhile, the interband contributions to the imaginary part of SHG, mainly including the double resonance $2\omega$ (dash line) and single resonance $\omega$ (dash-dot line) components, [107]–[109] are plotted in middle panels. Those intraband transitions are plotted in the lower panels. The modulation part is much smaller, and we did not list it here.

In Figure 5.5, there are two significant wave packages with opposite sign wrapping resonance terms that mainly comes from interband and intraband terms, starting at $\frac{E_g}{2}$. In both $CH_3NH_3PbI_3$ and $CH_3NH_3SnI_3$, the intraband double resonance term makes the largest contributions, and the net contribution leads to a positive peak packet, marked as I, roughly within the region of $\frac{E_g}{2} \sim E_g$. Above the band gap, single resonances appear and start to mix up with double-resonance parts. The large negative contribution of intraband $\omega$ part still gives rise to a negative peak package above $E_g$, marked as II. Due to the contributions of interband $2\omega$ item below $E_g$ are of the same scale, and the contributions of intraband $2\omega$ item below $E_g$ of $CH_3NH_3SnI_3$ are larger than those of $CH_3NH_3PbI_3$, peak I of $CH_3NH_3SnI_3$ are larger than that of $CH_3NH_3PbI_3$. Moreover, in the energy region just above $E_g$, interband and intraband contributions of $CH_3NH_3PbI_3$ cancel with each other to large extent while those of $CH_3NH_3SnI_3$ aggregates in both negative amplitudes. As a result, for both I and II regions, the SHG susceptibility of $CH_3NH_3SnI_3$ is larger than that $CH_3NH_3PbI_3$.

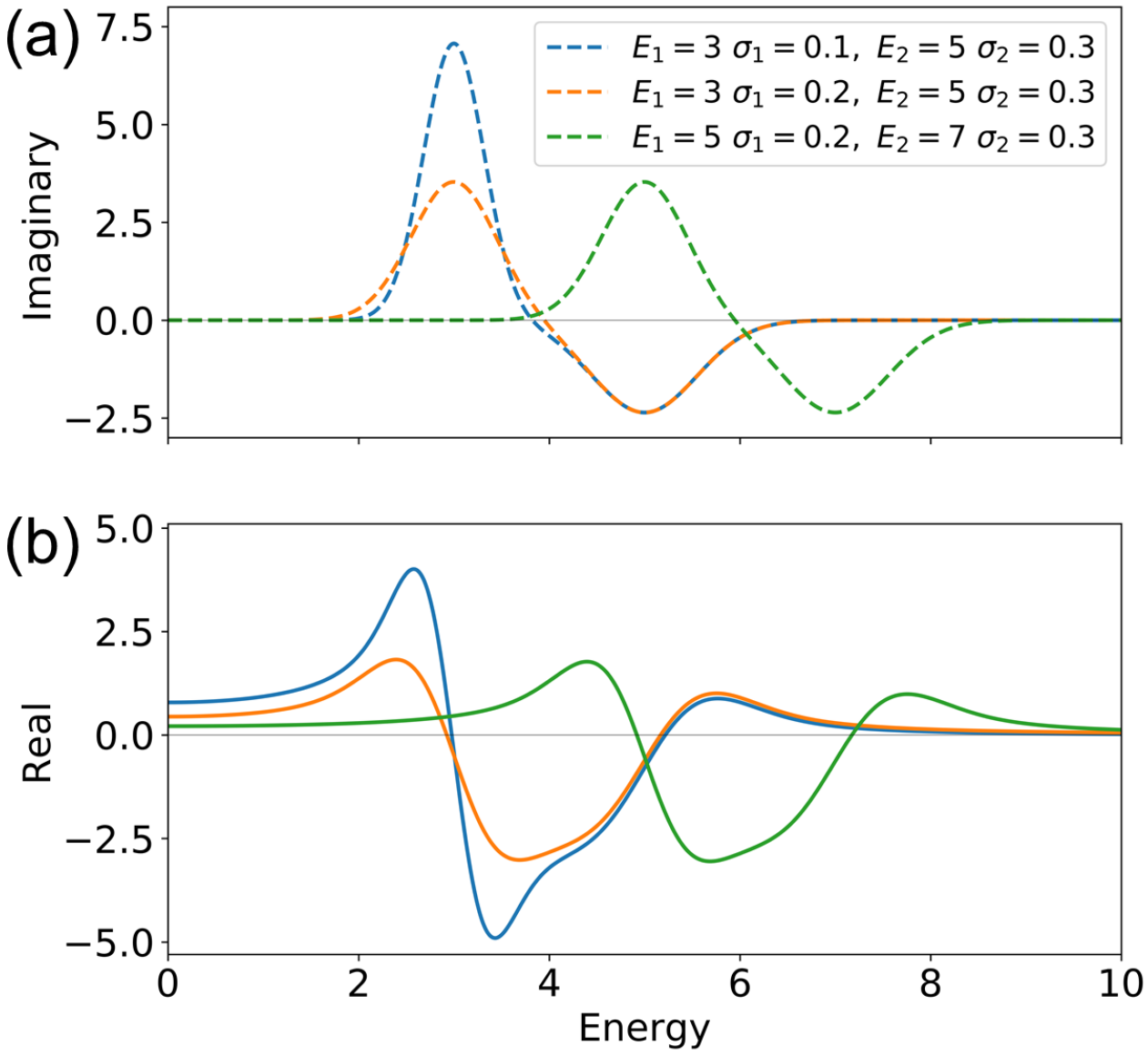


Figure 5.6. (a) Pairs of positive/negative Gaussian peaks as imaginary part, shown in dash line and (b) real part, shown in solid line, obtained by Kramers-Kronig relation of SHG susceptibility

### 5.4.3 Linear Electro-Optical (LEO) Effect

Figure 5.4 and Table 5.2 also indicate that low-frequency LEO coefficients are also large for in a few OHPs. Specially, for $\chi^{(2)}_{311}$ of $CH_3NH_3SnI_3$ there is a large intercept value 103.4 pm/V at zero frequency compared to others, which is greatly beneficial for LEO coefficient. Using the Eq.

(2.44), for $CH_3NH_3SnI_3$ LEO coefficient $r_{311}$ is found to be 3.9 pm/V, as shown in Table 5.2, which is comparable to GaAs [179] and CdTe [180]. All these large values suggest that the cubic $CH_3NH_3MX_3$ perovskites may have application potentials in second-order NLO devices and LEO modulators.

Table 5.2 Calculated dielectric function ($\varepsilon_x(0), \varepsilon_z(0)$), SHG susceptibility $|\chi^{(2)}_{311}|$, and LEO coefficient $r_{311}$ of the $CH_3NH_3MX_3$.

| M | Pb | | | Sn | | | Ge | | |
|---|---|---|---|---|---|---|---|---|---|
| X | I | Br | Cl | I | Br | Cl | I | Br | Cl |
| $\varepsilon_x(0)$ | 5.9 | 5.2 | 4.0 | 7.2 | 5.2 | 4.4 | 5.9 | 4.1 | 3.7 |
| $\varepsilon_z(0)$ | 5.6 | 4.2 | 3.7 | 7.4 | 5.1 | 4.2 | 6.4 | 4.1 | 3.7 |
| $\lvert\chi^{(2)}_{311}(0)\rvert\ (pm/V)$ | 6.4 | 0.7 | 1.9 | 103.4 | 19.7 | 0.9 | 14.4 | 2.8 | 2.7 |
| $r_{311}(0)\ (pm/V)$ | 0.4 | 0.1 | 0.3 | 3.9 | 1.5 | 0.1 | 0.8 | 0.3 | 0.4 |

To further illustrate the effects of SHG part on zero-frequency intercept value, which is directly related to the LEO coefficients, we construct a schematic picture in Figure 5.6 consisted of pairs of positive/negative Gaussian peaks with peak values ($E_1, E_2$) and linewidth ($\sigma_1^2, \sigma_2^2$) to mimic the I and II peaks of the imaginary SHG susceptibility in Figure 5.5. Then we can intercept values of the real part from the imaginary part through the Kramers-Kronig relation [78], [107], [109]. Comparing results in Figure 5.6 with different linewidth and peak positions, we can find that, using the same linewidth $\sigma$, if the two imaginary-part peaks move away from the zero frequency, which means a larger band gap, the corresponding real-part intercept will decrease.

Furthermore, as shown by the blue and orange-color curves, larger positive peak I and smaller negative peak II will lead to a larger real part intercept value, and vice versa. This explains the zero-frequency intercept results in Figure 5.4. The energies of the I and II peaks of $CH_3NH_3SnI_3$ are lower due to its smaller band gap. Meanwhile, for $CH_3NH_3PbI_3$, the negative peak II is stronger and broader than the positive peak I and for $CH_3NH_3SnI_3$, peak I and II are about the same scale. Combining these two factors, SHG susceptibility zero-frequency intercept, as well as LEO coefficient for $CH_3NH_3SnI_3$ should be much larger than those of $CH_3NH_3PbI_3$.

## 5.5 Summary

In summary, we investigate the structural and electronic properties of organic-inorganic hybrid halide perovskites $CH_3NH_3MX_3$ (M=Ge, Sn, Pb; X=halide). Linear and second-order NLO properties, such as SHG and LEO effects, are explored by our NLOPACK package, which proves good parallelism and scalability on such large systems. Due to the lack of inversion symmetry, cubic-phase hybrid halide perovskites exhibit SHG responses. We find large SHG susceptibilities as well as large LEO coefficients for $CH_3NH_3SnI_3$, which have application potentials in second-order NLO devices and LEO modulators. We further reveal that the large zero-frequency intercept of SHG susceptibilities are due to small band gap as well as large intraband double resonance contributions. This work will stimulate further experimental and theoretical investigations to achieve NLO responses in organic-inorganic hybrid halide perovskites, which can be fabricated by low-cost solution-based approaches.

# References


[1] C. Liu, F. Li, L.-P. Ma, and H.-M. Cheng, "Advanced materials for energy storage," *Adv. Mater.*, vol. 22, no. 8, pp. E28--E62, 2010.

[2] J.-Y. Lee, J. An, and C. K. Chua, "Fundamentals and applications of 3D printing for novel materials," *Appl. Mater. Today*, vol. 7, pp. 120–133, 2017.

[3] R. Langer and D. A. Tirrell, "Designing materials for biology and medicine," *Nature*, vol. 428, no. 6982, p. 487, 2004.

[4] M. Brust, D. J. Schiffrin, D. Bethell, and C. J. Kiely, "Novel gold-dithiol nano-networks with non-metallic electronic properties," *Adv. Mater.*, vol. 7, no. 9, pp. 795–797, 1995.

[5] W. Eerenstein, N. D. Mathur, and J. F. Scott, "Multiferroic and magnetoelectric materials," *Nature*, vol. 442, no. 7104, p. 759, 2006.

[6] K. S. Novoselov *et al.*, "Electric field effect in atomically thin carbon films," *Science (80-. ).*, vol. 306, no. 5696, pp. 666–669, 2004.

[7] C. Jin, F. Lin, K. Suenaga, and S. Iijima, "Fabrication of a freestanding boron nitride single layer and its defect assignments," *Phys. Rev. Lett.*, vol. 102, no. 19, p. 195505, 2009.

[8] K. S. Novoselov *et al.*, "Two-dimensional atomic crystals," *Proc. Natl. Acad. Sci.*, vol. 102, no. 30, pp. 10451–10453, 2005.

[9] L. Li *et al.*, "Black phosphorus field-effect transistors," *Nat. Nanotechnol.*, vol. 9, no. 5, p. 372, 2014.

[10] X. Xu, W. Yao, D. Xiao, and T. F. Heinz, "Spin and pseudospins in layered transition metal dichalcogenides," *Nat. Phys.*, vol. 10, no. 5, p. 343, 2014.

[11] Q. H. Wang, K. Kalantar-Zadeh, A. Kis, J. N. Coleman, and M. S. Strano, "Electronics and optoelectronics of two-dimensional transition metal dichalcogenides," *Nat. Nanotechnol.*, vol. 7, no. 11, p. 699, 2012.

[12] K. F. Mak and J. Shan, "Photonics and optoelectronics of 2D semiconductor transition metal dichalcogenides," *Nat. Photonics*, vol. 10, no. 4, p. 216, 2016.

[13] W. Han, R. K. Kawakami, M. Gmitra, and J. Fabian, "Graphene spintronics," *Nat. Nanotechnol.*, vol. 9, no. 10, p. 794, 2014.

[14] K. S. Novoselov *et al.*, "A roadmap for graphene," *Nature*, vol. 490, no. 7419, p. 192, 2012.

[15] J. R. Schaibley *et al.*, "Valleytronics in 2D materials," *Nat. Rev. Mater.*, vol. 1, no. 11, p. 16055, 2016.

[16] K. F. Mak, C. Lee, J. Hone, J. Shan, and T. F. Heinz, "Atomically thin MoS 2: a new

direct-gap semiconductor," *Phys. Rev. Lett.*, vol. 105, no. 13, p. 136805, 2010.

[17] A. Splendiani *et al.*, "Emerging photoluminescence in monolayer MoS2," *Nano Lett.*, vol. 10, no. 4, pp. 1271–1275, 2010.

[18] W. Zhao *et al.*, "Evolution of electronic structure in atomically thin sheets of WS2 and WSe2," *ACS Nano*, vol. 7, no. 1, pp. 791–797, 2012.

[19] S. Larentis, B. Fallahazad, and E. Tutuc, "Field-effect transistors and intrinsic mobility in ultra-thin MoSe2 layers," *Appl. Phys. Lett.*, vol. 101, no. 22, p. 223104, 2012.

[20] J. Frenkel, "On the transformation of light into heat in solids. I," *Phys. Rev.*, vol. 37, no. 1, p. 17, 1931.

[21] H. Haug and S. W. Koch, "Semiconductor laser theory with many-body effects," *Phys. Rev. A*, vol. 39, no. 4, p. 1887, 1989.

[22] Y. Liang, S. Huang, R. Soklaski, and L. Yang, "Quasiparticle band-edge energy and band offsets of monolayer of molybdenum and tungsten chalcogenides," *Appl. Phys. Lett.*, vol. 103, no. 4, p. 42106, 2013.

[23] M. M. Ugeda *et al.*, "Giant bandgap renormalization and excitonic effects in a monolayer transition metal dichalcogenide semiconductor," *Nat. Mater.*, vol. 13, no. 12, p. 1091, 2014.

[24] C. Zhang, H. Wang, W. Chan, C. Manolatou, and F. Rana, "Absorption of light by excitons and trions in monolayers of metal dichalcogenide Mo S 2: Experiments and theory," *Phys. Rev. B*, vol. 89, no. 20, p. 205436, 2014.

[25] Y. Liang and L. Yang, "Carrier plasmon induced nonlinear band gap renormalization in two-dimensional semiconductors," *Phys. Rev. Lett.*, vol. 114, no. 6, p. 63001, 2015.

[26] S. Gao, Y. Liang, C. D. Spataru, and L. Yang, "Dynamical excitonic effects in doped two-dimensional semiconductors," *Nano Lett.*, vol. 16, no. 9, pp. 5568–5573, 2016.

[27] R. S. Jacobsen *et al.*, "Strained silicon as a new electro-optic material," *Nature*, vol. 441, no. 7090, p. 199, 2006.

[28] K. Liu *et al.*, "Elastic properties of chemical-vapor-deposited monolayer MoS2, WS2, and their bilayer heterostructures," *Nano Lett.*, vol. 14, no. 9, pp. 5097–5103, 2014.

[29] S. Bertolazzi, J. Brivio, and A. Kis, "Stretching and breaking of ultrathin MoS2," *ACS Nano*, vol. 5, no. 12, pp. 9703–9709, 2011.

[30] M. R. Falvo *et al.*, "Bending and buckling of carbon nanotubes under large strain," *Nature*, vol. 389, no. 6651, p. 582, 1997.

[31] M. ~V. V Fischetti, Z. Ren, P. ~M. M. Solomon, M. Yang, and K. Rim, "Six-band k· p calculation of the hole mobility in silicon inversion layers: Dependence on surface orientation, strain, and silicon thickness," *J. Appl. Phys.*, vol. 94, no. 2, pp. 1079–1095, 2003.

[32] J. H. Haeni *et al.*, “Room-temperature ferroelectricity in strained SrTiO 3,” *Nature*, vol. 430, no. 7001, p. 758, 2004.

[33] R. Fei and L. Yang, “Strain-engineering the anisotropic electrical conductance of few-layer black phosphorus,” *Nano Lett.*, vol. 14, no. 5, pp. 2884–2889, 2014.

[34] W. S. Yun, S. W. Han, S. C. Hong, I. G. Kim, and J. D. Lee, “Thickness and strain effects on electronic structures of transition metal dichalcogenides: 2H-M X 2 semiconductors (M= Mo, W; X= S, Se, Te),” *Phys. Rev. B*, vol. 85, no. 3, p. 33305, 2012.

[35] L. Yang *et al.*, “Lattice strain effects on the optical properties of MoS 2 nanosheets,” *Sci. Rep.*, vol. 4, p. 5649, 2014.

[36] Z. H. Ni, T. Yu, Y. H. Lu, Y. Y. Wang, Y. P. Feng, and Z. X. Shen, “Uniaxial strain on graphene: Raman spectroscopy study and band-gap opening,” *ACS Nano*, vol. 2, no. 11, pp. 2301–2305, 2008.

[37] G.-H. Lee *et al.*, “Flexible and transparent MoS2 field-effect transistors on hexagonal boron nitride-graphene heterostructures,” *ACS Nano*, vol. 7, no. 9, pp. 7931–7936, 2013.

[38] M. Mehboudi, K. Utt, H. Terrones, E. O. Harriss, A. A. P. SanJuan, and S. Barraza-Lopez, “Strain and the optoelectronic properties of nonplanar phosphorene monolayers,” *Proc. Natl. Acad. Sci.*, vol. 112, no. 19, pp. 5888–5892, 2015.

[39] X. Wei, B. Fragneaud, C. A. Marianetti, and J. W. Kysar, “Nonlinear elastic behavior of graphene: Ab initio calculations to continuum description,” *Phys. Rev. B*, vol. 80, no. 20, p. 205407, 2009.

[40] F. Liu, P. Ming, and J. Li, “Ab initio calculation of ideal strength and phonon instability of graphene under tension,” *Phys. Rev. B*, vol. 76, no. 6, p. 64120, 2007.

[41] P. Johari and V. B. Shenoy, “Tuning the electronic properties of semiconducting transition metal dichalcogenides by applying mechanical strains,” *ACS Nano*, vol. 6, no. 6, pp. 5449–5456, 2012.

[42] J. F. Scott, *Ferroelectric memories*, vol. 3. Springer Science & Business Media, 2013.

[43] R. D. King-Smith and D. Vanderbilt, “First-principles investigation of ferroelectricity in perovskite compounds,” *Phys. Rev. B*, vol. 49, no. 9, p. 5828, 1994.

[44] W. J. Merz, “Switching time in ferroelectric BaTiO3 and its dependence on crystal thickness,” *J. Appl. Phys.*, vol. 27, no. 8, pp. 938–943, 1956.

[45] R. E. Cohen, “Origin of ferroelectricity in perovskite oxides,” *Nature*, vol. 358, no. 6382, pp. 136–138, 1992.

[46] J. B. Neaton, C. Ederer, U. V Waghmare, N. A. Spaldin, and K. M. Rabe, “First-principles study of spontaneous polarization in multiferroic Bi Fe O 3,” *Phys. Rev. B*, vol. 71, no. 1, p. 14113, 2005.

[47] S. Liu, I. Grinberg, and A. M. Rappe, “Intrinsic ferroelectric switching from first

principles," *Nature*, vol. 534, no. 7607, pp. 360–363, 2016.

[48] N. A. Benedek and C. J. Fennie, "Why are there so few perovskite ferroelectrics?," *J. Phys. Chem. C*, vol. 117, no. 26, pp. 13339–13349, 2013.

[49] L. Chen *et al.*, "Large Elasto-Optic Effect in Epitaxial PbTiO 3 Films," *Phys. Rev. Lett.*, vol. 115, no. 26, p. 267602, 2015.

[50] H. J. Xiang, "Origin of polar distortion in LiNbO 3-type 'ferroelectric' metals: role of A-site instability and short-range interactions," *Phys. Rev. B*, vol. 90, no. 9, p. 94108, 2014.

[51] K. F. Garrity, K. M. Rabe, and D. Vanderbilt, "Hyperferroelectrics: proper ferroelectrics with persistent polarization," *Phys. Rev. Lett.*, vol. 112, no. 12, p. 127601, 2014.

[52] M. Stengel, N. A. Spaldin, and D. Vanderbilt, "Electric displacement as the fundamental variable in electronic-structure calculations," *Nat Phys*, vol. 5, no. 4, pp. 304–308, 2009.

[53] J. Junquera and P. Ghosez, "Critical thickness for ferroelectricity in perovskite ultrathin films," *Nature*, vol. 422, no. 6931, p. 506, 2003.

[54] M. Stengel, D. Vanderbilt, and N. A. Spaldin, "Enhancement of ferroelectricity at metal-oxide interfaces," *Nat Mater*, vol. 8, no. 5, pp. 392–397, 2009.

[55] R. Fei, W. Kang, and L. Yang, "Ferroelectricity and phase transitions in monolayer group-IV monochalcogenides," *Phys. Rev. Lett.*, vol. 117, no. 9, p. 97601, 2016.

[56] P. Z. Hanakata, A. Carvalho, D. K. Campbell, and H. S. Park, "Polarization and valley switching in monolayer group-IV monochalcogenides," *Phys. Rev. B*, vol. 94, no. 3, p. 35304, 2016.

[57] M. Wu and X. C. Zeng, "Intrinsic Ferroelasticity and/or Multiferroicity in Two-Dimensional Phosphorene and Phosphorene Analogues," *Nano Lett.*, vol. 16, no. 5, pp. 3236–3241, 2016.

[58] K. Chang *et al.*, "Discovery of robust in-plane ferroelectricity in atomic-thick SnTe," *Science (80-. ).*, vol. 353, no. 6296, pp. 274–278, 2016.

[59] F. Liu *et al.*, "Room-temperature ferroelectricity in CuInP2S6 ultrathin flakes," *Nat. Commun.*, vol. 7, 2016.

[60] A. Belianinov *et al.*, "CuInP2S6 room temperature layered ferroelectric," *Nano Lett.*, vol. 15, no. 6, pp. 3808–3814, 2015.

[61] M. Chyasnavichyus *et al.*, "Size-effect in layered ferrielectric CuInP2S6," *Appl. Phys. Lett.*, vol. 109, no. 17, p. 172901, 2016.

[62] R. W. Boyd, *Nonlinear optics*. Elsevier, 2003.

[63] J. Luo, S. Huang, Z. Shi, B. M. Polishak, X.-H. Zhou, and A. K. Jen, "Tailored Organic Electro-optic Materials and Their Hybrid Systems for Device Applications †," *Chem. Mater.*, vol. 23, no. 3, pp. 544–553, Feb. 2011.

[64] P. P. Boix, K. Nonomura, N. Mathews, and S. G. Mhaisalkar, “Current progress and future perspectives for organic/inorganic perovskite solar cells,” *Mater. today*, vol. 17, no. 1, pp. 16–23, 2014.

[65] M. A. Loi and J. C. Hummelen, “Hybrid solar cells: perovskites under the sun,” *Nat. Mater.*, vol. 12, no. 12, p. 1087, 2013.

[66] F. Deschler *et al.*, “High photoluminescence efficiency and optically pumped lasing in solution-processed mixed halide perovskite semiconductors,” *J. Phys. Chem. Lett.*, vol. 5, no. 8, pp. 1421–1426, 2014.

[67] E. Mosconi, A. Amat, M. K. Nazeeruddin, M. Grätzel, and F. De Angelis, “First-principles modeling of mixed halide organometal perovskites for photovoltaic applications,” *J. Phys. Chem. C*, vol. 117, no. 27, pp. 13902–13913, 2013.

[68] A. Stroppa, C. Quarti, F. De Angelis, and S. Picozzi, “Ferroelectric polarization of CH3NH3PbI3: a detailed study based on density functional theory and symmetry mode analysis,” *J. Phys. Chem. Lett.*, vol. 6, no. 12, pp. 2223–2231, 2015.

[69] F. Zheng, H. Takenaka, F. Wang, N. Z. Koocher, and A. M. Rappe, “First-Principles Calculation of the Bulk Photovoltaic Effect in CH3NH3PbI3 and CH3NH3PbI3--x Cl x,” *J. Phys. Chem. Lett.*, vol. 6, no. 1, pp. 31–37, 2014.

[70] Y. Kutes, L. Ye, Y. Zhou, S. Pang, B. D. Huey, and N. P. Padture, “Direct observation of ferroelectric domains in solution-processed CH3NH3PbI3 perovskite thin films,” *J. Phys. Chem. Lett.*, vol. 5, no. 19, pp. 3335–3339, 2014.

[71] eg P. A. Franken, A. E. Hill, C. W. el Peters, and G. Weinreich, “Generation of optical harmonics,” *Phys. Rev. Lett.*, vol. 7, no. 4, p. 118, 1961.

[72] G. Walters and E. H. Sargent, “Electro-optic Response in Germanium Halide Perovskites,” *J. Phys. Chem. Lett.*, vol. 9, no. 5, pp. 1018–1027, 2018.

[73] A. A. Popkova *et al.*, “Second Harmonic Generation in CH3NH3PbI3 thin films,” in *Frontiers in Optics*, 2018, p. JW3A--49.

[74] Q. Lin, A. Armin, R. C. R. Nagiri, P. L. Burn, and P. Meredith, “Electro-optics of perovskite solar cells,” *Nat. Photonics*, vol. 9, no. 2, p. 106, 2015.

[75] J.-J. Li, Z.-Y. Li, and D.-Z. Zhang, “Second harmonic generation in one-dimensional nonlinear photonic crystals solved by the transfer matrix method,” *Phys. Rev. E*, vol. 75, no. 5, p. 56606, 2007.

[76] S. Sharma and C. Ambrosch-Draxl, “Second-harmonic optical response from first principles,” *Phys. Scr.*, vol. 2004, no. T109, p. 128, 2004.

[77] S. Bergfeld and W. Daum, “Second-Harmonic Generation in GaAs: Experiment versus Theoretical Predictions of $χ$ x y z (2),” *Phys. Rev. Lett.*, vol. 90, no. 3, p. 36801, 2003.

[78] C.-Y. Wang and G.-Y. Guo, “Nonlinear optical properties of transition-metal

dichalcogenide MX2 (M= Mo, W; X= S, Se) monolayers and trilayers from first-principles calculations," *J. Phys. Chem. C*, vol. 119, no. 23, pp. 13268–13276, 2015.

[79] G. Y. Guo, K. C. Chu, D. Wang, and C. Duan, "Linear and nonlinear optical properties of carbon nanotubes from first-principles calculations," *Phys. Rev. B*, vol. 69, no. 20, p. 205416, 2004.

[80] H. Wang and X. Qian, "Giant optical second harmonic generation in two-dimensional multiferroics," *Nano Lett.*, vol. 17, no. 8, pp. 5027–5034, 2017.

[81] J. Guan, W. Song, L. Yang, and D. Tománek, "Strain-controlled fundamental gap and structure of bulk black phosphorus," *Phys. Rev. B*, vol. 94, p. 45414, 2016.

[82] W. Song and L. Yang, "Quasiparticle band gaps and optical spectra of strained monolayer transition-metal dichalcogenides," *Phys. Rev. B*, vol. 96, no. 23, p. 235441, 2017.

[83] W. Song, R. Fei, and L. Yang, "Off-plane polarization ordering in metal chalcogen diphosphates from bulk to monolayer," *Phys. Rev. B*, vol. 96, no. 23, p. 235420, 2017.

[84] R. M. Martin, *Electronic Structure: Basic Theory and Practical Methods*. Cambridge University Press, 2004.

[85] G. D. Mahan, *Many-Particle Physics*. Springer US, 1990.

[86] R. M. Martin, L. Reining, and D. M. Ceperley, *Interacting electrons*. Cambridge University Press, 2016.

[87] P. Hohenberg and W. Kohn, "Inhomogeneous Electron Gas," *Phys. Rev.*, vol. 136, no. 3B, pp. B864--B871, 1964.

[88] W. Kohn and L. J. Sham, "Self-consistent equations including exchange and correlation effects," *Phys. Rev.*, vol. 140, no. 4A, p. A1133, 1965.

[89] M. S. Hybertsen and S. G. Louie, "Electron correlation in semiconductors and insulators: Band gaps and quasiparticle energies," *Phys. Rev. B*, vol. 34, pp. 5390–5413, 1986.

[90] J. P. Perdew and A. Zunger, "Self-interaction correction to density-functional approximations for many-electron systems," *Phys. Rev. B*, vol. 23, no. 10, p. 5048, 1981.

[91] D. C. Langreth and M. J. Mehl, "Beyond the local-density approximation in calculations of ground-state electronic properties," *Phys. Rev. B*, vol. 28, no. 4, p. 1809, 1983.

[92] J. P. Perdew, K. Burke, and M. Ernzerhof, "Generalized gradient approximation made simple," *Phys. Rev. Lett.*, vol. 77, no. 18, p. 3865, 1996.

[93] J. P. Perdew and Y. Wang, "Accurate and simple analytic representation of the electron-gas correlation energy," *Phys. Rev. B*, vol. 45, no. 23, p. 13244, 1992.

[94] M. van Schilfgaarde, T. Kotani, and S. Faleev, "Quasiparticle Self-Consistent $GW$ Theory," *Phys. Rev. Lett.*, vol. 96, no. 22, p. 226402, 2006.

[95] T. Takagahara and K. Takeda, “Theory of the quantum confinement effect on excitons in quantum dots of indirect-gap materials,” *Phys. Rev. B*, vol. 46, no. 23, p. 15578, 1992.

[96] L. Hedin, “New Method for Calculating the One-Particle Green’s Function with Application to the Electron-Gas Problem,” *Phys. Rev.*, vol. 139, no. 3A, pp. A796--A823, 1965.

[97] M. Rohlfing and S. G. Louie, “Electron-hole excitations and optical spectra from first principles,” *Phys. Rev. B*, vol. 62, pp. 4927–4944, 2000.

[98] G. Onida, L. Reining, and A. Rubio, “Electronic excitations: density-functional versus many-body Green’s-function approaches,” *Rev. Mod. Phys.*, vol. 74, no. 2, pp. 601–659, 2002.

[99] J. Deslippe, G. Samsonidze, D. A. Strubbe, M. Jain, M. L. Cohen, and S. G. Louie, “BerkeleyGW: A massively parallel computer package for the calculation of the quasiparticle and optical properties of materials and nanostructures,” *Comput. Phys. Commun.*, vol. 183, pp. 1269–1289, 2012.

[100] B. H. Bransden, *Quantum mechanics*. Pearson Education India, 2000.

[101] R. Resta and D. Vanderbilt, “Theory of polarization: a modern approach,” in *Physics of Ferroelectrics*, Springer, 2007, pp. 31–68.

[102] M. V. Berry, “Quantal phase factors accompanying adiabatic changes,” *Proc. R. Soc. Lond. A*, vol. 392, no. 1802, pp. 45–57, 1984.

[103] N. A. Spaldin, “A beginner’s guide to the modern theory of polarization,” *J. Solid State Chem.*, vol. 195, pp. 2–10, 2012.

[104] R. Resta, “Macroscopic polarization in crystalline dielectrics: the geometric phase approach,” *Rev. Mod. Phys.*, vol. 66, no. 3, p. 899, 1994.

[105] W. Kohn, “Analytic properties of Bloch waves and Wannier functions,” *Phys. Rev.*, vol. 115, no. 4, p. 809, 1959.

[106] K. N. Kudin, R. Car, and R. Resta, “Berry phase approach to longitudinal dipole moments of infinite chains in electronic-structure methods with local basis sets,” *J. Chem. Phys.*, vol. 126, no. 23, p. 234101, 2007.

[107] J. L. P. Hughes and J. E. Sipe, “Calculation of second-order optical response in semiconductors,” *Phys. Rev. B*, vol. 53, no. 16, p. 10751, 1996.

[108] J. E. Sipe and E. Ghahramani, “Nonlinear optical response of semiconductors in the independent-particle approximation,” *Phys. Rev. B*, vol. 48, no. 16, p. 11705, 1993.

[109] C. Aversa and J. E. Sipe, “Nonlinear optical susceptibilities of semiconductors: Results with a length-gauge analysis,” *Phys. Rev. B*, vol. 52, no. 20, p. 14636, 1995.

[110] J. E. Sipe and A. I. Shkrebtii, “Second-order optical response in semiconductors,” *Phys. Rev. B*, vol. 61, no. 8, p. 5337, 2000.

[111] Z. H. Levine and D. C. Allan, “Linear optical response in silicon and germanium including self-energy effects,” *Phys. Rev. Lett.*, vol. 63, no. 16, p. 1719, 1989.

[112] Z. Liu *et al.*, “Strain and structure heterogeneity in MoS$_{2}$ atomic layers grown by chemical vapour deposition,” *Nat. Commun.*, vol. 5, p. 5246, 2014.

[113] A. Singh *et al.*, “Trion formation dynamics in monolayer transition metal dichalcogenides,” *Phys. Rev. B*, vol. 93, p. 41401, 2016.

[114] T. Jakubczyk *et al.*, “Radiatively Limited Dephasing and Exciton Dynamics in MoSe2Monolayers Revealed with Four-Wave Mixing Microscopy,” *Nano Lett.*, vol. 16, pp. 5333–5339, 2016.

[115] E. Artacho *et al.*, “The SIESTA method; developments and applicability,” *J. Phys. Condens. Matter*, vol. 20, no. 6, p. 64208, 2008.

[116] P. Giannozzi *et al.*, “QUANTUM ESPRESSO: a modular and open-source software project for quantum simulations of materials,” *J. Phys. Condens. Matter*, vol. 21, p. 395502, 2009.

[117] J. Deslippe, G. Samsonidze, M. Jain, M. L. Cohen, and S. G. Louie, “Coulomb-hole summations and energies for G W calculations with limited number of empty orbitals: A modified static remainder approach,” *Phys. Rev. B*, vol. 87, no. 16, p. 165124, 2013.

[118] V. Tran, “Electronic and Optical Properties of Few Layer Black Phosphorus and Black Phosphorus Nanoribbons from First Principles Calculations,” Washington University in St. Louis, 2016.

[119] R. W. Keyes, “The electrical properties of black phosphorus,” *Phys. Rev.*, vol. 92, no. 3, p. 580, 1953.

[120] W. Ju, T. Li, H. Wang, Y. Yong, and J. Sun, “Strain-induced semiconductor to metal transition in few-layer black phosphorus from first principles,” *Chem. Phys. Lett.*, vol. 622, pp. 109–114, 2015.

[121] X. Peng, Q. Wei, and A. Copple, “Strain-engineered direct-indirect band gap transition and its mechanism in two-dimensional phosphorene,” *Phys. Rev. B*, vol. 90, no. 8, p. 85402, 2014.

[122] D. W. Latzke *et al.*, “Electronic structure, spin-orbit coupling, and interlayer interaction in bulk MoS$_{2}$ and WS$_{2}$,” *Phys. Rev. B*, vol. 91, p. 235202, 2015.

[123] B. D. Malone and M. L. Cohen, “Quasiparticle semiconductor band structures including spin-orbit interactions,” *J. Phys. Condens. Matter*, vol. 25, p. 105503, 2013.

[124] A. Ramasubramaniam, “Large excitonic effects in monolayers of molybdenum and tungsten dichalcogenides,” *Phys. Rev. B*, vol. 86, p. 115409, 2012.

[125] D. Y. Qiu, F. H. da Jornada, and S. G. Louie, “Optical Spectrum of MoS$_{2}$: Many-Body Effects and Diversity of Exciton States,” *\prl*, vol. 111, p. 216805, 2013.

[126] N. J. Borys *et al.*, "Anomalous Above-Gap Photoexcitations and Optical Signatures of Localized Charge Puddles in Monolayer Molybdenum Disulfide," *ACS Nano*, vol. 11, no. 2, pp. 2115–2123, 2017.

[127] A. M. Smith, M. C. Mancini, and S. Nie, "Bioimaging: Second window for in vivo imaging," *Nat. Nanotechnol.*, vol. 4, pp. 710–711, 2009.

[128] J. Feng, X. Qian, C.-W. Huang, and J. Li, "Strain-engineered artificial atom as a broad-spectrum solar energy funnel," *Nat. Photonics*, vol. 6, pp. 866–872, 2012.

[129] R. Fei, W. Li, J. Li, and L. Yang, "Giant piezoelectricity of monolayer group IV monochalcogenides: SnSe, SnS, GeSe, and GeS," *Appl. Phys. Lett.*, vol. 107, no. 17, p. 173104, 2015.

[130] L. C. Gomes, A. Carvalho, and A. H. C. Neto, "Enhanced piezoelectricity and modified dielectric screening of two-dimensional group-IV monochalcogenides," *Phys. Rev. B*, vol. 92, no. 21, p. 214103, 2015.

[131] T. Rangel, B. M. Fregoso, B. S. Mendoza, T. Morimoto, J. E. Moore, and J. B. Neaton, "Giant bulk photovoltaic effect and spontaneous polarization of single-layer monochalcogenides," *arXiv Prepr. arXiv1610.06589*, 2016.

[132] R. Haleoot *et al.*, "Photostrictive two-dimensional materials in the monochalcogenide family," *Phys. Rev. Lett.*, vol. 118, no. 22, p. 227401, 2017.

[133] W. Ding *et al.*, "Prediction of intrinsic two-dimensional ferroelectrics in In2Se3 and other III2-VI3 van der Waals materials," *Nat. Commun.*, vol. 8, 2017.

[134] S. N. Shirodkar and U. V Waghmare, "Emergence of Ferroelectricity at a Metal-Semiconductor Transition in a 1 T Monolayer of MoS 2," *Phys. Rev. Lett.*, vol. 112, no. 15, p. 157601, 2014.

[135] A. Chandrasekaran, A. Mishra, and A. K. Singh, "Ferroelectricity, Antiferroelectricity, and Ultrathin 2D Electron/Hole Gas in Multifunctional Monolayer MXene," *Nano Lett.*, vol. 17, no. 5, pp. 3290–3296, 2017.

[136] M. E. J. Newman and G. T. Barkema, *Monte Carlo Methods in Statistical Physics chapter 1-4*. Oxford University Press: New York, USA, 1999.

[137] G. Kresse and J. Furthmüller, "Efficient iterative schemes for ab initio total-energy calculations using a plane-wave basis set," *Phys. Rev. B*, vol. 54, no. 16, p. 11169, 1996.

[138] G. Kresse and D. Joubert, "From ultrasoft pseudopotentials to the projector augmented-wave method," *Phys. Rev. B*, vol. 59, no. 3, p. 1758, 1999.

[139] S. Grimme, "Semiempirical GGA-type density functional constructed with a long-range dispersion correction," *J. Comput. Chem.*, vol. 27, no. 15, pp. 1787–1799, 2006.

[140] H. Jónsson, G. Mills, and K. W. Jacobsen, "Nudged elastic band method for finding minimum energy paths of transitions," in *Classical and Quantum Dynamics in Condensed*

*Phase Simulations*, World Scientific, 1998, pp. 385–404.

[141] G. Henkelman, B. P. Uberuaga, and H. Jónsson, "A climbing image nudged elastic band method for finding saddle points and minimum energy paths," *J. Chem. Phys.*, vol. 113, no. 22, pp. 9901–9904, 2000.

[142] R. D. King-Smith and D. Vanderbilt, "Theory of polarization of crystalline solids," *Phys. Rev. B*, vol. 47, no. 3, p. 1651, 1993.

[143] V. Maisonneuve, V. B. Cajipe, A. Simon, R. Von Der Muhll, and J. Ravez, "Ferrielectric ordering in lamellar CuInP 2 S 6," *Phys. Rev. B*, vol. 56, no. 17, p. 10860, 1997.

[144] X. Bourdon, V. Maisonneuve, V. B. Cajipe, C. Payen, and J. E. Fischer, "Copper sublattice ordering in layered CuMP 2 Se 6 (M= In, Cr)," *J. Alloys Compd.*, vol. 283, no. 1, pp. 122–127, 1999.

[145] A. Dziaugys, J. Banys, J. Macutkevic, R. Sobiestianskas, and Y. Vysochanskii, "Dipolar glass phase in ferrielectrics: CuInP2S6 and Ag0. 1Cu0. 9InP2S6 crystals," *Phys. status solidi*, vol. 207, no. 8, pp. 1960–1967, 2010.

[146] J. Banys *et al.*, "Dipolar glass behaviour in mixed CuInP2 (S0. 7Se0. 3) 6 crystals," *Ferroelectrics*, vol. 318, no. 1, pp. 163–168, 2005.

[147] M. M. Maior, L. M. Belej, M. I. Gurzan, and Y. M. Vysochanskii, "Peculiarities of the Dipole Ordering in CuInP2 (Se x S1- x) 6 Layered Ferroelectrics," *Ferroelectrics*, vol. 349, no. 1, pp. 71–81, 2007.

[148] L. Bengtsson, "Dipole correction for surface supercell calculations," *Phys. Rev. B*, vol. 59, no. 19, p. 12301, 1999.

[149] S. Baroni and R. Resta, "Ab initio calculation of the macroscopic dielectric constant in silicon," *Phys. Rev. B*, vol. 33, no. 10, p. 7017, 1986.

[150] M. Gajdoš, K. Hummer, G. Kresse, J. Furthmüller, and F. Bechstedt, "Linear optical properties in the projector-augmented wave methodology," *Phys. Rev. B*, vol. 73, no. 4, p. 45112, 2006.

[151] S. P. Beckman, X. Wang, K. M. Rabe, and D. Vanderbilt, "Ideal barriers to polarization reversal and domain-wall motion in strained ferroelectric thin films," *Phys. Rev. B*, vol. 79, no. 14, p. 144124, 2009.

[152] S. Kim, V. Gopalan, and A. Gruverman, "Coercive fields in ferroelectrics: A case study in lithium niobate and lithium tantalate," *Appl. Phys. Lett.*, vol. 80, no. 15, pp. 2740–2742, 2002.

[153] K. Kitamura, Y. Furukawa, K. Niwa, V. Gopalan, and T. E. Mitchell, "Crystal growth and low coercive field 180° domain switching characteristics of stoichiometric LiTaO 3," *Appl. Phys. Lett.*, vol. 73, no. 21, pp. 3073–3075, 1998.

[154] J. Banys, V. Samulionis, V. B. Cajipe, and Y. Vysochanskii, "Dielectric properties of

ferroelectrics CuInP2Se6 and CuCrP2S6," *Ferroelectrics*, vol. 257, no. 1, pp. 163–168, 2001.

[155] K. Moriya, N. Kariya, I. Pritz, Y. M. Vysochanskii, A. Inaba, and T. Matsuo, "The Heat Capacity of CuInP2Se6, a Layer-Structured Selenodiphosphate," *Ferroelectrics*, vol. 346, no. 1, pp. 143–148, 2007.

[156] P. Yang and D. A. Payne, "Thermal stability of field-forced and field-assisted antiferroelectric-ferroelectric phase transformations in Pb (Zr, Sn, Ti) O3," *J. Appl. Phys.*, vol. 71, no. 3, pp. 1361–1367, 1992.

[157] J. Zhai and H. Chen, "Direct current field and temperature dependent behaviors of antiferroelectric to ferroelectric switching in highly (100)-oriented PbZrO 3 thin films," *Appl. Phys. Lett.*, vol. 82, no. 16, pp. 2673–2675, 2003.

[158] Y. Wang *et al.*, "Density functional theory analysis of structural and electronic properties of orthorhombic perovskite CH3NH3PbI3," *Phys. Chem. Chem. Phys.*, vol. 16, no. 4, pp. 1424–1429, 2013.

[159] P. Umari, E. Mosconi, and F. De Angelis, "Relativistic GW calculations on CH 3 NH 3 PbI 3 and CH 3 NH 3 SnI 3 perovskites for solar cell applications," *Sci. Rep.*, vol. 4, p. 4467, 2014.

[160] F. Brivio, K. T. Butler, A. Walsh, and M. Van Schilfgaarde, "Relativistic quasiparticle self-consistent electronic structure of hybrid halide perovskite photovoltaic absorbers," *Phys. Rev. B*, vol. 89, no. 15, p. 155204, 2014.

[161] Z. Fan *et al.*, "Ferroelectricity of CH3NH3PbI3 perovskite," *J. Phys. Chem. Lett.*, vol. 6, no. 7, pp. 1155–1161, 2015.

[162] A. Gulans *et al.*, "Exciting: a full-potential all-electron package implementing density-functional theory and many-body perturbation theory," *J. Phys. Condens. Matter*, vol. 26, no. 36, p. 363202, 2014.

[163] A. Marini, C. Hogan, M. Grüning, and D. Varsano, "Yambo: an ab initio tool for excited state calculations," *Comput. Phys. Commun.*, vol. 180, no. 8, pp. 1392–1403, 2009.

[164] C. Attaccalite and M. Grüning, "Nonlinear optics from an ab initio approach by means of the dynamical Berry phase: Application to second-and third-harmonic generation in semiconductors," *Phys. Rev. B*, vol. 88, no. 23, p. 235113, 2013.

[165] C. C. Stoumpos, C. D. Malliakas, and M. G. Kanatzidis, "Semiconducting tin and lead iodide perovskites with organic cations: phase transitions, high mobilities, and near-infrared photoluminescent properties," *Inorg. Chem.*, vol. 52, no. 15, pp. 9019–9038, 2013.

[166] T. Oku, "Crystal structures of CH3NH3PbI3 and related perovskite compounds used for solar cells," in *Solar Cells-New Approaches and Reviews*, InTech, 2015.

[167] C. Motta, F. El-Mellouhi, S. Kais, N. Tabet, F. Alharbi, and S. Sanvito, "Revealing the

role of organic cations in hybrid halide perovskite CH 3 NH 3 PbI 3," *Nat. Commun.*, vol. 6, p. 7026, 2015.

[168] A. Poglitsch and D. Weber, "Dynamic disorder in methylammoniumtrihalogenoplumbates (II) observed by millimeter-wave spectroscopy," *J. Chem. Phys.*, vol. 87, no. 11, pp. 6373–6378, 1987.

[169] S. Grimme, J. Antony, S. Ehrlich, and H. Krieg, "A consistent and accurate ab initio parametrization of density functional dispersion correction (DFT-D) for the 94 elements H-Pu," *J. Chem. Phys.*, vol. 132, no. 15, p. 154104, 2010.

[170] S. Grimme, S. Ehrlich, and L. Goerigk, "Effect of the damping function in dispersion corrected density functional theory," *J. Comput. Chem.*, vol. 32, no. 7, pp. 1456–1465, 2011.

[171] J. Heyd, G. E. Scuseria, and M. Ernzerhof, "Hybrid functionals based on a screened Coulomb potential," *J. Chem. Phys.*, vol. 118, no. 18, pp. 8207–8215, 2003.

[172] H. J. S. GE and M. Ernzerhof, "Erratum:'Hybrid functionals based on a screened Coulomb potential'[J. Chem. Phys. 118, 8207 (2003)]," *J. Chem. Phys*, vol. 124, p. 219906, 2006.

[173] A. Munir, A. Gordon-Ross, and S. Ranka, *Modeling and optimization of parallel and distributed embedded systems*. John Wiley & Sons, 2015.

[174] M.-Z. Huang and W. Y. Ching, "Calculation of optical excitations in cubic semiconductors. II. Second-harmonic generation," *Phys. Rev. B*, vol. 47, no. 15, p. 9464, 1993.

[175] C. Duan, J. Li, Z. Gu, and D. Wang, "First-principles calculation of the second-harmonic-generation coefficients of borate crystals," *Phys. Rev. B*, vol. 60, no. 13, p. 9435, 1999.

[176] G.-Y. Y. Guo *et al.*, "Hybrid solar cells: perovskites under the sun," *Phys. Rev. B*, vol. 6, no. 8, p. 235441, 2014.

[177] D. O. Demchenko *et al.*, "Optical properties of the organic-inorganic hybrid perovskite C H 3 N H 3 Pb I 3: Theory and experiment," *Phys. Rev. B*, vol. 94, no. 7, p. 75206, 2016.

[178] Y. Yamada, T. Nakamura, M. Endo, A. Wakamiya, and Y. Kanemitsu, "Near-band-edge optical responses of solution-processed organic--inorganic hybrid perovskite CH3NH3PbI3 on mesoporous TiO2 electrodes," *Appl. Phys. Express*, vol. 7, no. 3, p. 32302, 2014.

[179] C.-A. Berseth, C. Wuethrich, and F. K. Reinhart, "The electro-optic coefficients of GaAs: Measurements at 1.32 and 1.52 $μ$m and study of their dispersion between 0.9 and 10 $μ$m," *J. Appl. Phys.*, vol. 71, no. 6, pp. 2821–2825, 1992.

[180] D. B. Chenault, R. A. Chipman, and S.-Y. Lu, "Electro-optic coefficient spectrum of cadmium telluride," *Appl. Opt.*, vol. 33, no. 31, pp. 7382–7389, 1994.